DEVELOPMENT OF A TEST SYSTEM FOR VISCOELASTIC MATERIAL CHARACTERIZATION

A THESIS SUBMITTED TO
THE GRADUATE SCHOOL OF NATURAL AND APPLIED SCIENCES
OF
MIDDLE EAST TECHNICAL UNIVERSITY

BY

FULYA EROL

IN PARTIAL FULFILLMENT OF THE REQUIREMENTS
FOR
THE DEGREE OF MASTER IN SCIENCE
IN
MECHANICAL ENGINEERING

FEBRUARY 2014

Approval of the thesis:

DEVELOPMENT OF A TEST SYSTEM FOR VISCOELASTIC MATERIAL CHARACTERIZATION

submitted by **FULYA EROL** in partial fulfillment of the requirements for the degree of **Master in Science in Mechanical Engineering Department, Middle East Technical University** by,

Prof. Dr. Canan Özgen
Dean, Graduate School of **Natural and Applied Sciences**

Prof. Dr. Süha Oral
Head of Department, **Mechanical Engineering**

Assist. Prof. Dr. Gökhan O. Özgen
Supervisor, **Mechanical Engineering Department, METU**

Examining Committee Members:

Prof. Dr. Suat Kadıoğlu
Mechanical Engineering Department, METU

Assist. Prof. Dr. Gökhan O. Özgen
Mechanical Engineering Department, METU

Assoc. Prof. Dr. Ender Ciğeroğlu
Mechanical Engineering Department, METU

Assist. Prof. Dr. Yiğit Yazıcıoğlu
Mechanical Engineering Department, METU

Assoc. Prof. Dr. Demirkan Çöker
Aerospace Engineering Department, METU

Date: ________________

I hereby declare that all information in this document has been obtained and presented in accordance with academic rules and ethical conduct. I also declare that, as required by these rules and conduct, I have fully cited and referenced all material and results that are not original to this work.

Name, Last Name : FULYA EROL

Signature :

ABSTRACT

DEVELOPMENT OF A TEST SYSTEM FOR VISCOELASTIC MATERIAL CHARACTERIZATION

Erol, Fulya

M.Sc., Department of Mechanical Engineering

Supervisor: Assist. Prof. Dr. Gökhan O. Özgen

February 2014, 159 pages

Viscoelastic materials are used extensively as a means of vibration control and isolation in many vibrating structures. For example, damping instruments utilizing viscoelastic materials such as surface damping treatments and vibration isolators fabricated of viscoelastic materials such as machinery mounts are widely used in automotive and aerospace industries for the purpose of vibration and noise control and isolation, respectively. Viscoelastic materials, as the name implies, behave in between a purely elastic material and a purely viscous material. In other words, they possess both energy storage and energy dissipation characteristics. In order to design an effective damping instrument or vibration isolator utilizing viscoelastic materials, the dynamic properties of viscoelastic materials are to be available in advance. However, these materials have a rather complex dynamic behavior such that their energy storage and dissipation characteristics are dependent on the frequency and temperature at which they are working. There are commercially available test systems dedicated to the determination of dynamic properties of viscoelastic materials; however the companies serving in the aforementioned industries do not tend to purchase them due to their high prices. Therefore, it is economically more feasible for these companies to have their own test system designed. This thesis work is aimed at development of a test system for viscoelastic material characterization to be installed in one of these companies. For this purpose, a test set-up is designed mechanically considering the requirements, specifications and constraints regarding the general vibration tests and specifically the previous work and experience on dynamic testing of viscoelastic materials. Then, a dedicated software program with a user friendly interface is developed for collecting, processing, saving and monitoring the test data and at the end supplying the user with the material properties of the viscoelastic material on which the tests have been conducted.

Keywords: elastomer, rubber, viscoelastic, plastic, dynamic properties, dynamic stiffness, vibration isolators, resilient elements, viscoelastic material characterization, elastomer dynamic testing, dynamic stiffness measurement, elastomer test systems/equipment/machine

ÖZ

VİSKOELASTİK MALZEMELERİN YAPISAL DİNAMİK ÖZELLİKLERİNİN ELDE EDİLMESİNE YÖNELİK BİR TEST SİSTEMİNİN GELİŞTİRİLMESİ

Erol, Fulya

Yüksek Lisans, Makina Mühendisliği Bölümü

Tez Yöneticisi: Yard. Doç. Dr. Gökhan O. Özgen

Şubat 2014, 159 sayfa

Viskoelastik malzemeler titreşime maruz kalan yapılarda titreşim kontrolü ve yalıtımı aracı olarak sıklıkla kullanılmaktadır. Örneğin, yüzey titreşimi sönümleyiciler gibi viskoelastik malzeme kullanan sönümleyici gereçler ve makine takozları gibi viskoelastik malzemeden üretilmiş titreşim yalıtıcıları otomotiv ve havacılık-uzay endüstrilerinde titreşim ve gürültü kontrolü ve yalıtımı amacıyla sıklıkla kullanılmaktadır. Viskoelastik malzemeler adlarının çağrıştırdığı üzere tamamen elastik ve tamamen akışkan malzemelerin davranışlarının arasında bir davranış gösterirler. Başka bir deyişle, hem enerji depolama hem de enerji tüketme özelliklerine sahiptirler. Viskoelastik malzeme kullanarak etkili bir titreşim sönümleyici ya da yalıtıcı tasarlamak için viskoelastik malzemelerin yapısal dinamik özelliklerinin önceden bilinmesi gerekmektedir. Bununla birlikte viskoelastik malzemelerin enerji depolama ve tüketme özellikleri çalıştıkları frekans ve sıcaklığa bağlı olarak değişiklik gösterir ve böylece nispeten karmaşık bir dinamik davranış sergilerler. Viskoelastik malzemelerin karmaşık davranış özelliklerini belirleyen ticari test sistemleri mevcuttur, fakat bunlar oldukça pahalı olduğu için yukarıda bahsedilen firmalar tarafından satın almak için tercih edilmez. Dolayısıyla, bu firmalar için kendi test sistemlerini tasarlatmak ekonomik açıdan daha mantıklıdır. Bu tez çalışması da bu firmalardan birinin kullanımı için viskoelastik malzemelerin yapısal dinamik özelliklerinin elde edilmesine yönelik bir test sisteminin geliştirilmesine yöneliktir. Bu amaçla, genel titreşim testleri ve özellikle viskoelastik malzemelerin dinamik testlerine ait geçmişte yapılmış çalışmalar ve deneyimler ile ilgili gereksinimler, teknik özellikler ve kısıtlamalar göz önüne alınarak bir test düzeneği mekanik olarak tasarlanmıştır. Bunun yanında, test verilerini toplamak, gerekli işlemlerden geçirmek, kaydetmek ve izlemek ve en sonunda kullanıcıya test etmiş olduğu viskoelastik malzemenin malzeme özelliklerini sağlamak amacıyla kullanıcı dostu bir arayüz de içeren bir yazılım programı geliştirilmiştir.

Anahtar Kelimeler: elastomer, kauçuk, viskoelastik, plastik, dinamik özellikler, dinamik direngenlik, titreşim takozu, esnek elemanlar, viskoelastik malzeme karakterizasyonu, elastomer malzeme dinamik testi, dinamik direngenlik ölçümü, elastomer malzeme test sistemleri/ekipmanları/makineleri

To my family

ACKNOWLEDGEMENTS

I would like to express my deepest gratitude to my supervisor Assist. Prof. Dr. Gökhan O. Özgen for his guidance, advice, criticism, encouragements and insight throughout this thesis work.

I would like to acknowledge Roketsan Inc., Taru Engineering Inc. and Ministry of Science, Industry and Technology of Turkish Republic for funding this thesis work.

The technical assistance and contributions of Mr. Sami Samet Özkan and Mr. Bayındır Kuran from Roketsan Inc. are gratefully acknowledged.

I would also like to express my special thanks to Mr. Kenan Gürses for conducting the modal tests of the test set-up designed as a part of this thesis work, Mr. Halil Ardıç for developing the viscoelastic material characterization test procedure and conducting the characterization tests of several viscoelastic specimens, and Mr. Bilgehan Erdoğan for developing the dedicated post-processing software in LabVIEW environment.

TABLE OF CONTENTS

ABSTRACT……………………………………………………………………… v

ÖZ…………………………………………………………………………………vii

ACKNOWLEDGMENTS……………………………………………………… x

TABLE OF CONTENTS………………………………………………………… xi

LIST OF TABLES……………………………………………………………… xv

LIST OF FIGURES……………………………………………………………… xvii

NOMENCLATURE…………………………………………………………… xxviii

CHAPTERS

1. INTRODUCTION…………………………………………………… 1

2. LITERATURE SURVEY………………………………………………5

2.1. General Information on Viscoelastic Material Dynamic Behavior and Characterization……………………………………………… 5

2.2. Searched Standards and Published Studies………………… 11

2.2.1. Searched Standards………………………………… 11

2.2.2. Searched Published Studies…………………………22

2.3. Commercial Test Systems Dedicated to Viscoelastic Material Characterization……………………………………………………31

3. DESIGN AND VALIDATION OF THE TEST SET-UP………………35

3.1. Mathematical Modeling of the Viscoelastic Material Test Set-up…………………………………………………………… 35

3.1.1. Test Specimen Geometries and Dimensioning…… 39

3.1.2. Compensation of Unwanted Input Vibrations………42

3.2. The Test Set-up Designed for Viscoelastic Material Characterization…………………………………………………44

3.3. Improvements on Finite Element Modeling Studies of the Test Set-up for the Best Simulation of Real World Conditions……… 48

3.3.1. Finite Element Modeling Study of the Test Set-up with the Base Plate Included………………………………………54

3.3.2. Finite Element Modeling Study of the Test Set-up Considering the Bolted-Joints between the Parts………… 61

3.3.3. Finite Element Modeling Study of the Test Set-up with 3-D Model of the Ground onto which the Test Set-up is Mounted Added…………………………………………… 67

4. SELECTION OF THE SENSORS, ACTUATOR AND DATA ACQUISITION HARDWARE…………………………………………… 97

4.1. Features of the Selected Vibration Transducers………………102

4.1.1. Features of the Accelerometers……………………… 102

4.1.2. Features of the Force Sensor………………………… 102

4.2. Features of the Selected Vibration Exciter……………………103

4.3. Features of the Selected Data Acquisition Cards………….… 103

4.3.1. Features of the Analog Input Data Acquisition Cards………………………………………………………… 103

4.3.2. Features of the Analog Output Data Acquisition Card…………………………………………………………… 103

5. DEVELOPMENT OF THE TEST SOFTWARE……………………… 105

5.1. Theory and Application of Data Acquisition and Signal Processing……………………………………………………………… 105

5.2. Development of the Dedicated Test Software in LabVIEW Environment Following the Frequency-Response Function Estimation Procedure…………………………………………………………… 108

5.2.1. Generation of Signals to Drive the Electro-dynamic Shaker in LabVIEW……………………………………… 109

5.2.2. Measurement and Processing of the Signals Received from the Vibration Transducers in LabVIEW…………… 110

5.2.3. Additional Programming in LabVIEW…………… 121

6. DEVELOPMENT OF THE TEST PROCEDURE AND PRESENTATION OF SAMPLE TEST RESULTS…………………………………………… 127

6.1. Viscoelastic Material Characterization Test Procedure……… 127

6.2. Sample Viscoelastic Material Characterization Test Results…130

7. CONCLUSION…………………………………………………………135

REFERENCES………………………………………………………………… 139

APPENDICES

A. MATLAB CODES………………………………………………… 143

A.1. MATLAB Code Written to Investigate the Error in the Complex Stiffness of a Viscoelastic Specimen when the Fixture's Frequency-Response-Function is Neglected………………………………… 143

A.2. MATLAB Codes Written to Determine the Vibration Response and Dynamic Strain of Test Specimens for an Excitation Force of 15 N Harmonic Amplitude……………………………………………145

A.2.1. Tensile Specimens………………………………… 145

A.2.2. Shear Specimens……………………………………146

B. IMAGES OF THE DESIGNED USER INTERFACE IN LABVIEW…149

B.1. User Interface of the Tensile Specimen Test Software……… 149

B.2. User Interface of the Shear Specimen Test Software……… 154

LIST OF TABLES

TABLES

Table 1. The categorization of searched standards and published studies according to test methods for viscoelastic material characterization……………………………31

Table 2. Specifications of the elastomer multi-axial and uni-axial testing systems of the company *Saginomiya*……………………………………………………… 32

Table 3. Specifications of the uni-axial servo-hydraulic elastomer testing systems of the company *MTS*……………………………………………………………33

Table 4. Specifications of the dynamic mechanical analyzers with a wide range of force capacities of the company group *ACOEM*………………………………… 33

Table 5. Specifications of the high frequency elastomer testing systems of the company *Inova*……………………………………………………………………34

Table 6. Bill of materials of the test set-up……………………………………… 47

Table 7. The modal frequencies corresponding to the second iteration for convergence…………………………………………………………………… 51

Table 8. The modal frequencies corresponding to the third iteration for convergence…………………………………………………………………… 52

Table 9. The modal frequencies belonging to the first four modes of the initial finite element model of the test set-up………………………………………………… 53

Table 10. Experimental modal frequencies of the designed test set-up obtained as a result of the modal tests………………………………………………………… 77

Table 11. Vibration response and strain determination of tensile specimen configuration for harmonic force amplitude of 15 N in glassy region…………… 99

Table 12. Vibration response and strain determination of tensile specimen configuration for harmonic force amplitude of 15 N in rubbery region………… 99

Table 13. Vibration response and strain determination of double-shear specimen configuration for harmonic force amplitude of 15 N in glassy region……………99

Table 14. Vibration response and strain determination of double-shear specimen configuration for harmonic force amplitude of 15 N in rubbery region………… 100

Table 15. Output voltage signal levels from 1000 mV/g accelerometers for the responses of tensile specimen configuration to harmonic force amplitude of 15 N in both glassy and rubbery regions…………………………………………………… 101

Table 16. Output voltage signal levels from 1000 mV/g accelerometers for the responses of double-shear specimen configuration to harmonic force amplitude of 15 N in both glassy and rubbery regions…………………………………………… 101

Table 17. Properties of FFT calculator in LabVIEW…………………………… 116

LIST OF FIGURES

FIGURES

Figure 1. The applied sinusoidal stress and the resultant strain………………… 6

Figure 2. The frequency dependence of complex modulus property of viscoelastic materials at a constant temperature……………………………………………… 7

Figure 3. The temperature dependence of complex modulus property of viscoelastic materials at a constant frequency………………………………………………… 8

Figure 4. Illustration of frequency-temperature superposition: **(a)** Hypothetical set of complex modulus test data; **(b)** Master curves for storage modulus and loss factor…9

Figure 5. Modified generalized Maxwell model with *N* elements…………….. 10

Figure 6. The test set-up offered for dynamic stiffness determination of vibration isolators exposed to vibrations in the axial direction using the direct method……12

Figure 7. One example of the test set-up's offered for dynamic stiffness determination of vibration isolators exposed to vibrations in lateral directions using the direct method……………………………………………………………… 13

Figure 8. One example of the test set-up's offered for dynamic stiffness determination of vibration isolators exposed to vibrations in the axial direction using the indirect method…………………………………………………………… 15

Figure 9. One example of the test set-up's offered for dynamic stiffness determination of vibration isolators exposed to vibrations in lateral directions using the indirect method…………………………………………………………… 16

Figure 10. The test set-up offered for dynamic stiffness determination of vibration isolators exposed to vibrations in the axial direction using the driving-point method………………………………………………………………………… 17

Figure 11. One example of the test set-up's offered for dynamic stiffness determination of vibration isolators exposed to vibrations in lateral directions using the driving-point method…………………………………………………………… 18

Figure 12. A generic test system for VEM characterization using direct method with necessary measurement units……………………………………………………… 19

Figure 13. A typical test system for determination of the dynamic mechanical properties of rubbery materials using forced non-resonant vibration method…… 22

Figure 14. Schematic representation of the test set-up designed by *Allen*……… 23

Figure 15. Master curves for a specimen tested in the test set-up designed by *Allen*………………………………………………………………………… 24

Figure 16. **(a)** The sandwich plate composed of two steel plates as the constraining layers and a viscoelastic film as the core; **(b)** The test set-up designed by *Kergourlay et.al.* ……………………………………………………………………… 24

Figure 17. Master curves of a viscoelastic film tested without pre-stress in the test set-up designed by *Kergourlay et.al.* …………………………………………… 25

Figure 18. Shear modulus and loss factor curves against prestrain-reduced frequency of a viscoelastic film tested at T = 23°C in the test set-up designed by *Kergourlay et.al.* ……………………………………………………………………… 26

Figure 19. The test set-up designed by *Smith et.al.* …………………………… 26

Figure 20. Frequency dependent tensile modulus and loss factor curves of an elastomeric specimen tested in the test set-up designed by *Smith et.al.* ………… 27

Figure 21. Schematic representation of the test set-up designed by *Cardillo*…… 28

Figure 22. Frequency dependent elastic spring rate and damping coefficient curves of a sample resilient mount tested in the test set-up designed by *Cardillo*……… 29

Figure 23. Schematic representation of the test set-up designed by *Nadeau and Champoux*……………………………………………………………………… 30

Figure 24. Frequency dependent dynamic stiffness magnitude and loss factor curves of a sample resilient mount tested in the test set-up designed by *Nadeau and Champoux* in the axial and lateral directions…………………………………… 30

Figure 25. Configurations for tensile and shear viscoelastic specimen tests performed in accordance with the driving-point method……………………… 34

Figure 26. Two-DOF lumped mass-spring model representing the test set-up utilizing driving-point method………………………………………………… 36

Figure 27. Acceleration measurement of the fixture: **(a)** Tensile specimen configuration; **(b)** Double-shear specimen configuration…………………………37

Figure 28. Actual shear storage modulus of 3M-467 compared to the one obtained using the formulation neglecting the fixture's compliance…………………… 39

Figure 29. Circular, square, and rectangular cross-section tensile specimen geometries…………………………………………………………………40

Figure 30. Recommended geometries for double shear specimen configuration…41

Figure 31. Finite element model of the tensile specimen and the rigid block assembly for illustration of vibrations in bending modes…………………………42

Figure 32. First 6 modes of the tensile specimen and the rigid block assembly: **(a)** 1st bending mode – Version 1 (6.738 Hz); **(b)** 1st bending mode – Version 2 (6.738 Hz); **(c)** Torsional mode (10.128 Hz); **(d)** 2nd bending mode – Version 1 (40.642 Hz); **(e)** 2nd bending mode – Version 2 (40.642 Hz); **(f)** Axial mode (51.369 Hz)…………43

Figure 33. Frequency response amplitude of the axial displacement of the rigid block: **(a)** Mass center of the rigid block and application point of the force are coincident (Peak at 50.861 Hz); **(b)** Mass center of the rigid block and application point of the force are not coincident (1st peak at 6.5 Hz and 2nd peak at 50.861 Hz)……………………………………………………………………44

Figure 34. The final design of the test set-up to which tensile specimen is attached………………………………………………………………45

Figure 35. The final design of the test set-up to which shear specimens are attached (Version 1)……………………………………………………………………46

Figure 36. The final design of the test set-up to which shear specimens are attached (Version 2)……………………………………………………………………46

Figure 37. Initial finite element model of the test set-up corresponding to the first iteration for convergence………………………………………………………… 49

Figure 38. The mode shapes belonging to the initial finite element model of the test set-up corresponding to the first iteration for convergence: **(a)** 1st mode shape at 520.63 Hz; **(b)** 2nd mode shape at 638.02 Hz; **(c)** 3rd mode shape at 813.72 Hz; **(d)** 4th mode shape at 903.65 Hz………………………………………………………… 50

Figure 39. Initial finite element model of the test set-up corresponding to the second iteration for convergence………………………………………………………… 51

Figure 40. Initial finite element model of the test set-up corresponding to the third iteration for convergence………………………………………………………… 52

Figure 41. Representation of a bolted-joint using a threaded hole with three contact regions…………………………………………………………………… 54

Figure 42. The basic finite element modeling methods for a bolted-joint: (a) A simplified solid bolt model; (b) A coupled bolt model; (c) A spider bolt model; (d) No-bolt model………………………………………………………………… 55

Figure 43. The pressure cone for a bolted-joint………………………………… 56

Figure 44. A bolted-joint using a threaded hole………………………………… 57

Figure 45. Representation of the contact regions in the form of hollow circular areas at the bottom surface of the base plate around the holes……………………… 58

Figure 46. The pinball regions for the holes to be bolted to the ground on one of the corners of the base plate: **(a)** Isometric view; **(b)** Top view; **(c)** Front view…… 59

Figure 47. The Finite Element Model of the Test Set-up with the Base Plate… 59

Figure 48. The mode shapes corresponding to the finite element model of the test set-up with the base plate: **(a)** 2nd mode shape at 378.67 Hz; **(b)** 6th mode shape at 444.91 Hz; **(c)** 9th mode shape at 576.37 Hz; **(d)** 10th mode shape at 611.22 Hz… 60

Figure 49. Representation of the contact regions in the form of hollow circular areas at the contacting surfaces of parts of the test set-up around the mating holes…… 63

Figure 50. The pinball regions for the holes to be bolted to each other on the vertical and lateral supports – Front view…………………………………………………… 64

Figure 51. Finite element model of the test set-up with the base plate considering the bolted-joints between the parts…………………………………………………… 65

Figure 52. The mode shapes corresponding to the finite element model of the test set-up with the base plate considering the bolted-joints between the parts: **(a)** 1st mode shape at 286.06 Hz; **(b)** 2nd mode shape at 361.82 Hz; **(c)** 7th mode shape at 433.22 Hz; **(d)** 8th mode shape at 507.39 Hz; **(e)** 9th mode shape at 511.12 Hz… 66

Figure 53. The holes on the base plate which are inserted bolts to mount the base plate to the ground…………………………………………………………… 68

Figure 54. The pinball regions for the holes to be bolted to each other on one of the corners of the base plate and the concrete block representing the compliant ground – Front view……………………………………………………………………68

Figure 55. Finite Element Model of the Test Set-up with the Concrete Block Representing the Compliant Ground (Thickness of the concrete block is 100 mm.)…………………………………………………………………………… 69

Figure 56. The mode shapes corresponding to the finite element model of the test set-up with 3-D model of the ground – first iteration: **(a)** 1st mode shape at 135.74 Hz; **(b)** 2nd mode shape at 165.31 Hz; **(c)** 3rd mode shape at 206.63 Hz; **(d)** 4th mode shape at 248.44 Hz; **(e)** 5th mode shape at 264.9 Hz; **(f)** 6th mode shape at 278.17 Hz; **(g)** 7th mode shape at 338.26 Hz; **(h)** 11th mode shape at 365.91 Hz; **(i)** 12th mode shape at 390.66 Hz……………………………………………………… 70

Figure 57. **(a)** Locations of the tri-axial accelerometers to be placed on the upper part of the test set-up; **(b)** Experimental geometric model of the upper part of the test set-up indicating x-, y-, and z-axis of each accelerometer……………………… 72

Figure 58. The points at which the upper part of the test set-up is excited by an impact hammer……………………………………………………………………… 73

Figure 59. Settings made on LMS Test.Lab user interface for data acquisition and signal processing for modal tests………………………………………………… 74

Figure 60. Auto-power spectral estimate of the excitation induced on the upper part of the test set-up by an impact hammer for each modal test…………………… 75

Figure 61. The driving-point FRF of each excitation point obtained at the end of each modal test with the peaks of the FRF's marked to indicate the possible modal frequencies of the designed test set-up…………………………………………… 76

Figure 62. Experimental mode shapes of the designed test set-up obtained as a result of the modal tests: **(a)** 1st mode shape at 162.8 Hz; **(b)** 2nd mode shape at 317.6 Hz; **(c)** 3rd mode shape at 393.2 Hz; **(d)** 4th mode shape at 439.9 Hz; **(e)** 5th mode shape at 474.2 Hz; **(f)** 6th mode shape at 479.6 Hz; **(g)** 7th mode shape at 530.3 Hz……… 77

Figure 63. The mode shapes corresponding to the finite element model of the test set-up with 3-D model of the ground – second iteration: **(a)** 1st mode shape at 157.21 Hz; **(b)** 2nd mode shape at 183.93 Hz; **(c)** 3rd mode shape at 195.5 Hz; **(d)** 4th mode shape at 256.54 Hz; **(e)** 5th mode shape at 265.67 Hz; **(f)** 6th mode shape at 278.36 Hz; **(g)** 7th mode shape at 299.69 Hz; **(h)** 8th mode shape at 335.41 Hz………… 80

Figure 64. The mode shapes corresponding to the finite element model of the test set-up with 3-D model of the ground – third iteration: **(a)** 1st mode shape at 200.71 Hz; **(b)** 2nd mode shape at 230.04 Hz; **(c)** 3rd mode shape at 270.94 Hz; **(d)** 4th mode shape at 276.55 Hz; **(e)** 5th mode shape at 317.58 Hz; **(f)** 10th mode shape at 420.42 Hz; **(g)** 11th mode shape at 460.4 Hz…………………………………………… 82

Figure 65. Finite Element Model of the Test Set-up with the Concrete Block Representing the Compliant Ground (Thickness of the concrete block is 80 mm.)………………………………………………………………………………… 84

Figure 66. The mode shapes corresponding to the finite element model of the test set-up with 3-D model of the ground – fourth iteration: **(a)** 1st mode shape at 192.08 Hz; **(b)** 2nd mode shape at 223.91 Hz; **(c)** 3rd mode shape at 239.88 Hz; **(d)** 4th mode shape at 264.39 Hz; **(e)** 5th mode shape at 274.72 Hz; **(f)** 10th mode shape at 408.73 Hz; **(g)** 11th mode shape at 458.44 Hz; **(h)** 12th mode shape at 458.87 Hz……… 84

Figure 67. Finite Element Model of the Test Set-up with the Concrete Block Representing the Compliant Ground (Thickness of the concrete block is 60 mm.)………………………………………………………………………………… 86

Figure 68. The mode shapes corresponding to the finite element model of the test set-up with 3-D model of the ground – fifth iteration: **(a)** 1st mode shape at 175.05 Hz; **(b)** 2nd mode shape at 203.03 Hz; **(c)** 3rd mode shape at 211.28 Hz; **(d)** 4th mode shape at 229.69 Hz; **(e)** 5th mode shape at 250.92 Hz; **(f)** 10th mode shape at 390.73 Hz; **(g)** 11th mode shape at 452.87 Hz; **(h)** 12th mode shape at 456.5 Hz…………87

Figure 69. The mode shapes corresponding to the finite element model of the test set-up with 3-D model of the ground – sixth iteration: **(a)** 1st mode shape at 152.11 Hz; **(b)** 2nd mode shape at 171.09 Hz; **(c)** 3rd mode shape at 187.94 Hz; **(d)** 4th mode shape at 193.05 Hz; **(e)** 5th mode shape at 226.44 Hz; **(f)** 10th mode shape at 363.2 Hz; **(g)** 11th mode shape at 430.08 Hz; **(h)** 12th mode shape at 444.86 Hz……… 88

Figure 70. The mode shapes corresponding to the finite element model of the test set-up with 3-D model of the ground – seventh iteration: **(a)** 1st mode shape at 157.34 Hz; **(b)** 2nd mode shape at 190.38 Hz; **(c)** 3rd mode shape at 196.34 Hz; **(d)** 4th mode shape at 212.84 Hz; **(e)** 5th mode shape at 228.83 Hz; **(f)** 10th mode shape at 371.62 Hz; **(g)** 11th mode shape at 432.52 Hz; **(h)** 12th mode shape at 446.5 Hz…………90

Figure 71. The mode shapes corresponding to the finite element model of the test set-up with 3-D model of the ground – eighth iteration: **(a)** 1st mode shape at 162.62 Hz; **(b)** 2nd mode shape at 196.43 Hz; **(c)** 3rd mode shape at 203.02 Hz; **(d)** 4th mode

shape at 220.73 Hz; **(e)** 5th mode shape at 235.18 Hz; **(f)** 10th mode shape at 378.01 Hz; **(g)** 11th mode shape at 438.87 Hz; **(h)** 12th mode shape at 449.54 Hz; **(i)** 13th mode shape at 527.91 Hz………………………………………………………… 92

Figure 72. Representation of aliasing **(a)** Spectrum of a continuous band-limited signal with a maximum frequency, f_c; **(b)** Spectrum of the sampled signal within a finite length of time with a sampling frequency, $f_s > 2f_c$; **(c)** Spectrum of the sampled signal with a sampling frequency, $f_s < 2f_c$…………………………… 107

Figure 73. The part of the developed software belonging to the generation of signals to drive the electro-dynamic shaker……………………………………………… 110

Figure 74. The flowchart for measurement of signals received from the vibration transducers in LabVIEW………………………………………………………… 111

Figure 75. The part of the developed software belonging to the measurement of signals coming from the vibration transducers for tensile specimen tests……… 112

Figure 76. The part of the developed software belonging to the measurement of signals coming from the vibration transducers for shear specimen tests………… 113

Figure 77. Hanning data window……………………………………………… 115

Figure 78. Part of the software developed for VEM characterization that calculates frequencies corresponding to the spectral components of sampled data in time… 117

Figure 79. The part of the developed software belonging to the measurement of signals coming from the thermocouples……………………………………… 122

Figure 80. “TDMS” file format in LabVIEW offering three levels of hierarchy, namely “Root”, “Group”, and “Channel”, with each level allowing an unlimited number of custom properties to be defined……………………………………… 124

Figure 81. Saving test settings in a TDMS file whose path is selectable in the Front Panel……………………………………………………………………… 125

Figure 82. 3-D model of the thermal chamber integrated to the designed test set-up (without the door)……………………………………………………………… 128

Figure 83. Test system composed of the test set-up, the thermal chamber, the shaker with its amplifier and the data acquisition system with the test computer……… 130

Figure 84. The prepared tensile test specimen and the placed vibration transducers and thermocouples……………………………………………………………… 131

Figure 85. Master curves for the tensile specimen of the material EPDM of 50 Shore A hardness at discrete frequencies and temperatures…………………………… 132

Figure 86. Continuous master curves for the tensile specimen of the material EPDM of 50 Shore A hardness together with the master curves at discrete frequencies and temperatures…………………………………………………………………… 133

Figure 87. The tab of the user interface for tensile specimen testing where the measured and generated signal properties are specified………………………… 149

Figure 88. The tab of the user interface for tensile specimen testing where the vibration transducer settings are made…………………………………………… 150

Figure 89. The tab of the user interface for tensile specimen testing where the temperature related settings are made…………………………………………… 150

Figure 90. The tab of the user interface for tensile specimen testing where the test set-up properties are specified…………………………………………………… 151

Figure 91. The tab of the user interface for tensile specimen testing where the file locations to save the resultant data are specified………………………………… 151

Figure 92. The sub-tab of the user interface for tensile specimen testing where the start/stop buttons are located and the sets of measured data are displayed for each record……………………………………………………………………… 152

Figure 93. The sub-tab of the user interface for tensile specimen testing where the power spectral densities of the measured vibration transducer signals and the test temperature are displayed………………………………………………………152

Figure 94. The sub-tab of the user interface for tensile specimen testing where the resultant frequency dependent storage modulus and loss factor data are displayed………………………………………………………………………… 153

Figure 95. The sub-tab of the user interface for tensile specimen testing where the sets of resultant acceleration FRF data are displayed…………………………… 153

Figure 96. The sub-tab of the user interface for tensile specimen testing where the sets of resultant coherence data are displayed…………………………………… 154

Figure 97. The tab of the user interface for shear specimen testing where the measured and generated signal properties are specified………………………… 154

Figure 98. The tab of the user interface for shear specimen testing where the vibration transducer settings are made…………………………………………… 155

Figure 99. The tab of the user interface for shear specimen testing where the temperature related settings are made…………………………………………… 155

Figure 100. The tab of the user interface for shear specimen testing where the test set-up properties are specified…………………………………………………… 156

Figure 101. The tab of the user interface for shear specimen testing where the file locations to save the resultant data are specified………………………………… 156

Figure 102. The sub-tab of the user interface for shear specimen testing where the start/stop buttons are located and the sets of measured data are displayed for each record……………………………………………………………………… 157

Figure 103. The sub-tab of the user interface for shear specimen testing where the power spectral densities of the measured vibration transducer signals and the test temperature are displayed………………………………………………………157

Figure 104. The sub-tab of the user interface for shear specimen testing where the resultant frequency dependent storage modulus and loss factor data are displayed………………………………………………………………………… 158

Figure 105. The sub-tab of the user interface for shear specimen testing where the sets of resultant acceleration FRF data are displayed................................ 158

Figure 106. The sub-tab of the user interface for shear specimen testing where the sets of resultant coherence data are displayed... 159

NOMENCLATURE

t: time (in sec)

f: frequency (in Hz)

ω: frequency (in rad/sec)

T: temperature (*for the relevant uses*)

$\tau(t)$: shear stress as a function of time

$\varphi(t)$: shear strain as a function of time

$G^*(f,T)$: frequency and temperature dependent complex shear modulus

$E^*(\omega,T)$: frequency and temperature dependent complex tensile modulus

$\alpha(T)$: temperature dependent shift factor

$H_{rel}(\omega)$: relative acceleration FRF of the rigid block

k_{VEM}^*: complex stiffness of the viscoelastic specimen

$H_{fix}(\omega)$: FRF of the single-DOF model of the fixture

l': effective grip length for bolted-joints using threaded holes

d: nominal diameter of the bolt

t: thickness of the washer

t_1: thickness of the part without the threaded hole

t_2: thickness of the part with the threaded hole

f_s: sampling frequency (in Hz)

N: number of samples

Δf: frequency spacing between adjacent spectral components (in Hz)

T: record length (in sec) (*for the relevant uses*)

Δt: time spacing between adjacent samples (in sec)

$x(n\Delta t)$: sampled data in time domain

$X(m\Delta f)$: Fourier transform result of the sampled data in frequency domain

S_k: auto- or cross-power spectral estimate

$H_{tensile}$: FRF for a tensile specimen test

H_{shear}: FRF for a shear specimen test

$COH_{tensile}$: coherence function for a tensile specimen test

COH_{shear}: coherence function for a shear specimen test

CHAPTER 1

INTRODUCTION

In engineering applications involving mechanical systems subjected to dynamic loading, mechanical vibrations inevitably occur. The levels of these vibrations are most of the time undesirable since excessive vibrations decrease the life of mechanical systems due to fatigue failure, cause parts to be machined out-of-tolerance due to high levels of machine tool vibrations, distort the operation of high-precision electronic and optical devices and incur an uncomfortable environment for humans due to high levels of structure-borne noise. Therefore, the unwanted levels of vibrations are to be reduced either by utilizing a means of damping which targets the peaks of the frequency response of the mechanical systems, or by isolating the sources of vibrations from the mechanical systems to be protected, depending on the types of application.

Viscoelastic materials (abbreviated as VEM) are widely used for the purpose of vibration control and isolation in industries such as automotive, aerospace and white appliances. The preference of VEM's is based on their ability to serve as both energy storage and dissipation means. In other words, they behave like a combination of metallic spring-viscous damper pairs. However, the dynamic characteristics of VEM's are pretty different than simple metallic springs and viscous dampers in that both energy storage and dissipation characteristics of VEM's are strong functions of frequency and temperature.

In order to design a vibration control or isolation mechanism utilizing VEM's, the frequency and temperature dependent dynamic properties of these materials must be known in advance. There are commercially available test systems dedicated to VEM characterization; however the companies serving in the aforementioned industries do not tend to purchase them due to their high prices. Therefore, it is economically more feasible for these companies to have their own test system designed. The studies carried out for this thesis are aimed at development of a test system for VEM characterization to be installed in one of these companies.

For the purpose of developing a test system for VEM characterization, a well-defined design procedure is followed. First of all, a comprehensive literature survey is conducted in order to obtain a deep insight into the approach of available solutions to the given problem, and to learn their capabilities and limitations. It must be noted here that the scope of the literature survey is limited to the “single-degree-of-freedom (abbreviated as DOF) forced non-resonant” test methods. In the literature survey phase, therefore, commercial products, standards and published studies are investigated thoroughly, and it is seen that there are three main “single-DOF forced non-resonant” test methods for VEM characterization, namely “direct” method, “indirect” method and “driving-point” method. Secondly, the test method to be implemented is selected as “driving-point” method, which is based on dynamically exciting the viscoelastic specimen and measuring the response of the specimen at the same point of the excitation, and conceptual design studies are carried out accordingly. In conceptual design phase, first of all, the design problem is decomposed into its sub-functions. Since the aim is to design a test system, the functional decomposition is made considering the functions that have to be fulfilled in pre-test, during-test and post-test phases. The pre-test phase is composed of the mechanical design of the test set-up by use of which the viscoelastic specimens will be tested, and for this purpose several conceptual design alternatives are created upon brainstorming sessions with Dr. Gökhan Özgen. The during-test phase is composed of generating and measuring the dynamic force input, measuring the viscoelastic specimen response, and controlling and measuring the test temperature. The solutions to these sub-functions are predetermined such that the dynamic force input will be generated by an electrodynamic shaker and measured with a force sensor, the viscoelastic specimen response will be measured with accelerometers, and the test temperature will be controlled with a thermal chamber, and measured with appropriate type of thermocouples. The post-test phase is composed of the development of a dedicated test software that is able to generate the excitation as well as collect, process, save and monitor the measured test data. The programming environment for the test software to be developed is also predetermined to be LabVIEW. Thirdly, detailed design studies are carried out for each sub-function. In detailed design phase, first of all, some preliminary design studies are carried out to guide the mechanical design of the test set-up. Then, according to the conceptual design alternatives created in the conceptual design phase the test set-up is designed utilizing the finite element modeling technique extensively. Considerable effort is expended on improving the finite element model of the test set-up, so that the model best simulates the dynamic behavior of the real test set-up. The main purpose of this extensive finite element modeling study is to serve as a guide to future test set-up design works similar to this thesis work. In addition, in order to select the electrodynamic shaker, the vibration transducers (the force sensor and the accelerometers) and the corresponding data acquisition cards some studies based on the simulation of actual testing conditions are carried out. Furthermore, for the development of the dedicated test software, the digital signal processing and the frequency-response-function (abbreviated as FRF) estimation procedure is studied thoroughly and LabVIEW programming language is mastered to implement this procedure. Finally, the designed test set-up is manufactured and installed with the selected electrical and electronic test equipment, so that characterization tests can readily be conducted with prepared specimens to determine the frequency and temperature dependent properties of the tested viscoelastic materials.

In the thesis, after the introduction, the second chapter is composed of the brief explanation of the characteristics of the VEM dynamic behavior and the summary of the literature survey carried out with emphasis on the significant and inspiring points. The third chapter covers the studies carried out for the design and validation of the VEM characterization test set-up including the mathematical modeling of the test set-up according to the selected “driving-point” test method with details of the specimen geometries and dimensioning and the compensation of unwanted input vibrations, the embodiment design of the test set-up aiming to achieve the best performing configuration, and the further design studies regarding the finite element modeling of the test set-up for the best simulation of the real world conditions. The fourth chapter is devoted to the selection of the electrical and electronic test equipment which involves the vibration transducers, data acquisition cards and the vibration exciter. In the fifth chapter, the theory and application of data acquisition and signal processing for the purpose of the development of the dedicated test software in LabVIEW environment together with the FRF estimation procedure is explained in detail. In the sixth chapter, the VEM characterization test procedure including, successively, preparation of the test specimens, installation of the selected electrical and electronic test equipment and performing of the tests is described, and sample characterization test results are presented. In the final part, a general conclusion derived from the conducted thesis studies is given, and recommendations for improving the performance of the test set-up are stated.

CHAPTER 2

LITERATURE SURVEY

In this part of the thesis, the summary of the literature survey conducted in order to gain sufficient background related to the thesis title “Development of a test system for viscoelastic material characterization” is presented. First of all, general information on viscoelastic material dynamic behavior and characterization is given. This includes the definition of “viscoelasticity”, the unique property of viscoelastic materials called “complex modulus” and its dependence on frequency and temperature, and mathematical modeling techniques for viscoelastic materials to describe complex modulus phenomenon. Then, the searched standards and published studies are introduced with emphasis on significant and inspiring points. Finally, commercial test systems dedicated to viscoelastic material characterization are presented with key features.

2.1. General Information on Viscoelastic Material Dynamic Behavior and Characterization

It is a well-known fact that the stress induced on purely elastic materials is proportional to the corresponding strain whereas the stress induced on purely viscous materials is proportional to the time rate of change of the corresponding strain. Other materials, which do not behave in accordance with any of these two extreme cases, are called as viscoelastic materials, and this phenomenon is called as viscoelasticity. In other words, viscoelastic materials exhibit both energy storage and dissipation characteristics when loaded dynamically [4].

When a harmonically varying stress is applied to a viscoelastic material, the resulting strain will also be harmonic of the same frequency but with a phase angle with respect to the applied stress as shown in Fig.1.

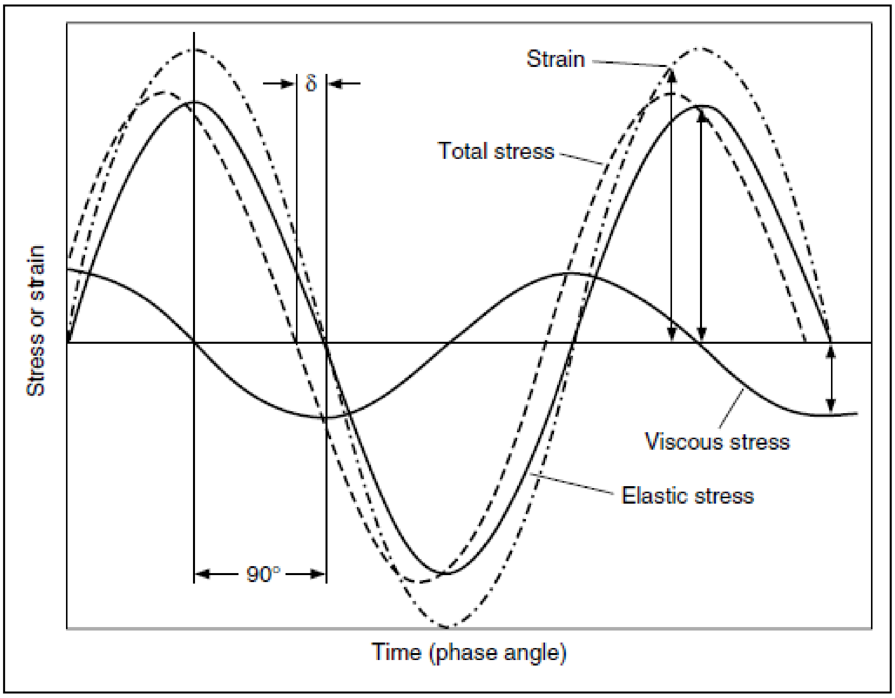

Figure 1. The applied sinusoidal stress and the resultant strain, where δ is the phase angle between them (The elastic stress is completely in-phase with the resultant strain whereas the viscous stress is completely out-of-phase with the resultant strain, as expected.) [1]

The relationship between the stress and the strain can be formulated using the complex exponential function concept. Considering shear deformation;

$$\tau(t) = G^{*}\varphi(t) \text{ ... (Eqn.1)}$$

where $\tau(t) = \tau_o e^{i\omega t}$ is the shear stress of frequency ω and amplitude τ_o, $\varphi(t) = \varphi_o^{*} e^{i\omega t} = \left(\varphi_o e^{-i\delta}\right) e^{i\omega t}$ is the shear strain of frequency ω and complex amplitude τ_o^{*} (amplitude φ_o with a phase angle δ), and $G^{*} = G(1 + i\eta)$ is the complex shear modulus. In the complex modulus designation, $G = \frac{\tau_o}{\varphi_o}\cos\delta$ is called as “storage modulus”, and $\eta = \tan\delta$ is called as “loss factor” [2]. The storage modulus represents the elastic behavior of viscoelastic materials and is a measurement of stiffness whereas the loss factor represents the ratio of the energy dissipated to the energy stored per cycle of harmonic motion and is a measurement of damping [1, 4].

The complex modulus property of viscoelastic materials is a strong function of frequency and temperature. The frequency dependence of complex modulus at a constant temperature is shown in Fig.2.

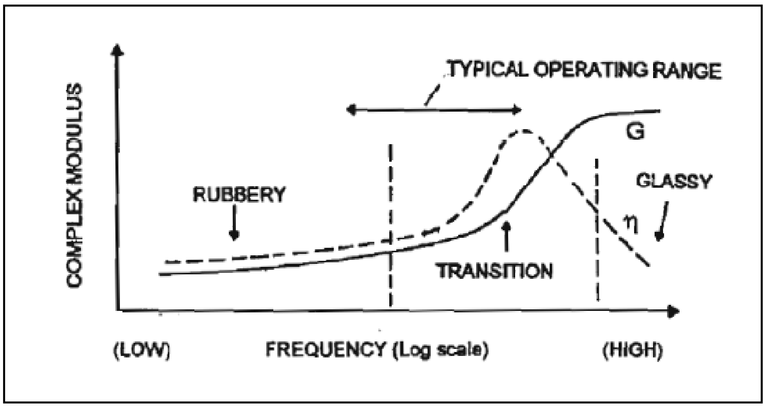

Figure 2. The frequency dependence of complex modulus property of viscoelastic materials at a constant temperature [2]

In the “rubbery region”, which encompasses low frequencies, as shown in Fig.2, viscoelastic materials possess the lowest stiffness and the damping capability is also low. In the “glassy region”, on the other hand, which encompasses high frequencies, as shown in Fig.2, viscoelastic materials possess the highest stiffness but the damping capability is still low. In the “transition region”, which represents the transition from the rubbery region to the glassy region or vice versa, as shown in Fig.2, viscoelastic materials exhibit an abrupt change in stiffness however the damping performance is at its maximum level [2].

The temperature dependence of complex modulus at a constant frequency is shown in Fig.3.

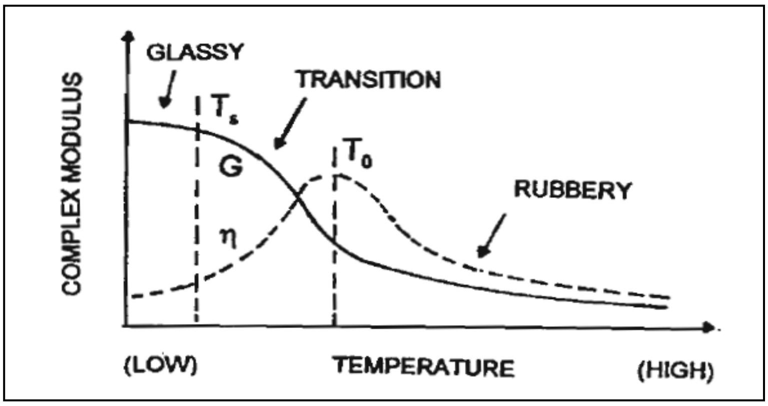

Figure 3. The temperature dependence of complex modulus property of viscoelastic materials at a constant frequency, where T_s is the softening temperature and T_0 is the peak loss factor temperature [2]

It is clearly seen in Fig's 2 and 3 that the temperature dependence of complex modulus is similar to the inverse frequency dependence such that decreasing temperature (at a constant frequency) affects the complex modulus in a similar way as increasing frequency (at a constant temperature). The complex modulus is also dependent on dynamic strain amplitude and preload induced on viscoelastic materials; however the scope of the thesis is confined to linear behavior of viscoelastic materials, which is valid up to a certain dynamic strain amplitude, and the preload effect is not aimed to be investigated [2].

In viscoelastic material characterization tests in order to obtain a set of complex modulus data as a function of both frequency and temperature, it is a common procedure to conduct a test by varying the frequency at a constant temperature, then to repeat the tests at different temperatures. In order to combine the effects of both frequency and temperature into a single variable called as "reduced frequency", a simple but effective operation is to be performed. This operation is called as "frequency-temperature superposition", and formulated as (considering shear deformation again):

$$G^*(f_1, T_1) = G^*\big(f_2\alpha(T_2)\big) \ldots \text{(Eqn.2)}$$

where $\alpha(T)$ is a unique temperature dependent variable called as "shift factor", and the product $f\alpha(T)$ is defined as reduced frequency [2]. The frequency-temperature superposition, illustrated in Fig.4, is based on the assumption that the complex modulus of a viscoelastic material at a certain frequency and temperature is equal to that at another frequency and temperature, and performed such that the obtained complex modulus data at a certain temperature is slide along the frequency axis with respect to the complex modulus data at another selected reference temperature [2]. This operation is continued to be performed until smooth master curves for both storage modulus and loss factor are obtained, as shown in Fig.4, and at the same time the corresponding shift factors are determined.

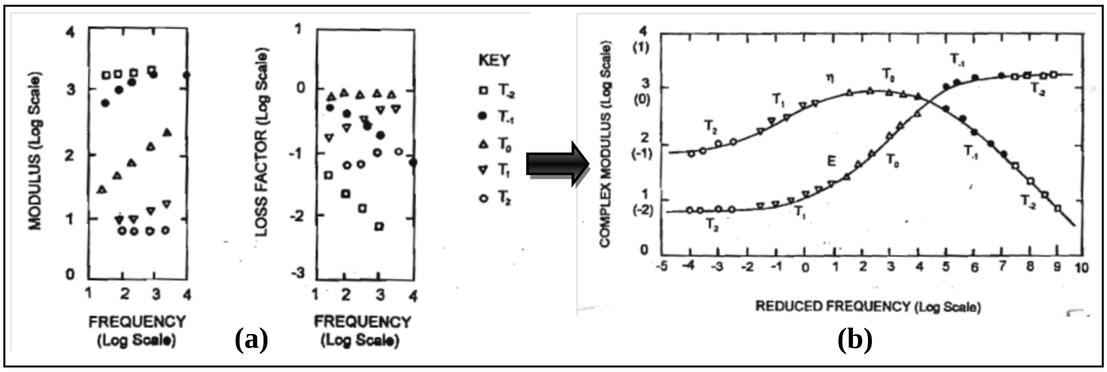

Figure 4. Illustration of frequency-temperature superposition: **(a)** Hypothetical set of complex modulus test data; **(b)** Master curves for storage modulus and loss factor [2]

In order to relate the shift factor not only to discrete test temperatures but also to any temperature, two different equations whose coefficients can be determined as a result of curve fitting are introduced. One of the two equations is referred to as Williams-Landel-Ferry (WLF) shift factor equation, which is nonlinear [2]. The other equation is referred to as Arrhenius shift factor equation, which is linear and therefore simple but sufficiently accurate, and formulated as:

$$\log[\alpha(T)] = T_A\left(\frac{1}{T}-\frac{1}{T_0}\right) \text{... (Eqn.3)}$$

where T_0 is an arbitrary reference temperature, and T_A is the slope of the line $\log[\alpha(T)]$ vs. $1/T$ (all temperatures are in absolute degrees, i.e. C°+273) [2].

It is known that complex modulus data obtained from tests are available only at discrete frequencies and temperatures; however complex modulus values of tested viscoelastic materials at different frequencies and temperatures will surely be needed.

Therefore, in order to relate the complex modulus to any frequency and temperature it is essential to define a continuous mathematical model whose coefficients can be determined as a result of curve fitting. The mathematical models that represent the frequency and temperature dependent complex modulus are: (1) Standard model; (2) Modified generalized Maxwell model; (3) Partial fractional derivative model [25]. The standard model is formulated as (considering normal deformation):

$$E^*(\omega, T) = \frac{E_0\left[1 + \sum_{j=1}^{J} a_j\big(i\omega\alpha(T)\big)^j\right]}{\left[1 + \sum_{k=1}^{K} b_k\big(i\omega\alpha(T)\big)^k\right]} \; \ldots \text{(Eqn.4)}$$

where E_0, a_j and b_k are the parameters to be determined upon curve fitting [25]. The modified generalized Maxwell model is composed of a number of serially connected metallic spring-viscous damper pairs connected in parallel and a single metallic spring element connected to them in parallel, as shown in Fig.5.

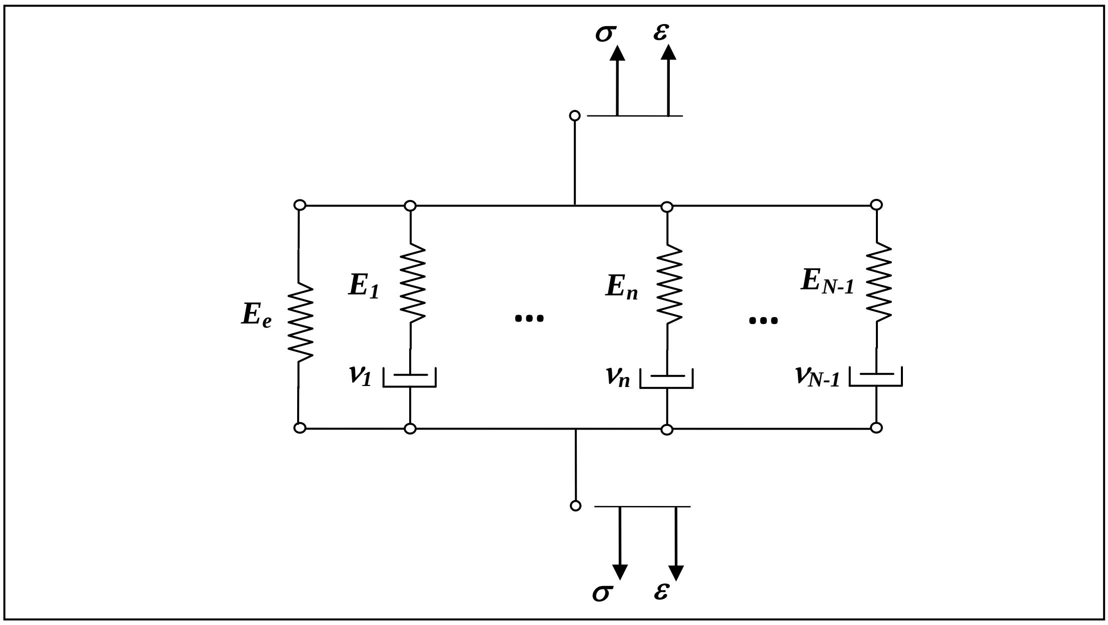

Figure 5. Modified generalized Maxwell model with N elements, where E_e is the Young's modulus of the single metallic spring element, E_n is the Young's modulus of the other metallic spring elements and v_n is the viscosity of the viscous damper elements [25]

The modified generalized Maxwell model is formulated as:

$$E^{*}(\omega, T) = E_e + \sum_{n=1}^{N-1} \frac{i\omega\alpha(T)E_n\tau_n}{1 + i\omega\alpha(T)\tau_n} \text{ ... (Eqn.5)}$$

where E_e, E_n and $\tau_n = \frac{v_n}{E_n}$ are the parameters to be determined upon curve fitting [25]. The partial fractional derivative model, which requires less number of parameters to be determined for a good fit to the complex modulus data compared to the other two models, is formulated as:

$$E^{*}(\omega, T) = \frac{a_1^{*} + b_1^{*}\left(i\omega\alpha(T)\right)^{\beta}}{1 + c_1\left(i\omega\alpha(T)\right)^{\beta}} \text{ ... (Eqn.6)}$$

where a_1^{*}, b_1^{*}, c_1 and β are the parameters to be determined upon curve fitting [25].

2.2. Searched Standards and Published Studies

Since the aim of this thesis is to develop a test system for viscoelastic material characterization, the standards dedicated to dynamic characterization testing of resilient mounts and viscoelastic, plastic and rubber materials, which belong to the same family of materials, are searched, and the characterization methods, the offered test set-up configurations, the given formulations, and the advantages, limitations and recommendations regarding the mentioned methods are all examined thoroughly. The published studies regarding the subject of the thesis are also investigated in terms of the types of characterization methods that are proposed by the standards and used in the studies, the formulations used, the developments brought to the methods, the test system configurations, the capabilities and weaknesses, and the results obtained upon the tests conducted on the specimens.

2.2.1. Searched Standards

The searched standards belong to International Organization for Standardization (abbreviated as ISO) and American Society for Testing and Materials (abbreviated as ASTM). The ISO standards specify the characterization methods either directly for viscoelastic materials or for vibration isolators fabricated of viscoelastic materials and give information on the specific characterization method; however, the ASTM standards give general information on dynamic testing of viscoelastic materials such as plastics and rubbers.

First of all, the ISO standard named ISO 10846 – Part 2: Direct method for determination of the dynamic stiffness of resilient supports for translatory motion [5] is investigated. This standard proposes the "direct method" for characterization (i.e. dynamic stiffness determination) of vibration isolators fabricated of viscoelastic materials in both axial and lateral directions in the frequency range of 1 Hz to an upper limiting frequency, which is set according to certain characteristics of the test set-up. The direct method is based on the "laboratory measurements of vibrations on the input side of a vibration isolator and blocking output forces, which are actually the dynamic forces on the output side of a vibration isolator that result in a zero displacement output" [5]. Then, the ratio of the measured blocking output force to the measured displacement on the input side is taken to determine the dynamic stiffness of the tested vibration isolator. This standard offers the test set-up in Fig.6 for vibrations in the axial direction.

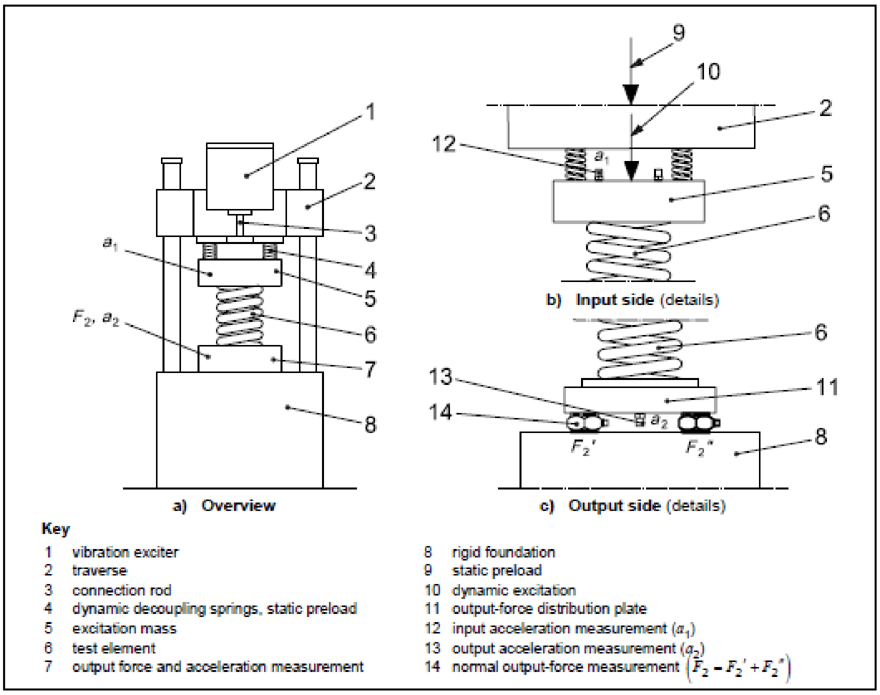

Figure 6. The test set-up offered for dynamic stiffness determination of vibration isolators exposed to vibrations in the axial direction using the direct method [5]

In Fig.6, the aim of using dynamic decoupling springs is to decouple the vibration exciter, so that vibration transmission to the output side of the vibration isolator through the traverse and the guiding columns is reduced. In addition, using an excitation mass as shown in Fig.6 can help to achieve uniform vibrations on the input side of the vibration isolator and also to maintain the vibrations along the axial direction [5]. For vibrations in lateral directions, there are more than one test set-up's offered by this standard. One example is shown in Fig.7.

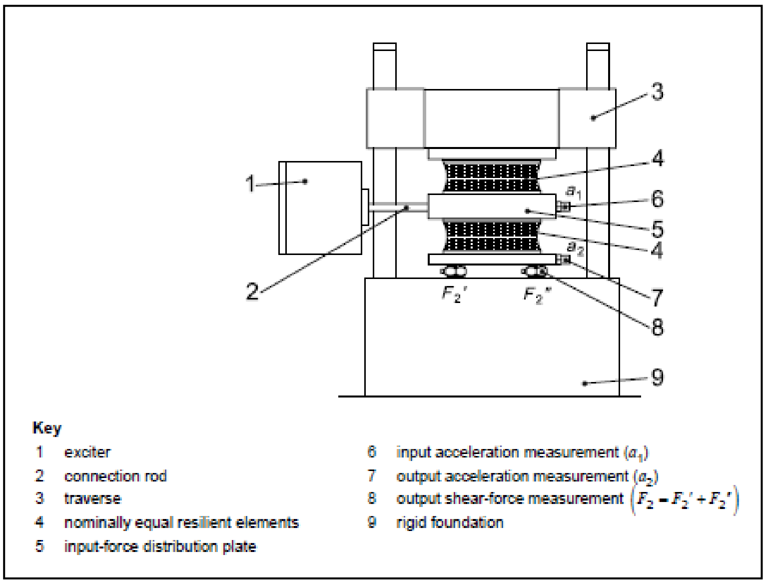

Figure 7. One example of the test set-up's offered for dynamic stiffness determination of vibration isolators exposed to vibrations in lateral directions using the direct method [5]

The purpose of using two identical vibration isolators as shown in Fig.7 is to enhance the simple shear deformation of the vibration isolators, inherently. The limitations of the test method proposed by this standard are as follows [5]: Firstly, the upper limiting frequency is to be set such that the ratio of the measured input acceleration to the measured output acceleration must be greater than 10. The upper limiting frequency is especially important since the output acceleration is possible to attain considerable levels at high frequencies where the dynamic behavior of the test set-up becomes dominant. Secondly, for accurate measurement of the blocking force the output force distribution plate must have a negligible inertial effect such that its mass is to be smaller than 0.06 times the ratio of the blocking force to the output acceleration. Thirdly, for a reliable characterization test the ratio of the input acceleration to the acceleration in a direction other than the main excitation direction (unwanted input vibration) must be greater than 5.62.

Secondly, the ISO standard named ISO 10846 – Part 3: Indirect method for determination of the dynamic stiffness of resilient supports for translatory motion [6] is investigated. This standard proposes the “indirect method” for characterization (i.e. dynamic stiffness determination) of vibration isolators fabricated of viscoelastic materials in both axial and lateral directions in a frequency range of a lower limit in the range of 20 Hz – 50 Hz and an upper limit in the range of 2 kHz – 5 kHz. The indirect method is based on the “laboratory measurements of vibration transmissibility of a vibration isolator” [6]. This standard offers more than one test set-up’s for vibrations in the axial direction. One example is shown in Fig.8.

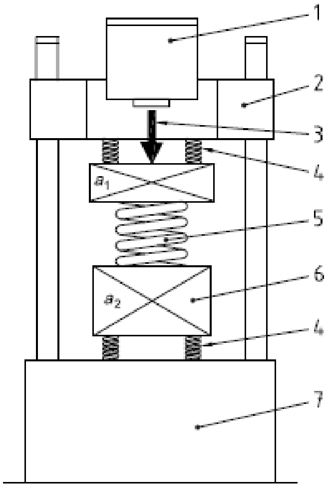

Key

1 Exciter
2 Traverse
3 Connection rod
4 Dynamic decoupling springs, static preload
5 Test element
6 Blocking mass
7 Rigid foundation

a) Overview

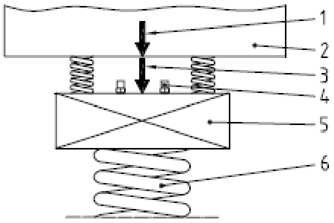

Key

1 Static preload
2 Traverse
3 Dynamic excitation
4 Acceleration measurement (a_1)
5 Excitation mass
6 Test element

b) Input side (details)

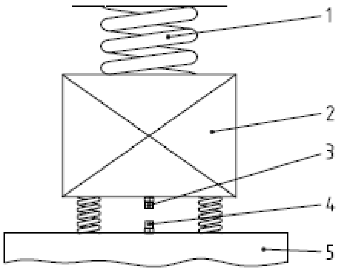

Key

1 Test element
2 Blocking mass (m_1)
3 Acceleration measurement (a_2)
4 Acceleration measurement (a_3)
5 Rigid foundation

c) Output side (details)

Figure 8. One example of the test set-up's offered for dynamic stiffness determination of vibration isolators exposed to vibrations in the axial direction using the indirect method [6]

The rigid blocking body shown in Fig.8 is the crucial part of the test set-up since its mass m_2 determines the dynamic stiffness of the tested vibration isolator together with the measured vibration transmissibility T, which is the ratio of the output displacement to the input displacement, such that the dynamic stiffness is approximately equal to $-(2\pi f)^2 m_2 T$ for $|T| \ll 1$ [6]. The rigid blocking body is suspended on the dynamic decoupling springs as shown in Fig.8. For vibrations in lateral directions, there are also more than one test set-up's offered by this standard. One example is shown in Fig.9.

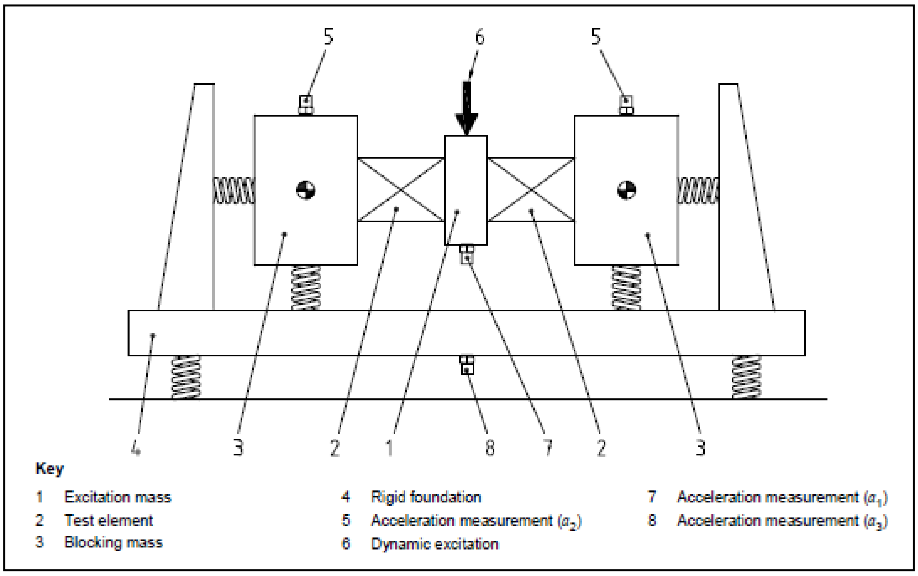

Figure 9. One example of the test set-up's offered for dynamic stiffness determination of vibration isolators exposed to vibrations in lateral directions using the indirect method [6]

The lower frequency limit of the test method proposed by this standard depends on the frequencies corresponding to the rigid-body-modes of the system composed of the vibration isolator, excitation mass, blocking mass and the dynamic decoupling springs. The lower frequency limit must be three times the highest rigid-body-mode frequency of the given system [6]. The upper frequency limit of the test method proposed by this standard, on the other hand, depends on the frequency at which the blocking mass no longer vibrates as a rigid body [6].

Thirdly, the ISO standard named ISO 10846 – Part 5: Driving point method for determination of the low-frequency transfer stiffness of resilient supports for translatory motion [7] is investigated. This standard proposes the “driving-point method” for characterization (i.e. dynamic stiffness determination) of vibration isolators fabricated of viscoelastic materials in both axial and lateral directions in a frequency range of 1 Hz to an upper limiting frequency, which is typically in the range of 50 Hz – 200 Hz. The driving-point method is based on the “laboratory measurement of vibrations and forces on the input side of a vibration isolator with the output side blocked” [7]. Then, the ratio of the measured input force to the measured displacement on the input side is taken to determine the dynamic stiffness of the tested vibration isolator. This standard offers the test set-up in Fig.10 for vibrations in the axial direction.

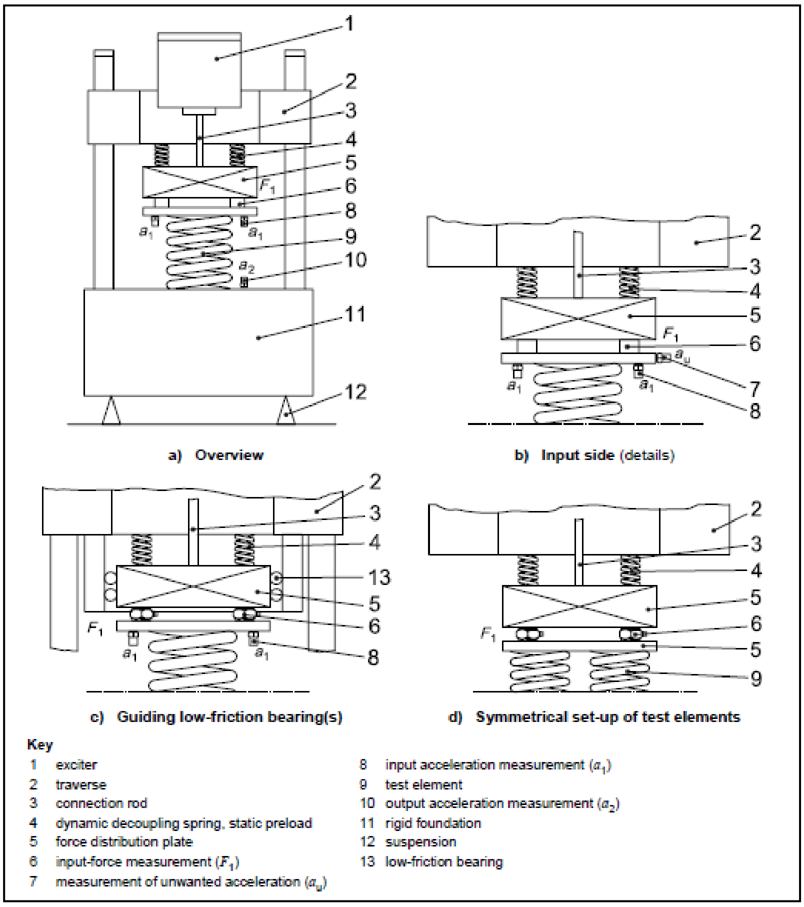

Figure 10. The test set-up offered for dynamic stiffness determination of vibration isolators exposed to vibrations in the axial direction using the driving-point method [7]

For vibrations in lateral directions, there are more than one test set-up's offered by this standard. One example is shown in Fig.11.

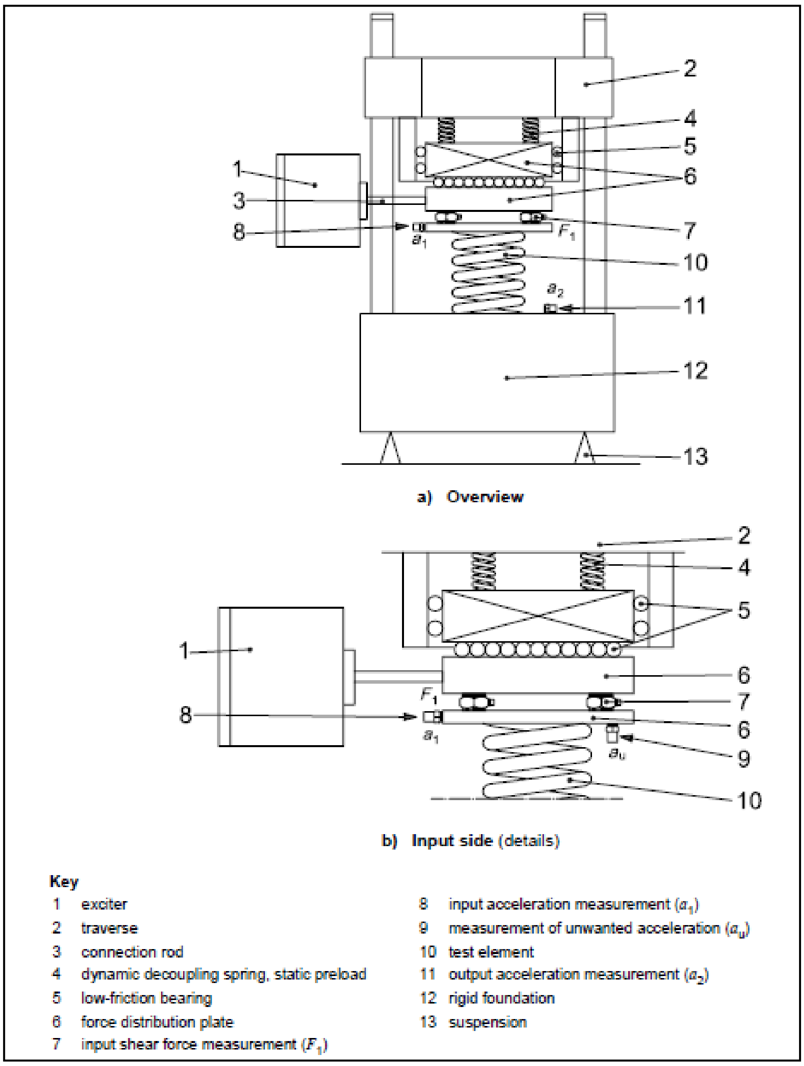

Figure 11. One example of the test set-up's offered for dynamic stiffness determination of vibration isolators exposed to vibrations in lateral directions using the driving-point method [7]

The purpose of using low-friction bearings as shown in Fig's.10 and 11 is to suppress unwanted vibrations that may occur in directions other than the desired direction on the input side of the vibration isolators [7]. The inertial effect of the force distribution plate between the vibration isolator and the input-force transducers shown in Fig.'s 10 and 11 is negligible up to a certain limiting frequency; otherwise, the dynamic stiffness of the vibration isolator is determined inaccurately [7].

Fourthly, the ISO standard named ISO 18437 Characterization of the dynamic mechanical properties of viscoelastic materials – Part 4: Dynamic stiffness method [8] is investigated. This standard proposes the direct (dynamic stiffness) method for determination of complex tensile or shear moduli of linearly behaving viscoelastic materials at small dynamic strain amplitudes including rubbery materials and rigid plastics in a frequency range up to 10 kHz (up to 500 Hz, however, if the viscoelastic material is used for vibration suppression) and in a temperature range of -60°C – +70°C. A generic test system for VEM characterization with necessary electrical and electronic test equipment offered by this standard is shown in Fig.12.

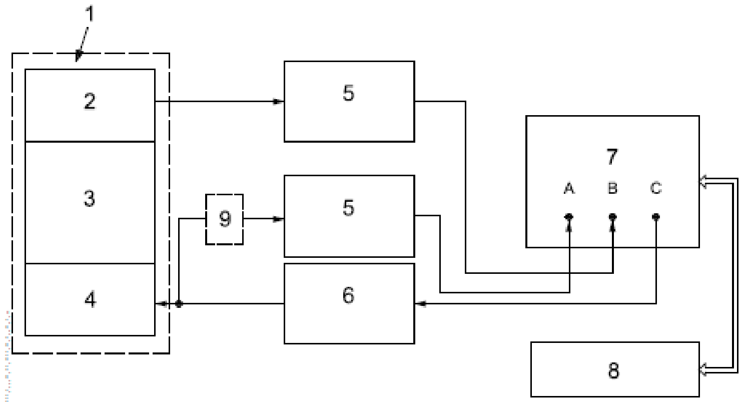

Key

1 test device
2 force transducer
3 test piece
4 displacement actuator
5 amplifier [a]
6 power amplifier
7 dual channel spectrum FFT analyser [b]
8 PC
9 voltage divider
A channel A — displacement from displacement actuator input
B channel B — force from force transducer output
C channel C — excitation signal from the FFT analyser

[a] The amplifier shall have the functions of amplification and attenuation of the signal. If the signal from the output of the power amplifier is too large for the amplifier, a voltage divider shall be added before the amplifier. The voltage divider shall not distort the signal's phase by more than 0,05°.

[b] Channel A is the displacement from displacement actuator input, channel B is the force from force transducer output and channel C is the excitation signal from the FFT analyser.

Figure 12. A generic test system for VEM characterization using direct method with necessary measurement units [8]

The general expression for determination of the complex tensile or shear modulus of a VEM using the measurements indicated in Fig.12 is given as [8]:

$$E^*(f) \text{ or } G^*(f) = \alpha_{E,G}\left[\frac{F(f)}{s(f)}\right] \text{... (Eqn.7)}$$

where $\alpha_{E,G}$ is the ratio of the complex modulus of the tested material to the stiffness of the tested material strained in either tensile or shear mode, and $F(f)/s(f)$ is the complex ratio of the output force to the input displacement. $\alpha_{E,G}$ depends on the geometry of the test material, and the standard recommends test material shapes and gives formulations for the corresponding $\alpha_{E,G}$.

Fifthly, the ISO standard named ISO 6721 Plastics – Determination of dynamic mechanical properties – Part 4: Tensile vibration – Non-resonance method [9] and the ISO standard named ISO 6721 Plastics – Determination of dynamic mechanical properties – Part 6: Shear vibration – Non-resonance method [10] are investigated. The former standard proposes the aforementioned direct method for determination of complex tensile moduli of linearly behaving plastics at small dynamic tensile strain amplitudes in a frequency range of 0.01 Hz – 100 Hz whereas the latter standard proposes the same method for determination of complex shear moduli of linearly behaving plastics at small dynamic shear strain amplitudes in the same frequency range. Both standards offer test set-up configurations, give formulations for determination of complex moduli with corrections for certain cases and give recommendations and limitations about the testing method. In addition, the ASTM standard named ASTM D 4065-06 Standard practice for plastics: Dynamic mechanical properties: Determination and report procedures [11] is investigated. This standard describes general guidelines for experimental studies carried out for determining frequency and temperature dependent dynamic mechanical properties of plastics by free vibration and resonant or non-resonant forced vibration techniques using instruments such as dynamic mechanical analyzers or dynamic thermo-mechanical analyzers. However, since plastics are not intended to be tested with the test set-up designed and used in this thesis work, the details of these standards are not presented.

Finally, the ASTM standard named ASTM D 5992-96 Standard guide for dynamic testing of vulcanized rubber and rubber-like materials using vibratory methods [12] is investigated. This standard covers all free resonant vibration and forced resonant or non-resonant vibration methods for determination of the dynamic mechanical properties of rubbery materials in a frequency range of 0.01 Hz – 100 Hz and in a temperature range of -70°C – +200°C (Not all methods and test systems are able to cover the whole frequency and temperature ranges). It is stated in this standard that measurement of the complex modulus of a rubbery material is affected by three significant factors [12]: (1) Thermodynamic: This is related with the “internal temperature of the specimen”. It is a fact that the internal temperature of a rubbery material increases when the material is mechanically strained due to its internal damping property. Therefore, in order to prevent this fact from causing a considerable increase in the test temperature, which is to be constant throughout the test, some precautions are to be taken. (2) Mechanical: This is related with the “test apparatus”. It is recommended to support the test apparatus on resilient mounts to isolate it from the unpredictable effects of the floor of the test laboratory. It is also recommended to design a test apparatus with a dead mass as large as possible, so that the modal frequencies of the test apparatus on its resilient mounts are smaller than the lower limit of the frequency range of interest. (3) Instrumentation and electronics: This is related with the “ability to obtain and handle signals proportional to the needed physical properties”. The standard points out important factors to consider while selecting the vibration transducers such as stability of their sensitivities with respect to time and temperature change and the data acquisition cards such as their resolution capacities. It is stated that forced non-resonant vibration method is able to cover the widest frequency range among all three methods described in the standard [12]. One of the test systems offered by this standard for forced non-resonant vibration method is shown in Fig.13.

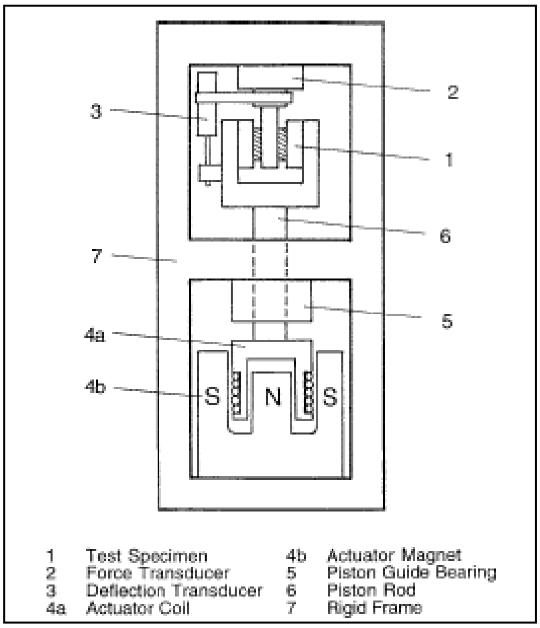

Figure 13. A typical test system for determination of the dynamic mechanical properties of rubbery materials using forced non-resonant vibration method [12]

It is recommended to use double-shear specimens and tensile specimens with one end bonded to an auxiliary part. As final recommendations, the vibration measurements especially at high frequencies where the displacements and forces become small and dynamic behavior of the fixture could become dominant must be handled carefully for accurate stiffness measurements [12]. The measurement of the dimensions of a specimen must also be performed carefully because the accuracy of the measurement of the dimensions directly affects the accuracy of the modulus measurements [12]. Lastly, slipping, which is a form of damping, must be avoided within the test set-up because this will distort the accuracy of the damping measurements of a specimen [12].

2.2.2. Searched Published Studies

In the study by *Allen* [13], a test set-up is designed to measure frequency and temperature dependent complex shear moduli of VEM’s using the aforementioned driving-point method. The schematic representation of the test set-up is shown in Fig.14.

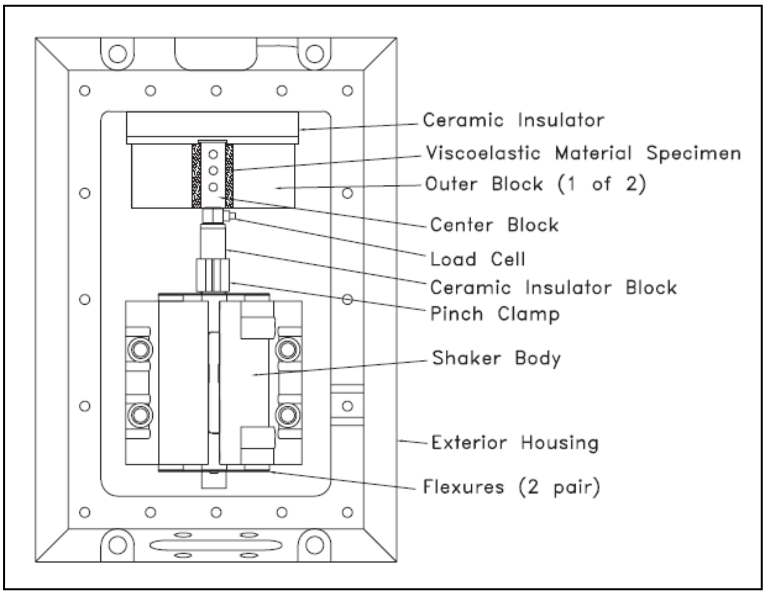

Figure 14. Schematic representation of the test set-up designed by *Allen* [13]

As can be seen in Fig.14, double-shear specimen configuration is used with a center block excited by a shaker through its stinger and two outer blocks fixed to the exterior housing. The force applied on the center block is measured by a load cell conventionally; however, rather than measuring the absolute displacement of the center block the relative displacement between the center block and the outer blocks is measured by a non-contacting displacement sensor to minimize the effect of machine compliance, which is the development brought to the driving-point method by this study [13]. By this way, a frequency range of 0.1 Hz – 500 Hz is achieved [13]. Another distinction in this study is that a liquid convection temperature control is used with a reservoir, heating and cooling elements and a heat exchanger directly contacting both outer blocks, and a temperature range of -80°F – 370°F (-60°C – +185°C) is accommodated [13]. Two thermocouples are used to measure the temperatures of one of the outer blocks and the center block, and when their difference becomes less than 1°F, the temperature is approved to be stable. Thermal insulators shown in Fig.14, which have a modulus of elasticity greater than the aluminum that the center and outer blocks are made of, are used to maintain the temperature uniformity within the outer blocks, the center block and the test specimen [13]. Test results for a specimen are shown in Fig.15.

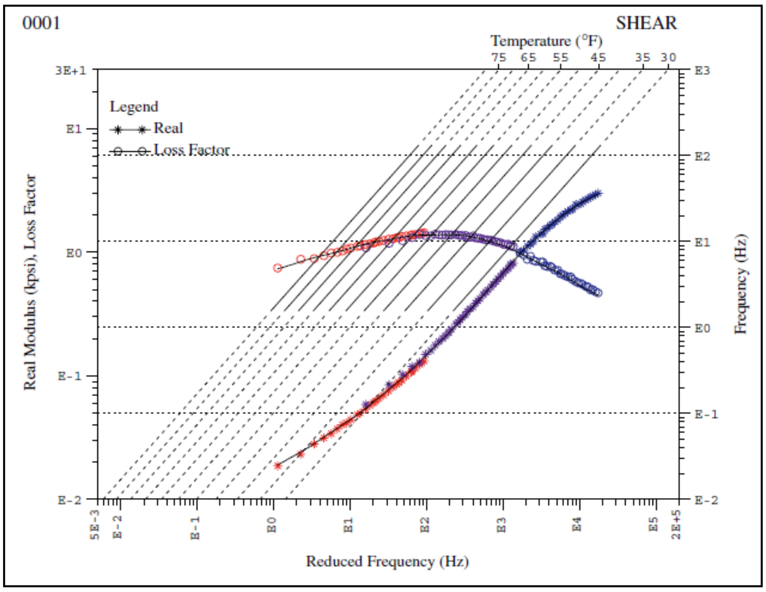

Figure 15. Master curves for a specimen tested in the test set-up designed by *Allen* [13]

In the study by *Kergourlay et.al.* [14], a test set-up is designed to measure the complex shear moduli of viscoelastic films used in sandwich plates under considerable static load using the aforementioned driving-point method. The frequency range is given as 1 Hz – 2000 Hz, the pre-strain range is given as 0 – 3, and the temperature range is given as 0°C – 50°C. The configuration of the sandwich plate and the test set-up is shown in Fig.16.

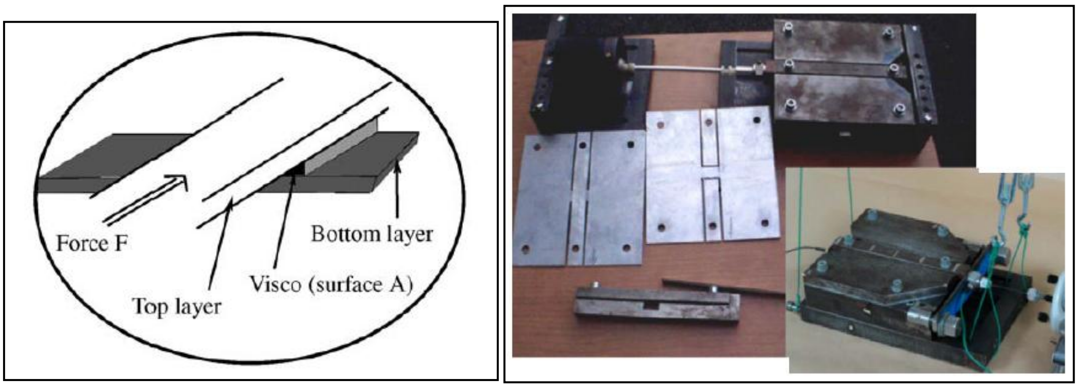

(a) **(b)**

Figure 16. **(a)** The sandwich plate composed of two steel plates as the constraining layers and a viscoelastic film as the core (top layer designed to translate whereas bottom layer designed to be fixed); **(b)** The test set-up designed by *Kergourlay et.al.* [14]

In order to induce pre-strain on the viscoelastic film, a pre-stress beam is employed, as shown in Fig.16b on the right. A Hall affect position sensor is used to measure both the static displacement induced by the pre-stress beam and the dynamic relative displacement of the moving plate, and a force sensor is used to measure the force applied by the shaker to the moving plate through a piano wire [14]. The distinctions in this study are that the test set-up is hung at its corners as shown in Fig.16b on the right, and the test set-up is placed into a thermal chamber to observe the temperature dependency of the complex moduli of the tested viscoelastic films [14]. A test is conducted on a viscoelastic film without pre-stress, and the master curves are obtained as shown in Fig.17 using the frequency-temperature superposition technique.

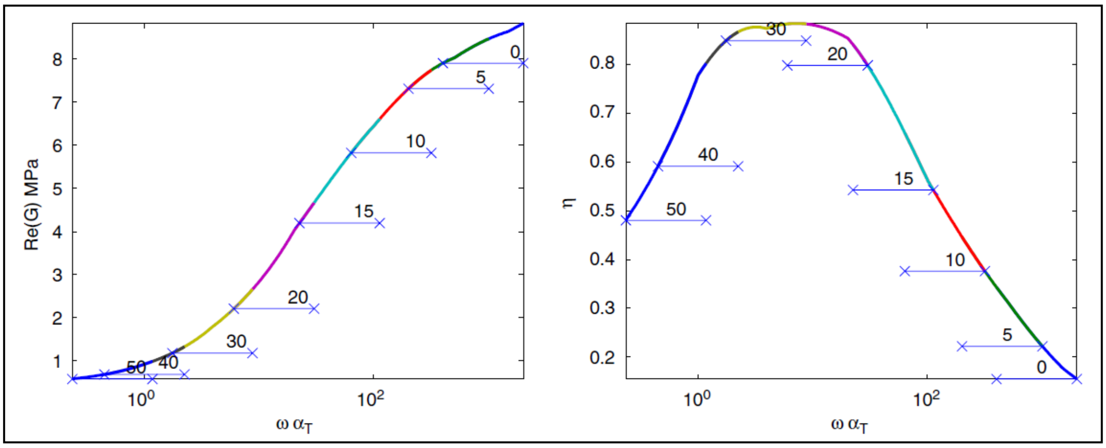

Figure 17. Master curves of a viscoelastic film tested without pre-stress in the test set-up designed by *Kergourlay et.al.* [14]

Applicability of the frequency-prestrain superposition is also investigated, and the curves shown in Fig.18 are obtained. It is seen that although the trends of the resultant curves are as expected, the superposition technique does not result in smooth transition between data sets corresponding to different pre-strain values especially for the loss factor [14].

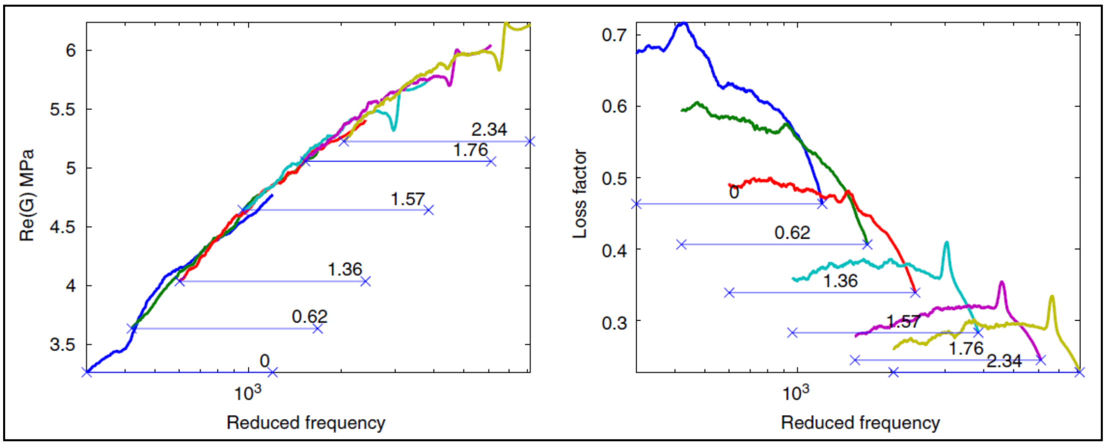

Figure 18. Shear modulus and loss factor curves against prestrain-reduced frequency of a viscoelastic film tested at T = 23°C in the test set-up designed by *Kergourlay et.al.* [14]

In the study by *Smith et.al.* [15], a test set-up is designed to measure the frequency dependent complex shear moduli of elastomers using the aforementioned indirect method. It is stated that reliable results can be obtained at frequencies as high as 6000 Hz. The test set-up is shown in Fig.19.

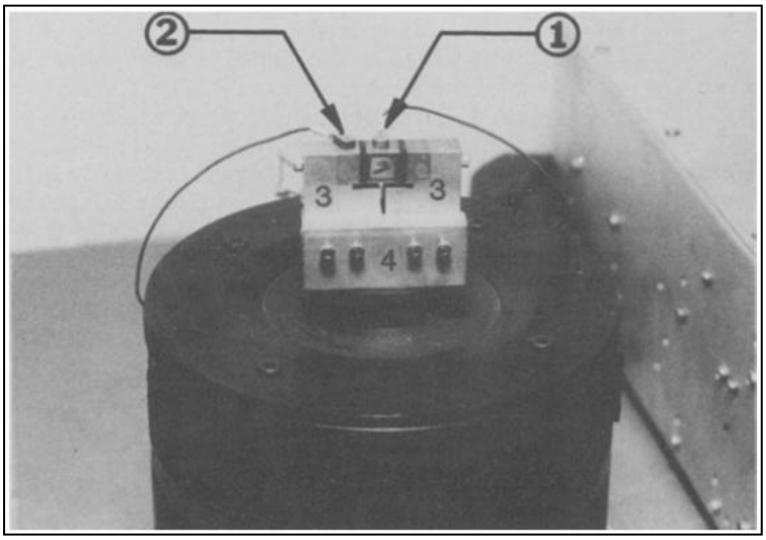

Figure 19. The test set-up designed by *Smith et.al.*[15]

Numbers 1 and 2 in Fig.19 indicate micro-miniature piezoelectric accelerometers attached to the center block and one of the side blocks of the double-shear specimen assembly, respectively. Number 3 indicates two support fixtures to which the double-shear specimen assembly is attached, and number 4 indicates the shaker head fixture to which the rest of the test set-up is mounted. Test results for the frequency dependent tensile modulus and loss factor of an elastomeric specimen are shown in Fig.20.

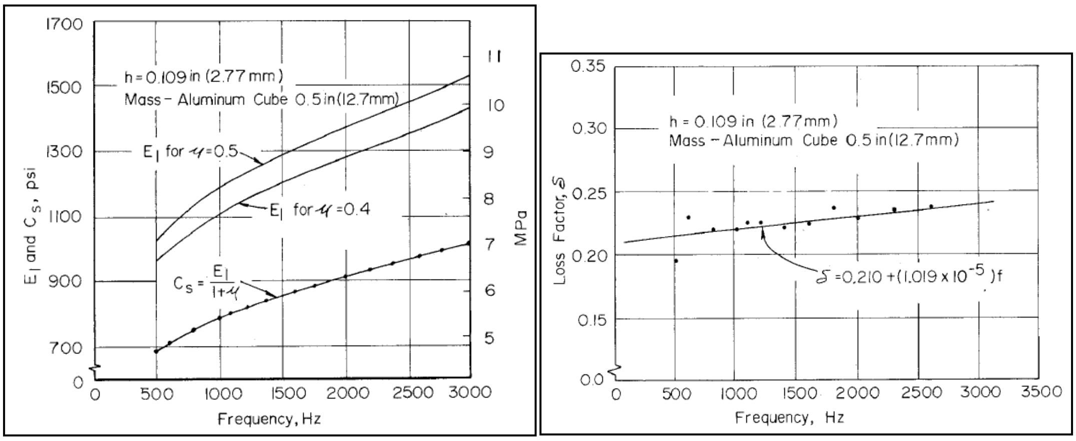

Figure 20. Frequency dependent tensile modulus and loss factor curves of an elastomeric specimen tested in the test set-up designed by *Smith et.al.* (*h* indicates the thickness of the specimen and μ indicates the Poisson's ratio of the specimen.) [15]

In the study by *Thompson et.al.* [16], the aforementioned indirect method for measuring the dynamic stiffness of vibration isolators is concerned in terms of developing the method by shifting the lower frequency limit of the method to the lowest possible values. The direct and indirect methods are compared, and it is stated that the dynamic stiffness of vibration isolators can be measured at much higher frequencies using the indirect method. Also it is stated that the direct method is more suitable for measuring the dynamic stiffness of vibration isolators in the axial direction whereas the dynamic stiffness values in lateral and rotational directions can also be measured using the indirect method [16]. However, as pointed out in [6], the lower frequency limit of the indirect method is to take a certain value higher than the highest rigid-body-mode frequency of the system composed of the vibration isolator, excitation mass, blocking mass and the dynamic decoupling springs. Therefore, this study discusses two ways to decrease the lower frequency limit of the indirect method [16]: (1) measuring the transmissibility between the net displacement of the vibration isolator (input displacement minus output displacement) and the displacement of the blocking body (output displacement); (2) replacing the mass of the blocking body with its frequency dependent effective mass, which is defined as the ratio of the force applied by the vibration isolator onto the blocking body to the acceleration of the blocking body.

In the study by *Cardillo* [17], a test set-up is designed to measure frequency, temperature and preload dependent dynamic stiffness of resilient mounts using the aforementioned direct method. The schematic representation of the test set-up is shown in Fig.21.

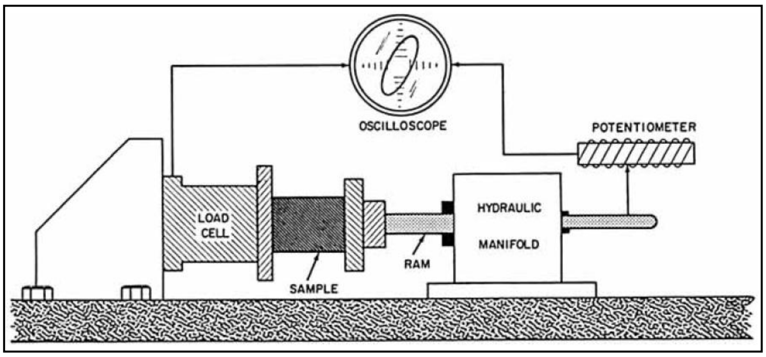

Figure 21. Schematic representation of the test set-up designed by *Cardillo* [17]

The distinctions in this study are that the vibrations are induced on the samples by a servo-controlled hydraulic power unit in the frequency range of 0.01 Hz – 100 Hz, and the temperature dependent tests are conducted using an insulated temperature control box in the range of -50°F – +250°F (-45°C – +120°C). Frequency dependent test results for a sample resilient mount at a constant temperature and preload are shown in Fig.22.

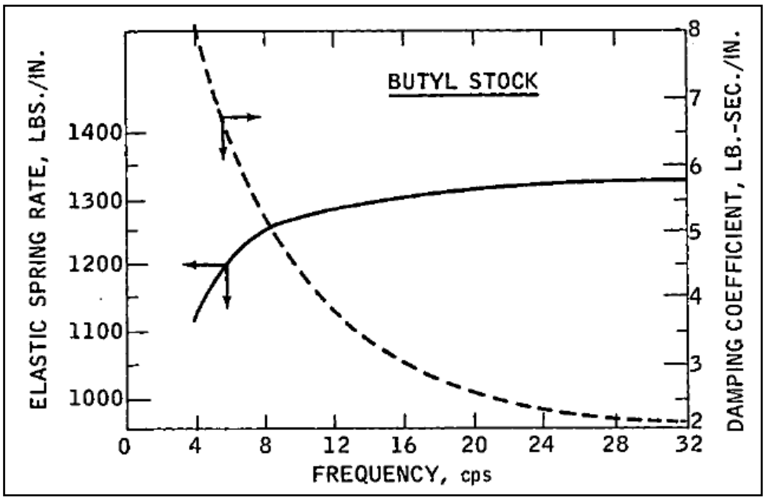

Figure 22. Frequency dependent elastic spring rate (real component of dynamic spring rate) and damping coefficient (the ratio of imaginary component of spring rate to frequency) curves of a sample resilient mount tested in the test set-up designed by *Cardillo* (75°F (23°C) test temperature; 250 lb (115 kg) preload) [17]

It is denoted that the shapes of the curves are somehow distorted due to increase in the temperature of the sample during the test [17].

Finally, in the study by *Nadeau and Champoux* [18], a test set-up with two different configurations are designed to measure the frequency dependent dynamic stiffness of resilient mounts in the axial and lateral directions separately using the aforementioned direct method. The schematic representation of the test set-up is shown in Fig.23.

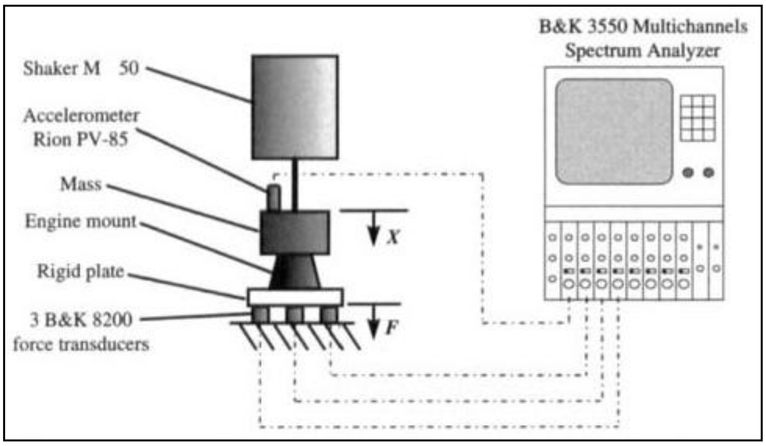

Figure 23. Schematic representation of the test set-up designed by *Nadeau and Champoux* [18]

The purpose of putting a mass on the top of the resilient mount as shown in Fig.23 is to apply a preload on the resilient mount [18]. As a result of a case study, the dynamic stiffness magnitude and loss factor data for both axial and lateral directions are obtained as shown in Fig.24.

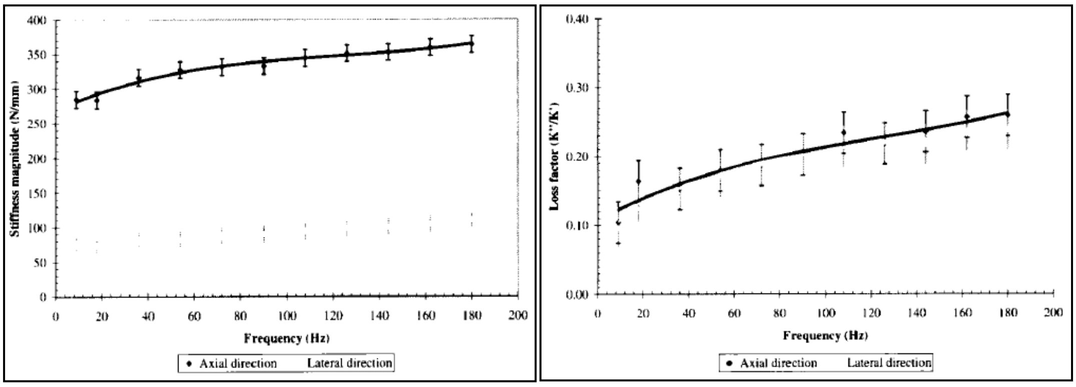

Figure 24. Frequency dependent dynamic stiffness magnitude and loss factor curves of a sample resilient mount tested in the test set-up designed by *Nadeau and Champoux* in the axial and lateral directions [18]

As can be seen in Fig.24, the frequency range of measurements is 10 Hz – 180 Hz. It is stated that since the acceleration levels are quite small at low frequencies, it is reasonable to use an accelerometer with a high sensitivity, and since the force levels required to excite the resilient mounts are quite large at high frequencies, the shaker is to be selected accordingly [18].

To sum up, the searched standards and published studies are categorized according to the test methods for viscoelastic material (or resilient mount) characterization as given in Table 1.

Table 1. The categorization of searched standards and published studies according to the test methods for viscoelastic material (or resilient mount) characterization

Test Method	**Standard**	**Published Study**
Direct Method	ISO 10846 – Part 2, ISO 18437 – Part 4, ISO 6721 – Part 4, ISO 6721 – Part 6 [5, 8, 9, 10]	Cardillo, Nadeau and Champoux [17, 18]
Indirect Method	ISO 10846 – Part 3 [6]	Smith et.al., Thompson et.al. [15, 16]
Driving-Point Method	ISO 10846 – Part 5 [7]	Allen, Kergourlay et.al. [13, 14]
Not-Specified	ASTM D 4065-06, ASTM D 5992-96 [11, 12]	Not-Available

2.3. Commercial Test Systems Dedicated to Viscoelastic Material Characterization

First of all, the specifications of the elastomer multi-axial and uni-axial testing systems of the Japanese company *Saginomiya*, which is specialized in automatic control units and test systems, are tabulated in Table 2.

Table 2. Specifications of the elastomer multi-axial and uni-axial testing systems of the company *Saginomiya* [41]

Specifications	Multi-axial testing system	Uni-axial testing systems	
	KCH703-30	KCH701-30	KCH701-20
x, y, z axis max. force	20 kN	20 kN (z-axis)	20 kN (z-axis)
x, y, z axis max. displacement	±30 mm	±50 mm (z-axis)	±60 mm (z-axis)
Max. velocity	35 cm/s	50 cm/s	50 cm/s
Frequency range	0.1 to 200 Hz	0.1 to 1000 Hz	0.1 to 300 Hz
Preload displacement	±15 mm	Not-Available	Not-Available
Optional	- Independent excitation mode up to 1 kHz in z-axis - Temperature control chamber in the range of -40 to +150°C	Not-Available	Not-Available

Secondly, the specifications of the uni-axial servo-hydraulic elastomer test systems of the company *MTS*, which is specialized in sensors and test systems, are tabulated in Table 3.

Table 3. Specifications of the uni-axial servo-hydraulic elastomer testing systems of the company *MTS* [42]

Specifications	Landmark™ 100 Hz	Landmark™ 200 Hz	Model 831.50 1000 Hz
Max. dynamic force	25 kN	100 kN	10 kN
Max. displacement	±75 mm	±50 mm	±20 mm
Frequency range	Up to 100 Hz	Up to 200 Hz	0.01 to 1000 Hz
Thermal chamber option	No	Yes (Temperature range not specified)	Yes (Temperature range: -100 to +200°C)

Thirdly, the specifications of the dynamic mechanical analyzers with a wide range of force capacities of the company group *ACOEM*, which is specialized in various subjects including material testing, are tabulated in Table 4.

Table 4. Specifications of the dynamic mechanical analyzers with a wide range of force capacities of the company group *ACOEM* [43]

Specifications	Desktop Series		DMA+ 100, 150, 450 Series			DMA+ 1000, 2000 Series	
	DMA 25	DMA 50	DMA+ 100	DMA+ 150	DMA+ 450	DMA+ 1000	DMA+ 2000
Max. force	25 N	50 N	100 N	150 N	450 N	1000 N	2000 N
Max. displacement	±3 mm		Not-Specified			±6 mm	
Frequency range	10^{-5} to 200 Hz		10^{-5} to 1000 Hz			10^{-5} to 1000 Hz	
Temperature range	-150 to +500°C		Not-Specified (Thermal chamber option available)			-150 to +500°C	
Excitation mode	Not-Specified		Tension/compression/bending/shear				

Finally, the specifications of the high frequency elastomer testing systems of the company *Inova*, which is specialized in servo-hydraulic and mechanical testing systems, are tabulated in Table 5.

Table 5. Specifications of the high frequency elastomer testing systems of the company *Inova* [44]

Specifications	FU500-16	FU500-25
Max. force	16 kN	25 kN
Max. displacement	±25 mm	
Frequency range	Up to 200 Hz	Up to 500 Hz
Optional	- Side load unit for side load application and multi-axis characterization (Max. side load: 5 kN for FU500-16; 3kN for FU 500-25) - Thermal chamber	

As a result of certain discussions, it is decided to implement the "driving-point method", which is depicted in Fig.25, in order to design the viscoelastic material characterization test set-up utilized in the thesis work.

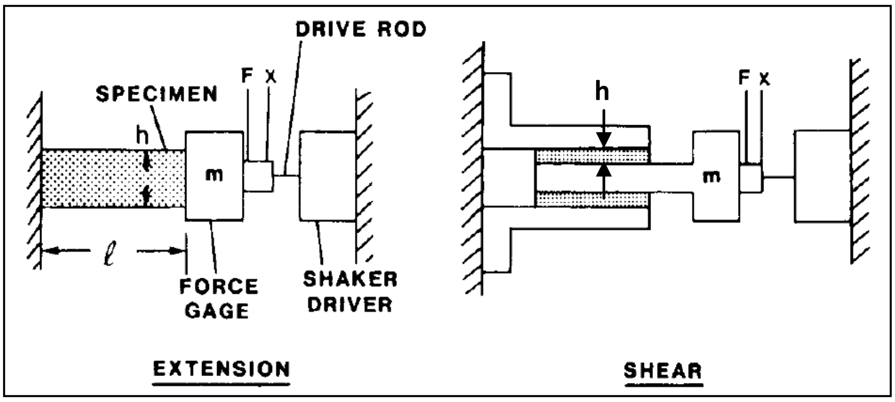

Figure 25. Configurations for tensile and shear viscoelastic specimen tests performed in accordance with the driving-point method [1]

CHAPTER 3

DESIGN AND VALIDATION OF THE TEST SET-UP

In this part of the thesis, the studies carried out to design and validate the test set-up are presented. First of all, a mathematical model that well represents the test set-up to be designed is derived considering several important aspects of the problem. The purpose is to relate the measured mechanical quantities (i.e., force and acceleration) of the test set-up during a material test to the dynamic characteristics (i.e. complex modulus) of the tested material. Secondly, the VEM characterization test set-up is designed through extensive utilization of the finite element modeling technique. The main target in designing the test set-up is to maximize its first structural modal frequency. Finally, further design studies regarding finite element modeling of the test set-up are carried out apart from the ones conducted initially to design the test set-up. These studies aim at improving the finite element model of the test set-up to best simulate the real world conditions.

3.1. Mathematical Modeling of the Viscoelastic Material Test Set-up

It was stated at the end of the literature survey part that the driving-point method is adopted to be utilized so that the designed test set-up is based on the principles of this method. Therefore, the mathematical model that represents the test set-up is derived to be compatible with the driving-point method.

Since it is not possible to establish a perfectly rigid fixture, modeling the dynamic behavior of a viscoelastic specimen as if it is attached to a rigid foundation will not give accurate results. The main idea in mathematical modeling is, therefore, to include the compliance of the fixture [19, 20]. The fixture is represented as a lumped mass-spring system in the direction of the applied force as shown in Fig.26. This model is sufficient for a frequency range of analysis that includes only the first natural frequency of the fixture.

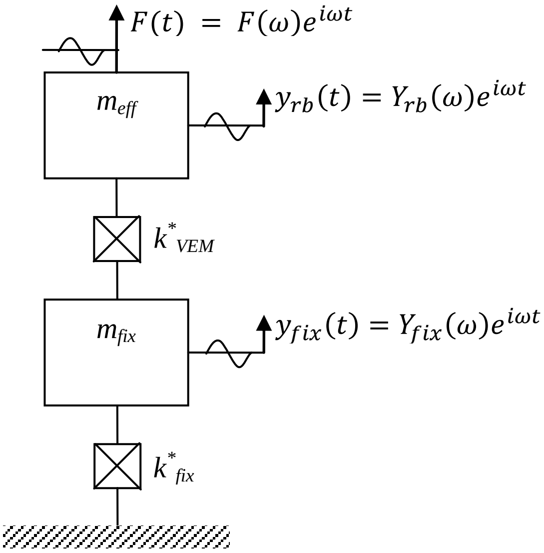

Figure 26. Two-DOF lumped mass-spring model representing the test set-up utilizing driving-point method, where $F(t)$: forcing function; $y_{rb}(t)$: absolute displacement response of the rigid block attached to the specimen; $y_{fix}(t)$: absolute displacement response of the fixture; m_{eff}: effective vibrating mass; m_{fix}: effective fixture mass; k^*_{VEM}: complex stiffness of the viscoelastic specimen; k_{fix}: effective fixture stiffness

As stated in the literature survey part, the driving-point method is based on the measurement of the input force acting on the test specimen and the corresponding response of the test specimen. In Fig.26, $F(\omega)$ is the harmonic amplitude of the input force, and $Y_{rb}(\omega)$ and $Y_{fix}(\omega)$ are the harmonic amplitudes of the absolute displacement responses of the rigid block attached to the specimen and the fixture, respectively. The harmonic amplitude of the net displacement response of the test specimen can, therefore, be obtained by taking the difference of $Y_{rb}(\omega)$ and $Y_{fix}(\omega)$. Dividing this quantity by $F(\omega)$ is defined as the relative displacement FRF of the rigid block and is formulated as:

$$H_{rel}(\omega) = \frac{Y_{rb}(\omega) - Y_{fix}(\omega)}{F(\omega)} \text{ ... (Eqn.8)}$$

$H_{rel}(\omega)$ can be determined by exciting the test set-up by an electrodynamic shaker and measuring the input force using a force transducer and the responses of the rigid block and the fixture using accelerometers during the tests conducted on viscoelastic specimens. It is well known that converting harmonic acceleration amplitude, designated as $A(\omega)$, to harmonic displacement amplitude, designated as $D(\omega)$, is achieved as such:

$$D(\omega) = -\frac{A(\omega)}{\omega^2} \text{ ... (Eqn.9)}$$

It is required to measure accelerations at points on the line of action of the applied force [5, 6, 7]. However, as can be seen in Fig.27 this is not possible for the parts of the fixture to which the viscoelastic specimens are directly attached. Therefore, as stated in [5, 6, 7], signals coming from two accelerometers symmetrically placed on the parts of the fixture directly attached to the test specimens about the line of action of the excitation force are linearly averaged, which is also shown in Fig.27.

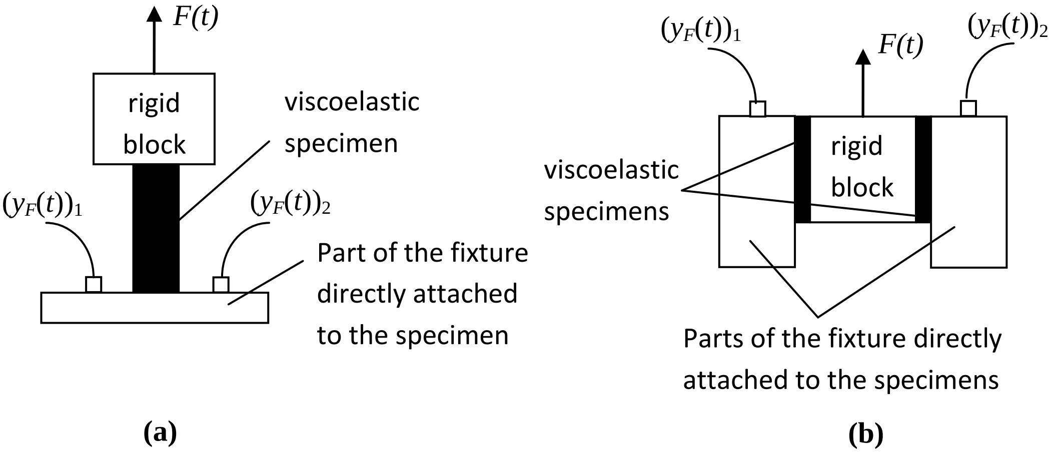

Figure 27. Acceleration measurement of the fixture: **(a)** Tensile specimen configuration; **(b)** Double-shear specimen configuration

Writing the equations of motion of the rigid block and the fixture separately considering the two-DOF system in Fig.26 and carrying out a harmonic response analysis corresponding to a harmonic excitation, the frequency dependent complex stiffness of the viscoelastic specimen can be obtained as [19, 20]:

$$k_{VEM}^{*} = \frac{1 + m_{eff}\omega^2 H_{rel}(\omega)}{\left(-m_{eff}\omega^2 H_{fix}(\omega) + 1\right) H_{rel}(\omega)} \text{ ... (Eqn.10)}$$

where m_{eff} is formulated as $m_{eff} = m_{rb} + m_{transducer} + \frac{m_{specimen}}{3}$ [2, 15, 19].

The $H_{fix}(\omega)$ term in Eqn.10 is the FRF of the single-DOF model of the fixture and is formulated as [19, 20]:

$$H_{fix}(\omega) = \frac{1}{-\omega^2 m_{fix} + k_{fix}^{*}} = \frac{1/m_{fix}}{-\omega^2 + (\omega_n)_{fix}^2} \text{ ... (Eqn.11)}$$

where $(\omega_n)_{fix}$ is the first natural frequency of the fixture.

To obtain the complex stiffness of the tested specimen as a function of frequency, $H_{fix}(\omega)$ must be determined in advance. However, determining $H_{fix}(\omega)$ accurately either by a finite element analysis or by modal testing is a difficult task to achieve. Therefore, it is preferable to neglect this term in Eqn.10, which reduces to:

$$k_{VEM}^{*} = \frac{1 + m_{eff}\omega^2 H_{rel}(\omega)}{H_{rel}(\omega)} \text{ ... (Eqn.12)}$$

To see how much error will be involved in k^{*}_{VEM} when $H_{fix}(\omega)$ is neglected, a code which compares the predetermined complex modulus of a VEM named 3M-467 by 3M Company [2] with the one obtained using Eqn.12 for representative values of the terms involved in the equation is written in MATLAB [see Appendix A.1]. For 0.7 kg of effective vibrating mass, 80 kg of effective fixture mass and 500 Hz of fixture's first natural frequency, which are close to the corresponding values of the initial model of the test set-up, the result is shown in Fig.28 as a function of frequency.

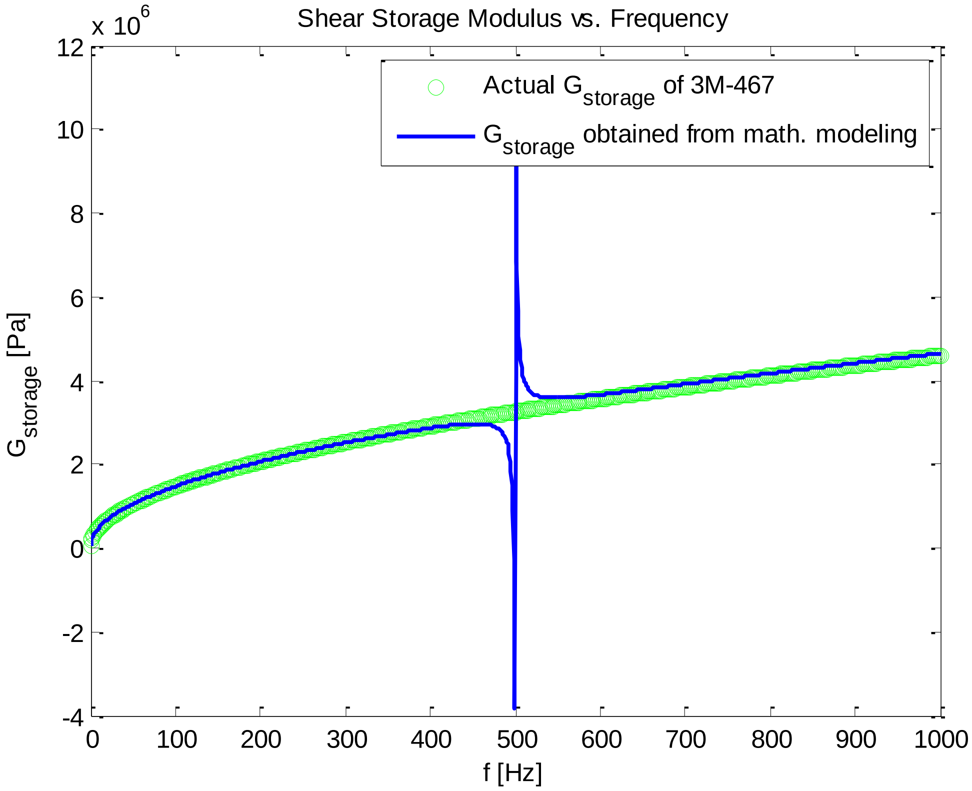

Figure 28. Actual shear storage modulus of 3M-467 compared to the one obtained using the formulation neglecting the fixture's compliance

As seen in Fig.28, considerable amount of error in storage modulus of the given material occurs only within the frequency range close to the first natural frequency of the fixture, which is taken as 500 Hz for the purpose of this simulation. This result can surely be generalized to conclude that the complex stiffness values of the tested VEM's obtained using the formulation that neglects the fixture's FRF are sufficiently accurate at frequencies below the first natural frequency of the fixture.

3.1.1. Test Specimen Geometries and Dimensioning

It is required to determine both the tensile and shear complex moduli of a VEM in order to verify the relationship between them, $E^* = 3G^*$, for a typical Poisson' ratio value of 0.499 [21]. Therefore, the test set-up is designed to accommodate both the tensile and shear specimen configurations.

The recommended tensile specimen geometries are shown in Fig.29.

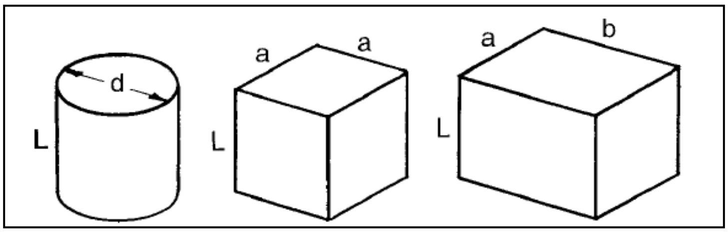

Figure 29. Circular, square, and rectangular cross-section tensile specimen geometries [12]

For tensile specimens of square cross-section, which are selected to be used for the tests conducted using the designed test set-up, the relation between the complex stiffness determined as a function of frequency using Eqn.12 and the complex tensile modulus is identified as [12]:

$$E^*_{VEM} = k^*_{VEM} \frac{L}{a^2} \text{ ... (Eqn.13)}$$

where *L* is the length of the specimen in the direction of the applied force and *a* is the edge length of the square cross-section.

The recommended geometries for double shear specimen configuration are shown in Fig.30.

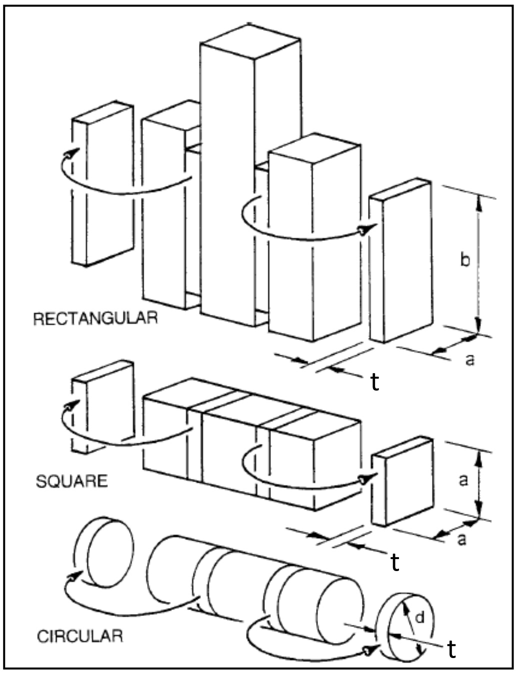

Figure 30. Recommended geometries for double shear specimen configuration [12]

For shear specimens of square cross-section, which are selected to be used for the tests conducted using the designed test set-up, the relation between the complex stiffness determined as a function of frequency using Eqn.12 and the complex shear modulus is identified as [12]:

$$G^*_{VEM} = k^*_{VEM}\,\frac{t}{2a^2} \text{ ... (Eqn.14)}$$

where t is the thickness of the specimen and a is the edge length of the square cross-section.

These equations are derived assuming that uniform stress and strain distribution occurs within the specimen body. However, it is possible for tensile specimens to bulge and for shear specimens to bend rather than deform in simple shear mode. To be able to neglect these undesired deformations, the specimen dimensions are recommended to be selected considering the following conditions [8, 19]:

$$\frac{L}{a} \geq 2.5 \text{ (for tensile specimen) ... (Eqn.15a)}$$

$$\frac{a}{t} \geq 4 \text{ (for shear specimen) ... (Eqn.15b)}$$

According to the aforementioned considerations about the specimen dimensioning, the tensile specimens to be tested in the designed test set-up are selected to have a square cross-section edge length value of 3 cm and length values changing between 6 cm and 9 cm ($2 \leq L/a \leq 3$), and the shear specimens are selected to have a square cross-section edge length value of 5 cm and thickness values changing between 1 mm and 9 mm ($5.6 \leq a/t \leq 50$).

3.1.2. Compensation of Unwanted Input Vibrations

It is essential to excite the tensile specimens purely in axial mode and the shear specimens purely in simple shear mode to accurately determine their complex tensile and shear moduli, respectively. However, there may be unwanted input vibrations induced on the specimens during the characterization tests. As it is stated in the literature survey part, the double-shear specimen configuration enhances simple shear deformation and minimizes the effects of deformations in other undesired modes, inherently. The geometry of tensile specimens, however, does not help to maintain the axial deformation, and an asymmetrical excitation causes additional deformations in undesired modes [5, 6, 7]. For example, if the mass center of the rigid block attached to the input side of the tensile specimen is not coincident with the point to which the vibration exciter is attached, the specimen will undergo vibrations in bending modes in addition to the axial mode. To illustrate this effect, a finite element analysis is performed in ANSYS Workbench using the model shown in Fig.31.

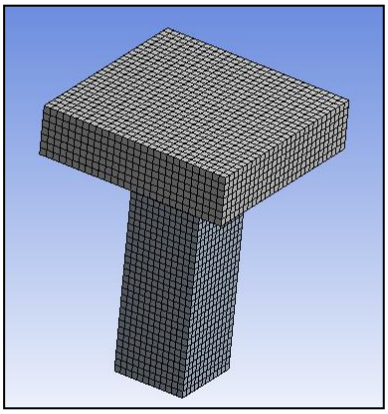

Figure 31. Finite element model of the tensile specimen and the rigid block assembly for illustration of vibrations in bending modes

For the purpose of this simulation, a (80mm)x(20mm)x(80mm) stainless steel rigid block (nearly the same as the one used in the designed test set-up) and a (30mm)x(90mm)x(30mm) viscoelastic specimen of 1100 kg/m^3 density (for soft commercial rubber [29]) and 10 MPa rubbery region Young's modulus (included within the range of the Young's moduli of various commercially available VEM's [19]) are used. The modal analysis of this model with the other end of the specimen fixed yields the natural frequencies and the mode shapes as shown in Fig.32.

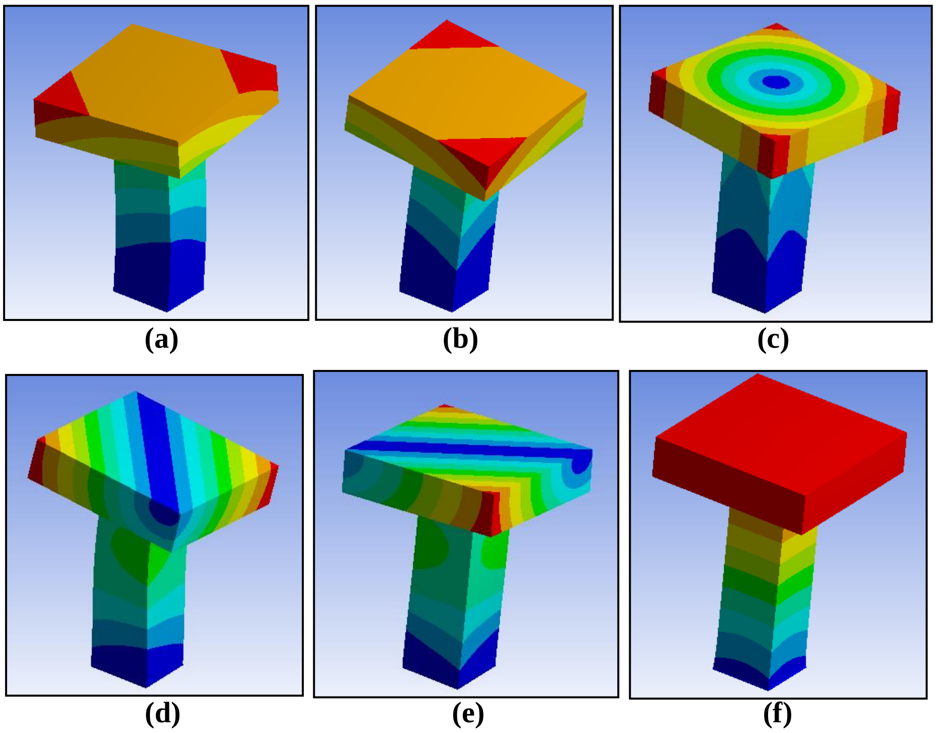
(a) (b) (c)
(d) (e) (f)

Figure 32. First 6 modes of the tensile specimen and the rigid block assembly: **(a)** 1st bending mode – Version 1 (6.738 Hz); **(b)** 1st bending mode – Version 2 (6.738 Hz); **(c)** Torsional mode (10.128 Hz); **(d)** 2nd bending mode – Version 1 (40.642 Hz); **(e)** 2nd bending mode – Version 2 (40.642 Hz); **(f)** Axial mode (51.369 Hz)

A harmonic analysis of the model is also performed to see the effect of the given modes other than the axial mode on the frequency response of the axial displacement of the rigid block for an axial load of unit amplitude. The results for the cases when the force is applied at the mass center of the rigid block and when it is applied at a point 1 mm away from the mass center of the rigid block in both lateral directions are shown in Fig.33.

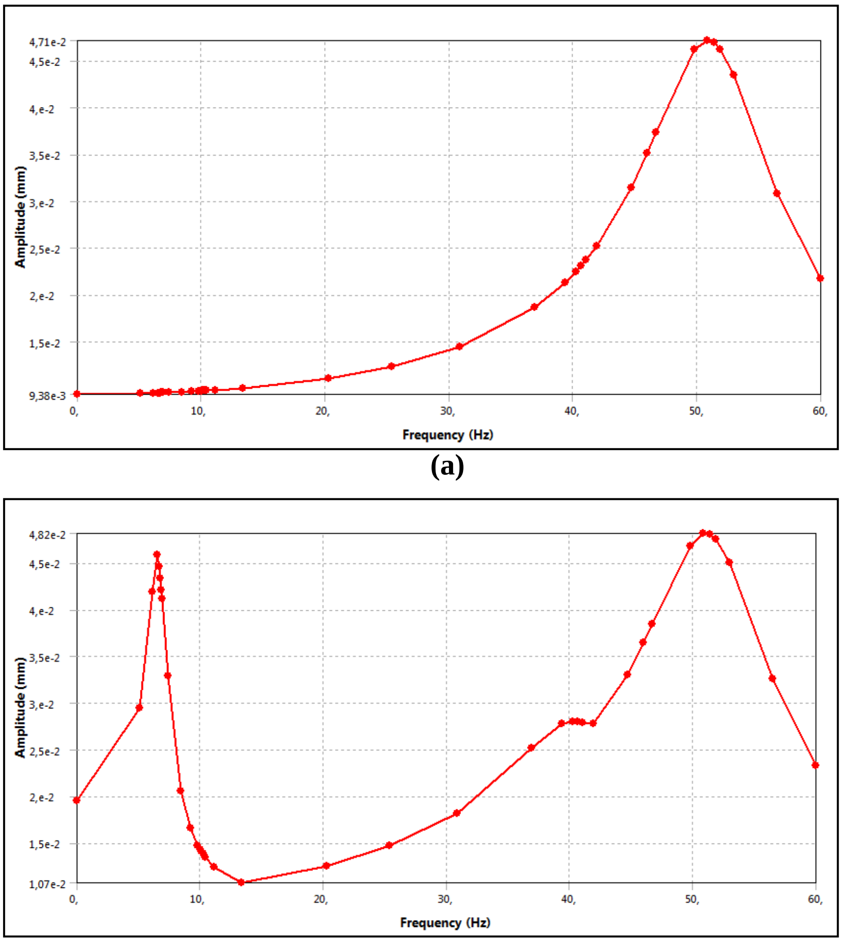

(a)

(b)

Figure 33. Frequency response amplitude of the axial displacement of the rigid block: **(a)** Mass center of the rigid block and application point of the force are coincident (Peak at 50.861 Hz); **(b)** Mass center of the rigid block and application point of the force are not coincident (1st peak at 6.5 Hz and 2nd peak at 50.861 Hz)

As seen in Fig.33, vibration modes other than the axial mode are not excited for the ideal case of coincident mass center of the rigid block and application point of the force. However, for an eccentricity of even small amount1st bending mode is also excited, which causes highly inaccurate data for the frequency response of the axial displacement of the rigid block around its corresponding natural frequency.

To compensate for the undesired bending deformations, signals coming from two accelerometers symmetrically placed on the rigid block about its mass center are linearly averaged.

3.2. The Test Set-up Designed for Viscoelastic Material Characterization

The effort expended to design the test set-up utilized in the thesis work is aimed at maximizing the first natural frequency of the fixture while keeping the weight of the parts that compose the test set-up at minimum considering modularity and portability and at the same time minimizing the manufacturing cost. Considering these criteria, the final design shown in Fig's 34, 35 and 36 with part numbers is reached as a result of many design iterations and topological optimization studies conducted on several conceptual design alternatives to determine the best geometry and material combination.

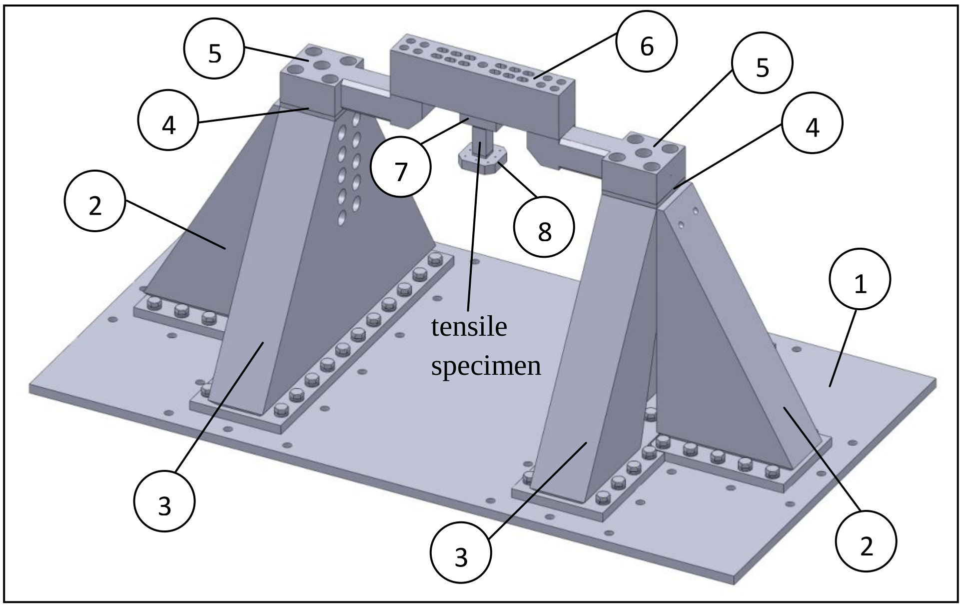

Figure 34. The final design of the test set-up to which tensile specimen is attached

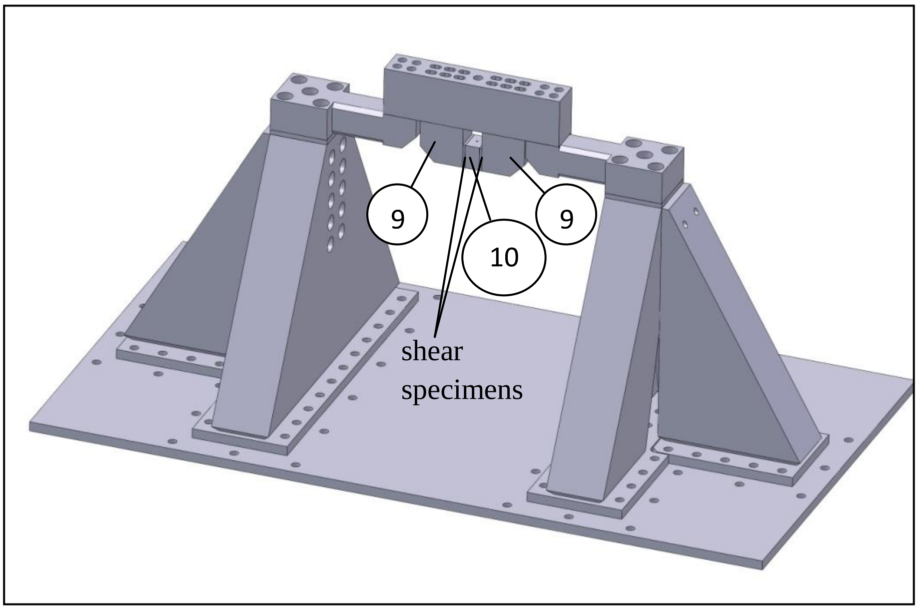

Figure 35. The final design of the test set-up to which shear specimens are attached (Version 1)

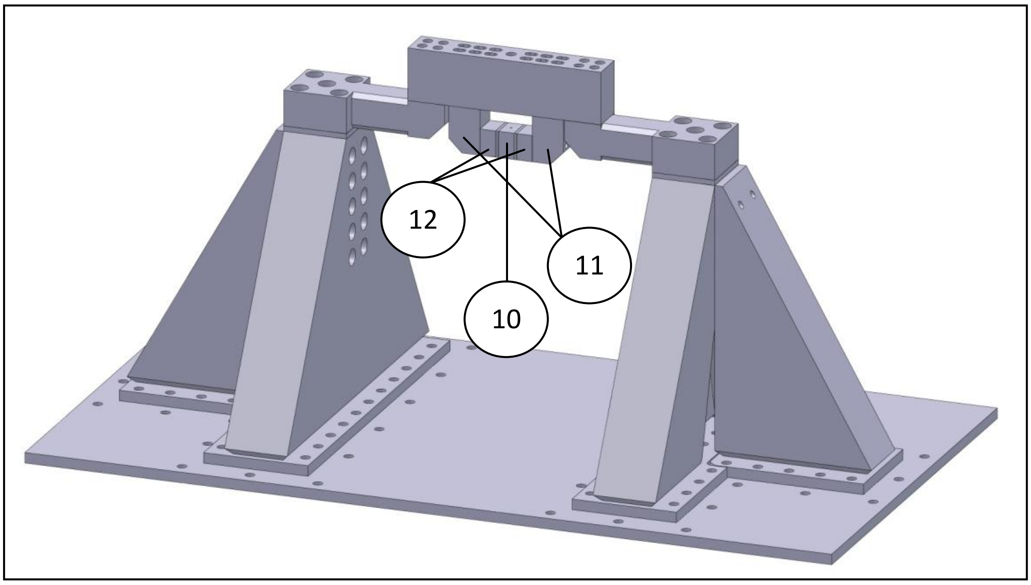

Figure 36. The final design of the test set-up to which shear specimens are attached (Version 2)

The bill of materials for the parts numbered in Fig’s 34, 35 and 36 are given in Table 6.

Table 6. Bill of materials of the test set-up

PART NO	PART NAME	MATERIAL	QUANTITY
1	Base Plate	Aluminum	1
2	Lateral Support (Welded)	Aluminum	2
3	Vertical Support (Welded)	Aluminum	2
4	Thermal Isolation Plate	Steel	2
5	Side Hole Extension	Steel	2
6	Holder for Tensile & Shear Specimen Assembly	Aluminum	1
7	Tensile Specimen Base Block	Stainless Steel	1
8	Tensile Specimen Vibrating Block	Stainless Steel	1
9	Side Block for Shear Specimen	Stainless Steel	2
10	Center Block for Shear Specimen	Stainless Steel	1
11	Side Block for Shear Specimen v2	Aluminum	2
12	Connector for Shear Specimen Side Block v2	Stainless Steel	2

In version 1 of the test set-up to which shear specimens are attached, which is shown in Fig.35, self adhesive materials and/or materials that can be temporarily bonded to the side blocks and the center block are tested. On the other hand, in version 2 of the test set-up to which shear specimens are attached, which is shown in Fig.36, materials that are required to be permanently bonded, for example specimens produced by injection molding, are tested. In this version for every double-shear specimen, a center block and a pair of connectors for side block v2 are to be re-manufactured.

It must be remarked that although the holder for tensile and shear specimen assembly (upper block) is designed as shown in Fig's. 34, 35 and 36, it is manufactured with chamfers of 45° angle at the upper left and right edges.

3.3. Improvements on Finite Element Modeling Studies of the Test Set-up for the Best Simulation of Real World Conditions

The initial finite element model of the test set-up prepared using the commercial software package ANSYS-Workbench is based on the following conditions:

- The base plate is omitted from the model.
- The automatically detected contact between the parts of the test set-up is accepted such that the contacting surfaces of the parts are bonded to each other at all nodal points on these surfaces.
- The boundary condition is defined such that the whole bottom surfaces of the lateral and vertical supports are fixed to the ground.

In order to perform a modal analysis with these conditions, the finite element model of the test set-up is to be prepared in advance. For this purpose, a convergence analysis is carried out to determine the optimum meshing parameters in terms of accuracy and computational time and memory usage. The set-up is meshed in ANSYS-Workbench using the special meshing method, MultiZone, in which the geometry is automatically decomposed into mapped (sweepable/sliceable) and free regions. The "Mapped Mesh Type" is selected to be "Hexa/Prism", which provides higher quality and smoother transitioning and the "Free Mesh Type" is selected to be "Hexa Core", which provides faster computational time and better convergence [28]. The side hole extensions have triangular faces, which cause MultiZone meshing method to fail in creating a successful mesh; therefore these faces are further handled with "Mapped Face Meshing", which places a mapped face mesh control on triangular faces for solid models and automatically determines a suitable number of divisions for the edges on the boundary face [28].

For the first iteration the mesh settings are specified such that the "Relevance", which automatically determines the element size and number of elements of the mesh for the whole model, is -20 and the “Relevance Center”, which sets the gauge of the “Relevance”, is medium. The corresponding mesh of the initial finite element model of the test set-up is shown in Fig.37.

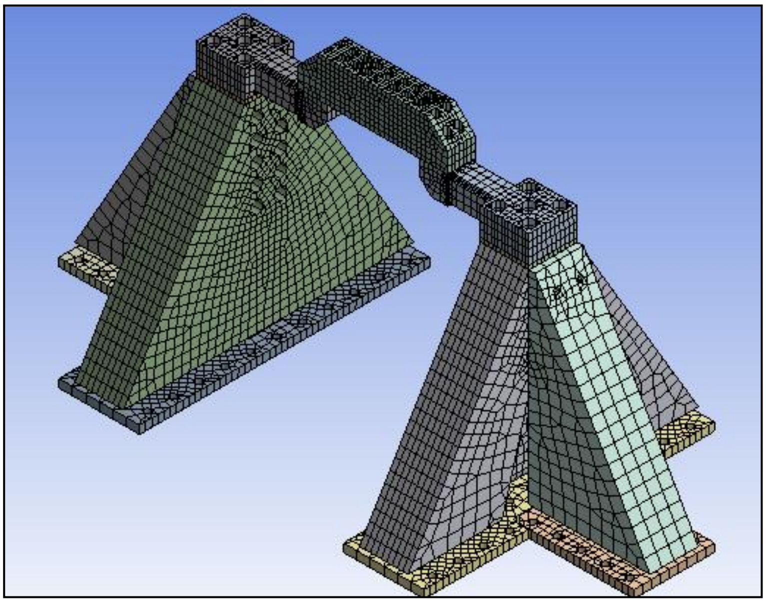

Figure 37. Initial finite element model of the test set-up corresponding to the first iteration for convergence (Number of Elements: 139908; Number of Nodes: 236895; Aspect Ratio (average): 2.95)

The resultant first four modes of this model are obtained as shown in Fig.38.

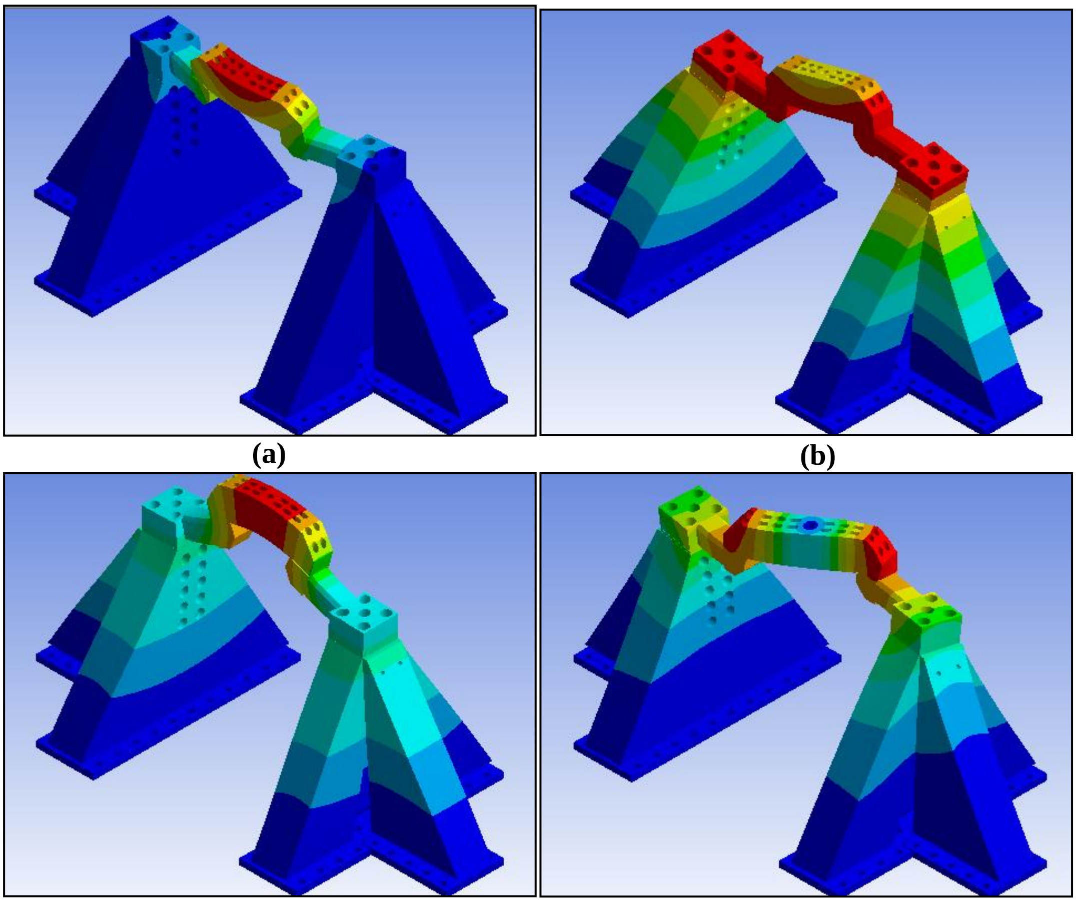

(a) (b) (c) (d)

Figure 38. The mode shapes belonging to the initial finite element model of the test set-up corresponding to the first iteration for convergence: **(a)** 1st mode shape at 520.63 Hz; **(b)** 2nd mode shape at 638.02 Hz; **(c)** 3rd mode shape at 813.72 Hz; **(d)** 4th mode shape at 903.65 Hz

For the second iteration the mesh settings are specified such that the “Relevance” is 0 and the “Relevance Center” is medium. The corresponding mesh of the initial finite element model of the test set-up is shown in Fig.39.

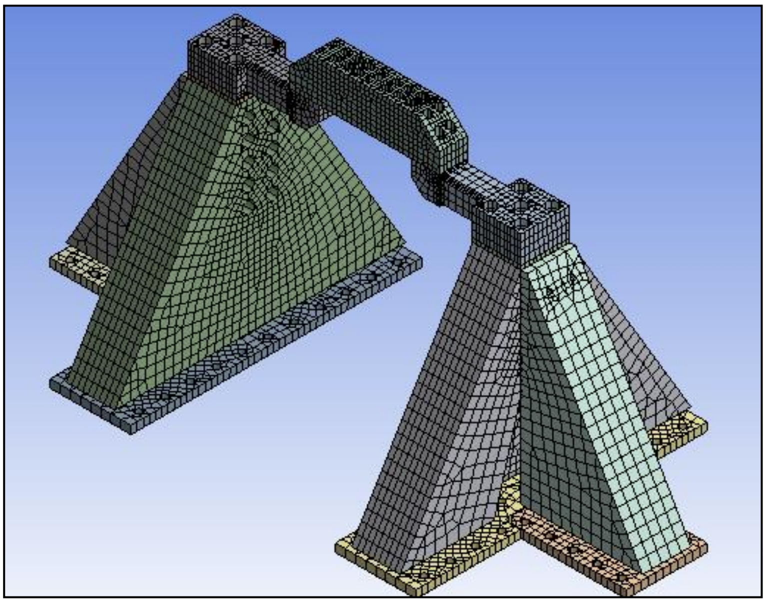

Figure 39. Initial finite element model of the test set-up corresponding to the second iteration for convergence (Number of Elements: 149307; Number of Nodes: 251624; Aspect Ratio (average): 2.86)

The resultant first four mode shapes of this model are the same as the ones corresponding to the first iteration for convergence. However, the corresponding modal frequencies are slightly different as listed in Table 7.

Table 7. The modal frequencies corresponding to the second iteration for convergence

1st modal frequency	520.33 Hz
2nd modal frequency	638.36 Hz
3rd modal frequency	813.41 Hz
4th modal frequency	903.45 Hz

For the third iteration the mesh settings are specified such that the “Relevance” is 20 and the “Relevance Center” is medium. The corresponding mesh of the initial finite element model of the test set-up is shown in Fig.40.

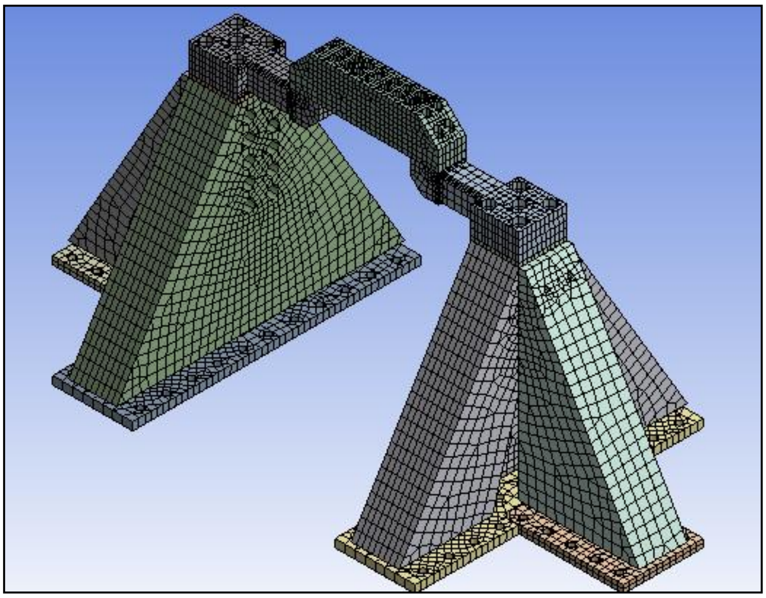

Figure 40. Initial finite element model of the test set-up corresponding to the third iteration for convergence (Number of Elements: 157551; Number of Nodes: 266275; Aspect Ratio (average): 2.79)

The resultant first four mode shapes of this model are the same as the ones corresponding to the first and second iterations for convergence. However, the corresponding modal frequencies are the lowest of all three iterations as listed in Table 8.

Table 8. The modal frequencies corresponding to the third iteration for convergence

1st modal frequency	520.21 Hz
2nd modal frequency	637.96 Hz
3rd modal frequency	812.97 Hz
4th modal frequency	903.25 Hz

To conclude, the modal frequencies belonging to the first four modes of the initial finite element model of the test set-up converge to the ones listed in Table 9.

Table 9. The modal frequencies belonging to the first four modes of the initial finite element model of the test set-up

1st modal frequency	520 Hz
2nd modal frequency	637 Hz
3rd modal frequency	812 Hz
4th modal frequency	903 Hz

In real, however, the conditions of the test set-up are rather different than those of this finite element model as stated in the following:

- The base plate is a bulky part such that its own compliance is possible to have a significant effect on the modes of the test set-up. Therefore, it is more accurate to model the test set-up with the base plate. Including the base plate in the model, the boundary condition of the test set-up is to be such that the bottom surface of the base plate is fixed to the ground only at certain regions around the holes on the base plate through which the bolts to mount the test set-up to the ground are intended to pass rather than fixing the whole bottom surface of the base plate.

- In real, like the mounting of the whole test set-up to ground with bolts, the parts of the test set-up are assembled to each other by using bolts together with washers, i.e., the contact between mating surfaces of the parts occurs only at certain regions around the holes to be bolted. Therefore, it is better to redefine the contact relations between the parts considering the bolted connections so that the parts are not bonded to each other at all nodal points on the contacting surfaces.

- The ground onto which the test set-up is mounted is a concrete block which has also its own compliance, which may affect the modes of the test set-up. Therefore, it is better to investigate this case by adding the 3-D model of the ground to that of the test set-up. The boundary condition of the model of the ground is better be defined as an elastic foundation in 3 orthogonal axes representing the characteristics of the soil onto which the test laboratory is built.

3.3.1. Finite Element Modeling Study of the Test Set-up with the Base Plate Included

In this study the base plate is included in the finite element model of the test set-up, and the test set-up is designed such that the base plate is mounted to ground using hex-head bolts together with washers. This type of joint which uses threaded holes rather than nuts is composed of three contact regions as shown in Fig.41 [23].

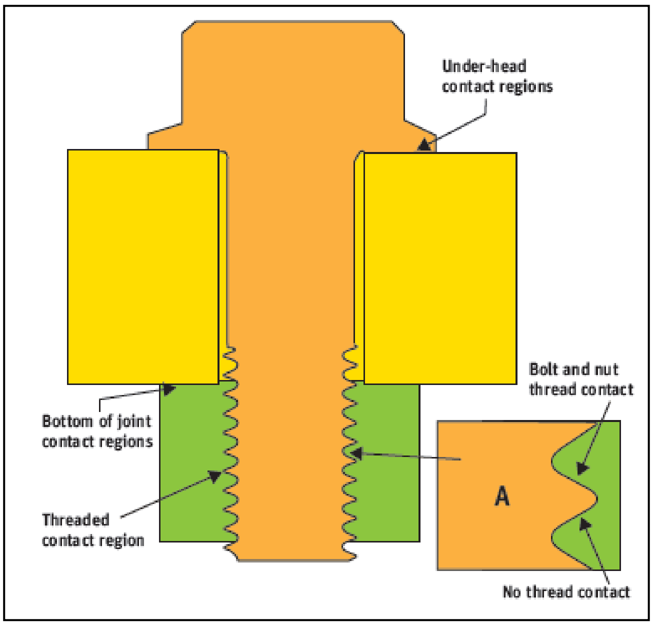

Figure 41. Representation of a bolted-joint using a threaded hole with three contact regions (The view A shows the details of the threaded contact region) [23]

In a generic finite element model of two parts connected to each other with a bolted-joint, the most realistic way is to keep the bolt in the model as a solid body and well-define the contact behavior between the parts and the bolt considering the contacting and non-contacting surfaces between the threads of the bolt and those of the hole on the associated part as well as the distinct frictional behavior at contact regions. However, due to the limitation of computational time and memory usage it is highly difficult to analyze a large and complex structure of multiple parts with detailed modeling of numerous bolted-joints [22, 23].

There are four basic finite element modeling methods for modeling two parts connected with a bolted-joint: (1) A simplified solid bolt model; (2) A coupled bolt model; (3) A spider bolt model; (4) No-bolt model [22]. These modeling methods are depicted in Fig.42 for a bolted joint using a nut.

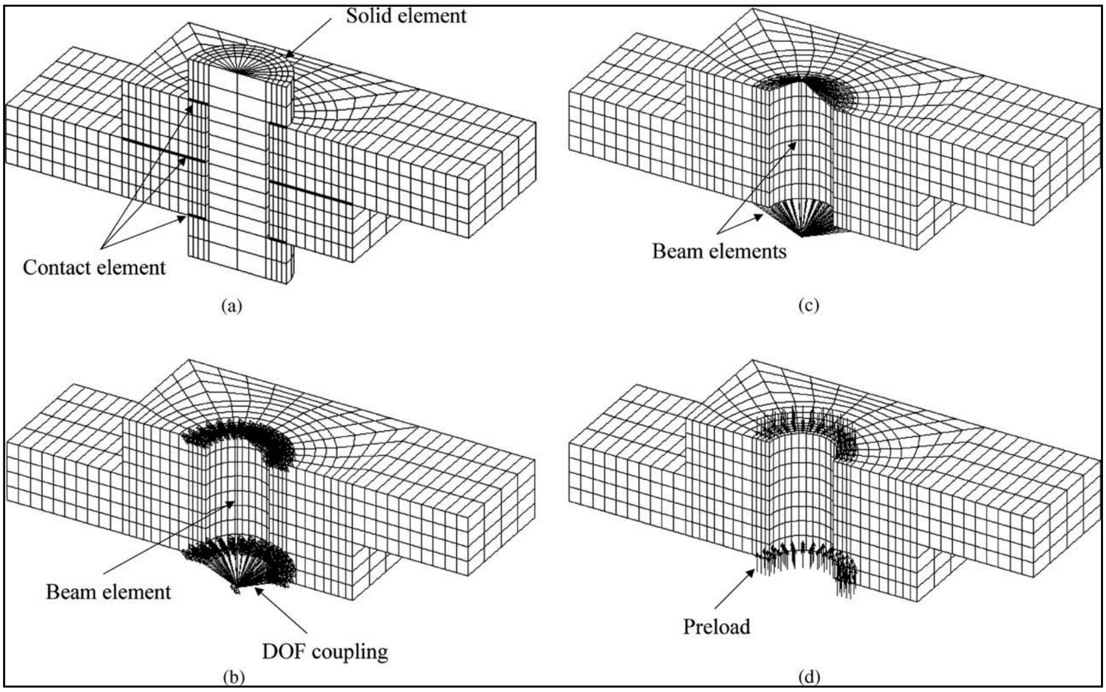

Figure 42. The basic finite element modeling methods for a bolted-joint: (a) A simplified solid bolt model; (b) A coupled bolt model; (c) A spider bolt model; (d) No-bolt model [22]

In the simplified solid bolt model, the bolt (both the head and the stud) and the nut are modeled with 3-D solid elements and to define the contact relations surface-to-surface contact elements between the head of the bolt/the nut and the parts and between the parts themselves are employed. The threads are ignored; however the friction at contact regions can be incorporated by selecting proper contact elements in this simplified model. In the coupled bolt model, the stud of the bolt is represented with a beam element and the end nodes of the beam element are coupled with the nodes at the contact surfaces between the head of the bolt/the nut and the parts. In the spider bolt model, the head and the stud of the bolt and the nut are all represented by beam elements. In the no-bolt model, the bolt (and the nut) is omitted from the model; therefore, this model is the simplest bolt modeling method in terms of computational time and memory usage. However, in this model the bolt stiffness is not taken into account and it is assumed that the parts do not separate [22, 24].

Since it is the simplest way of bolted-joint modeling in terms of computational time and memory usage, the no-bolt model is decided to be used to model the bolted-joint between the base plate of the test set-up and the ground. To define the contact relation between the base plate and the ground, it is necessary to determine the sizes of the contact regions around the holes through which the bolts are intended to pass. For this purpose, the conventional pressure cone method, which estimates the pressure distribution within the bolted-joint that ensures the compression of the joined parts against each other due to clamping, is used, as shown in Fig.43 [3].

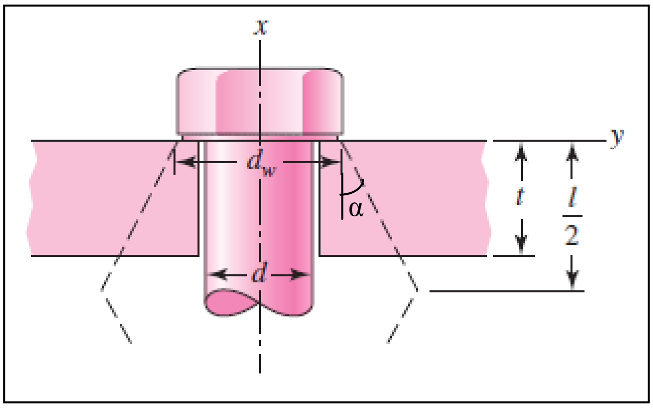

Figure 43. The pressure cone for a bolted-joint where l: effective grip length; d_w: washer outer diameter; d: bolt nominal diameter; t: thickness of one part; α: half-apex angle of the cone [3]

It is recommended that $\alpha = 30°$. The effective grip length for bolted-joints using threaded holes, as shown in Fig.44, is formulated as [3]:

$$l' = \begin{cases} h + \dfrac{t_2}{2}, & t_2 < d \\ h + \dfrac{d}{2}, & t_2 \geq d \end{cases} \quad \text{... (Eqn.16)}$$

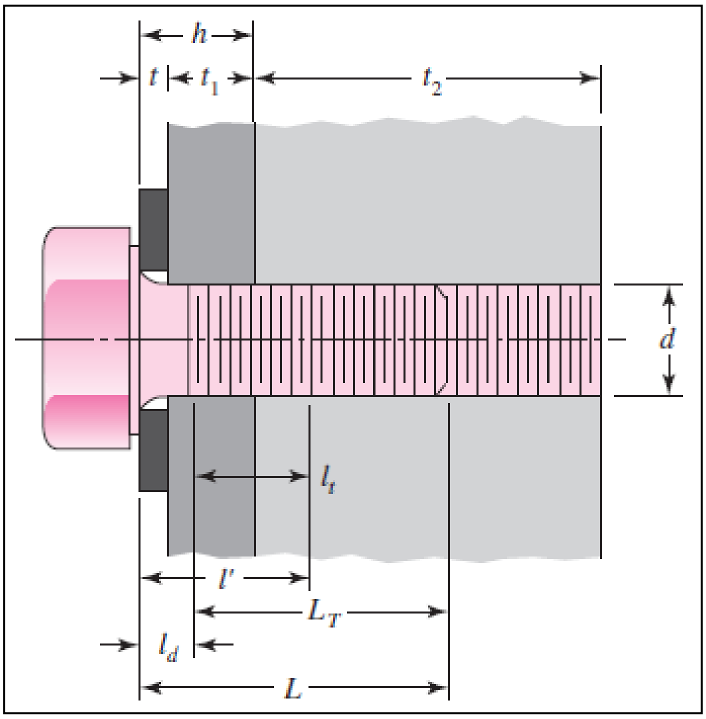

Figure 44. A bolted-joint using a threaded hole where l': effective grip length; L_T: threaded length of the bolt; L: total length of the bolt; l_d: unthreaded length of the bolt; l_t: threaded portion of the effective grip length; t: thickness of the washer; t_1: thickness of the part without the threaded hole; t_2: thickness of the part with the threaded hole; $h = t + t_1$ [3]

It is sure that the size of one of the contact regions between the base plate and the ground is equal to the size of the pressure cone's cross-section at the bottom surface of the base plate around the corresponding hole. Using all this information, the size of the identical contact regions between the base plate and the ground is easily determined: To join the base plate to the ground ISO 4017 hex-head M16 bolts are used. For M16 bolts the sizes of an ISO 7092 metric flat washer are as follows: the outer diameter = 28 mm; the inner diameter = 17 mm; the thickness = 2.5 mm [27]. The thickness of the base plate is 20 mm while the thickness of the ground is indefinite. Then, t = 2.5 mm; t_1 = 20 mm; t_2 = indefinite; d = 16 mm, and as a result h = 22.5 mm; $t_2 \geq$ d. Therefore, the effective grip length is calculated as l' = 22.5 + 16/2 = 30.5 mm. With all this information, it is determined with the help of Fig.43 that one of the identical contact regions at which the base plate is to be bonded to the ground is a hollow circular area with inner diameter of 17 mm and outer diameter of approximately 40 mm. The contact regions in the form of hollow circular areas at the bottom surface of the base plate around the holes are shown in Fig.45 as surfaces with thickness of 10^{-9} mm generated in ANSYS-Workbench.

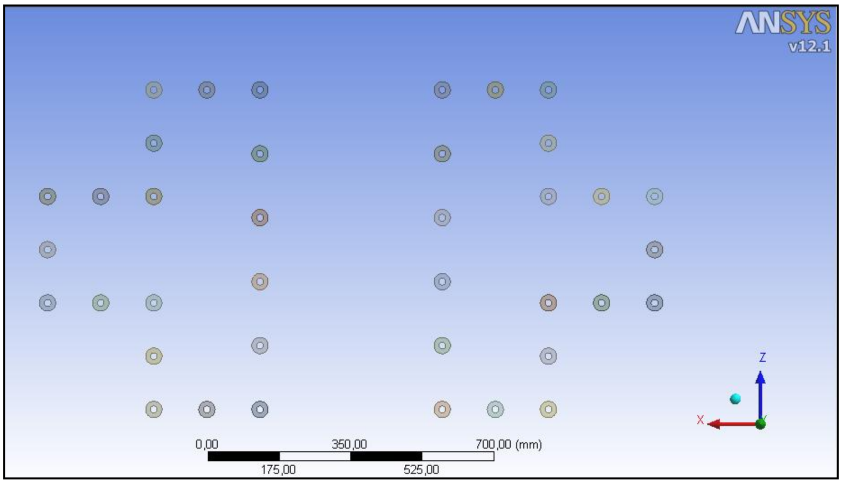

Figure 45. Representation of the contact regions in the form of hollow circular areas at the bottom surface of the base plate around the holes

In order to bond the base plate to the ground only at the contact regions shown in Fig.45 rather than at all nodal points on the bottom surface of the base plate, fixed body-to-ground joints are introduced in ANSYS-Workbench at the bottom surface of the base plate around the holes to accommodate the bolts. For this purpose, the user friendly “Pinball Region” setting is used with a radius value assigned to be equal to that of the corresponding contact region. The pinball regions for the holes to be bolted to the ground on one of the corners of the base plate are shown in Fig.46.

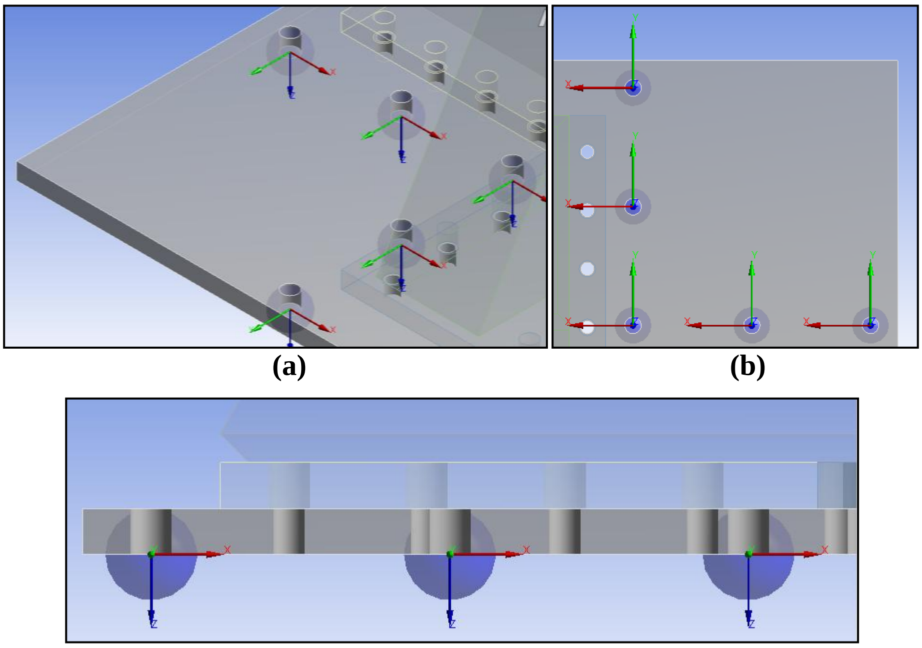

(a) (b)

(c)

Figure 46. The pinball regions for the holes to be bolted to the ground on one of the corners of the base plate: **(a)** Isometric view; **(b)** Top view; **(c)** Front view

In addition, the contact between the lateral and vertical supports and the plates to which they are welded is modified such that the supports and the plates are bonded to each other only at surfaces to which welding is applied, as shown in Fig.47.

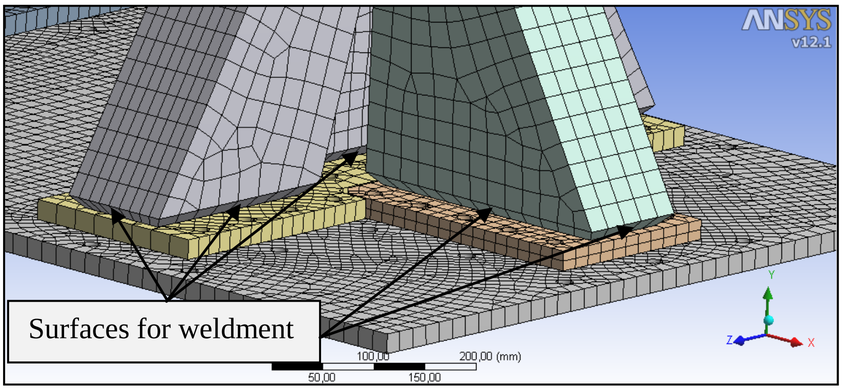

Figure 47. The Finite Element Model of the Test Set-up with the Base Plate (MultiZone Mesh; Relevance: 20; Relevance Center: Medium; Number of Nodes: 318385; Number of Elements: 161794; Aspect Ratio (average): 2.76)

The 1st, 3rd, 4th and 5th modes of this model are obtained such that only the corners of the base plate deform, and the frequencies of these modes are in the range of 377.32 Hz – 389.36 Hz. The 7th and 8th modes, which occur at 510.44 Hz and 541.84 Hz, respectively, also belong to the deformation of only the base plate such that the middle region of the base plate deforms this time. The remaining modes up to 10th mode belong to the structural deformation of the whole test set-up, as shown in Fig.48.

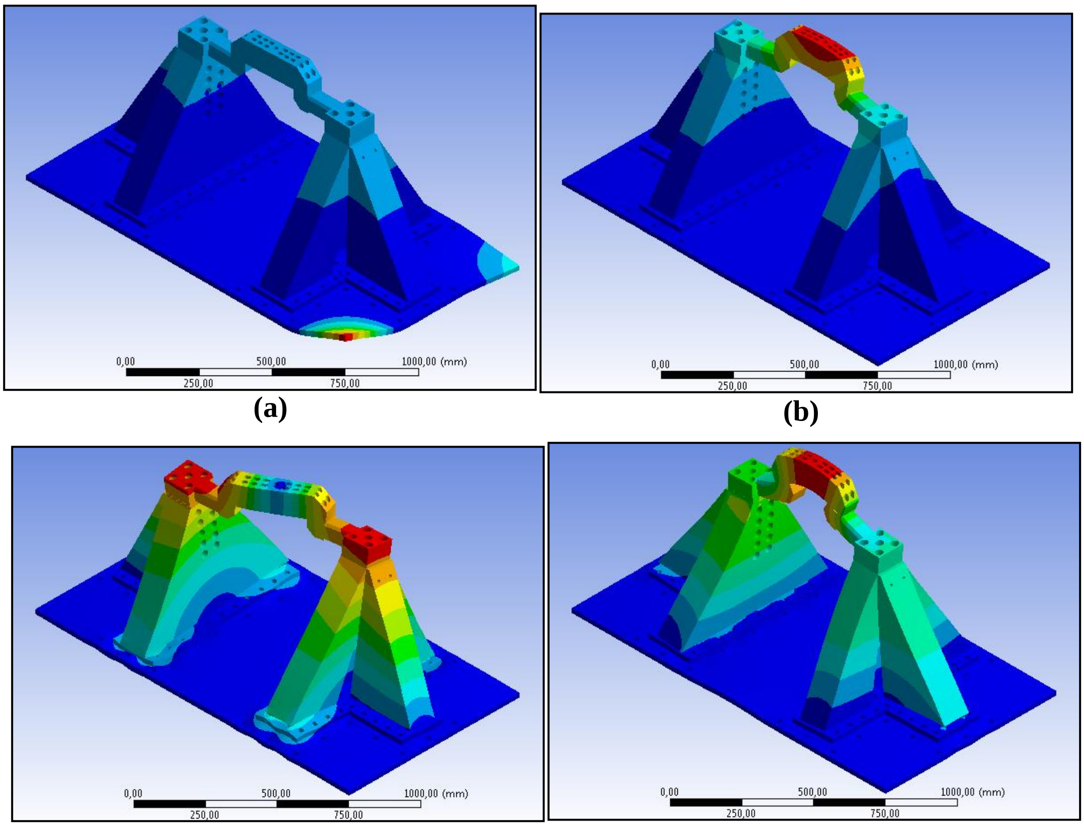

(a) **(b)**

(c) **(d)**

Figure 48. The mode shapes corresponding to the finite element model of the test set-up with the base plate: **(a)** 2nd mode shape at 378.67 Hz; **(b)** 6th mode shape at 444.91 Hz; **(c)** 9th mode shape at 576.37 Hz; **(d)** 10th mode shape at 611.22 Hz

When the modal analysis results of the finite element model with the base plate where the bottom surface of the base plate is fixed to the ground only at certain regions around the holes through which the bolts to mount the base plate to the ground are intended to pass are investigated, it is clearly seen that the frequencies at which the structural modes of the whole test set-up occur (disregarding the local modes of the base plate) are quite lower than the ones for the finite element model without the base plate. In addition, when the mode shapes are compared, it is seen that the mode order has changed as such: 1st structural mode of the test set-up without the base plate corresponds to the 2nd structural mode of the *whole* test set-up with the base plate (6th mode in Fig.48). 2nd structural mode of the test set-up without the base plate corresponds to the 1st structural mode of the *whole* test set-up with the base plate (2nd mode in Fig.48). 3rd structural mode of the test set-up without the base plate corresponds to the 4th structural mode of the *whole* test set-up with the base plate (10th mode in Fig.48). 4th structural mode of the test set-up without the base plate corresponds to the 3rd structural mode of the *whole* test set-up with the base plate (9th mode in Fig.48). Nevertheless, regardless of the mode order change, it can easily be said that the first structural modal frequency of the *whole* test set-up has dropped dramatically from 520 Hz to 379 Hz, which corresponds to an approximately 27% decrease.

3.3.2. Finite Element Modeling Study of the Test Set-up Considering the Bolted-Joints between the Parts

The parts of the test set-up are designed to be assembled to each other by using bolts together with washers, and these bolted-joints involve hex-head and socket-head bolts using threaded holes rather than nuts as in the case of mounting of the base plate to the ground. Due to the same reason of saving computational time and memory usage, the no-bolt model is decided to be used to model also the bolted-joints between the parts of the test set-up. In order to determine the sizes of the contact regions at the mating surfaces of the parts around the holes for accommodating the bolts, and therefore to define the contact relations between the parts of the test set-up, the same procedure as in the case of mounting of the base plate to the ground is followed.

To join the vertical and lateral supports to the base plate ISO 4017 hex-head M16 bolts are used. The thickness of one of the plates to which the vertical and lateral supports are welded is 20 mm while the thickness of the base plate is also 20 mm. Then, $t = 2.5$ mm; $t_1 = 20$ mm; $t_2 = 20$ mm; $d = 16$ mm, and as a result $h = 22.5$ mm; $t_2 \geq d$. Therefore, the effective grip length is calculated as $l' = 22.5 + 16/2 = 30.5$ mm. With all this information, it is determined with the help of Fig.43 that the contact region at which the parts are to be bonded is a hollow circular area with inner diameter of 17 mm and outer diameter of approximately 40 mm. To join the vertical and lateral supports to each other ISO 4762 socket-head M16 bolts are used. The thickness of the vertical support in the direction of the joint when the counter-bore depth is subtracted is 50 mm while the thickness of the lateral support in the direction of the joint is greater than 30 mm. Then, $t = 2.5$ mm; $t_1 = 50$ mm; $t_2 > 30$ mm; $d = 16$ mm, and as a result $h = 52.5$ mm; $t_2 \geq d$. Therefore, the effective grip length is calculated as $l' = 52.5 + 16/2 = 60.5$ mm. With all this information, it is determined with the help of Fig.43 that the contact region at which the parts are to be bonded is a hollow circular area with inner diameter of 17 mm and outer diameter of approximately 40 mm. To join the side hole extension, thermal isolation plate and vertical support to each other ISO 4762 socket-head M16 bolts are used again. The thickness of the side hole extension in the direction of the joint when the counter-bore depth is subtracted is 20 mm while the thickness of the thermal isolation plate is 10 mm and the thickness of the vertical support in the direction of the joint is greater than 25 mm. Then, $t = 2.5$ mm; $t_1 = 20 + 10 = 30$ mm (since both the side hole extension and the thermal isolation plate have unthreaded holes); $t_2 > 25$ mm; $d = 16$ mm, and as a result $h = 32.5$ mm; $t_2 \geq d$. Therefore, the effective grip length is calculated as $l' = 32.5 + 16/2 = 40.5$ mm. With all this information, it is determined with the help of Fig.43 that the contact region at which the side hole extension and the thermal isolation plate are to be bonded is a hollow circular area with inner diameter of 17 mm and outer diameter of approximately 51 mm while the contact region at which the thermal isolation plate and the vertical support are to be bonded is a hollow circular area with inner diameter of 17 mm and outer diameter of approximately 40 mm. Finally, to join the holder for tensile & shear specimen assembly to the side hole extension ISO 4762 socket-head M8 bolts are used. For M8 bolts the sizes of an ISO 7092 metric flat washer are as follows: the outer diameter = 15 mm; the inner diameter = 8.4 mm; the thickness = 1.6 mm [27]. The thickness of the holder for tensile & shear specimen assembly in the direction of the joint when the counter-bore depth is subtracted is 20 mm while the thickness of the side hole extension in the direction of the joint is greater than 25 mm. Then, $t = 1.6$ mm; $t_1 = 20$ mm; $t_2 > 25$ mm; $d = 8$ mm, and as a result $h = 21.6$ mm; $t_2 \geq d$. Therefore, the effective grip length is calculated as $l' = 21.6 + 8/2 = 25.6$ mm. With all this information, it is determined with the help of Fig.43 that the contact region at which the parts are to be bonded is a hollow circular area with inner diameter of 8.4 mm and outer diameter of approximately 22 mm.

Now that the sizes of the contact regions in the form of hollow circular areas between all mating parts of the test set-up are determined, these regions are generated as surfaces with thickness of 10^{-9} mm at each contacting surface of the test set-up around the holes on the parts in ANSYS-Workbench for the purpose of demonstration, as shown in Fig.49.

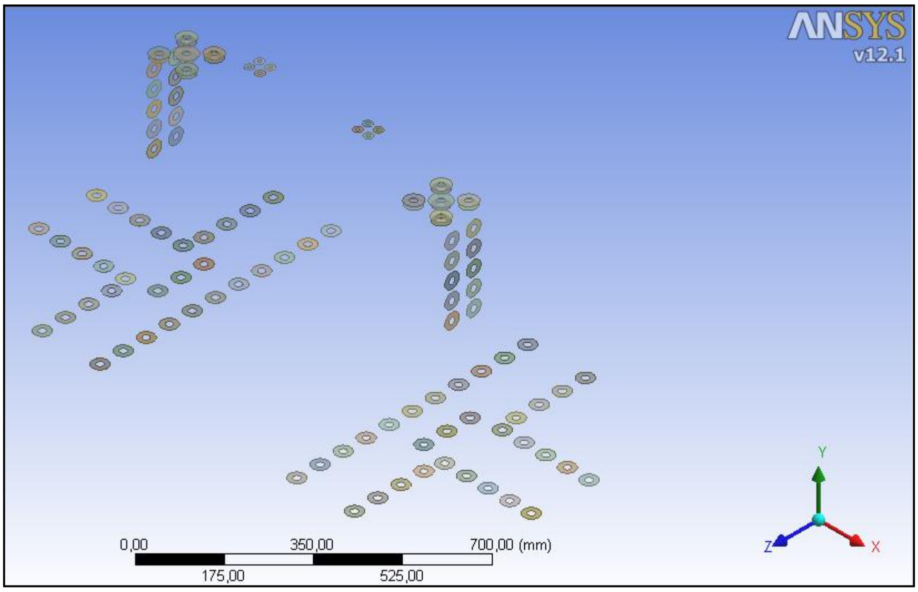

Figure 49. Representation of the contact regions in the form of hollow circular areas at the contacting surfaces of parts of the test set-up around the mating holes

In order to bond the mating parts of the test set-up to each other only at the contact regions shown in Fig.49 rather than at all nodal points on the contacting surfaces, fixed body-to-body joints are introduced in ANSYS-Workbench between the contacting surfaces of the parts of the test set-up around the holes on the parts for accommodating the bolts. For this purpose, the pinball region setting is used again with a radius value assigned to be equal to that of the corresponding contact region. By this way, the DOF of the nodes located at the contacting surfaces of the parts of the test set-up within the defined pinball regions are coupled to each other such that the relative motion between them in 3-D space is all prevented. The pinball regions for the holes to be bolted to each other on the vertical and lateral supports are shown in Fig.50 as an example.

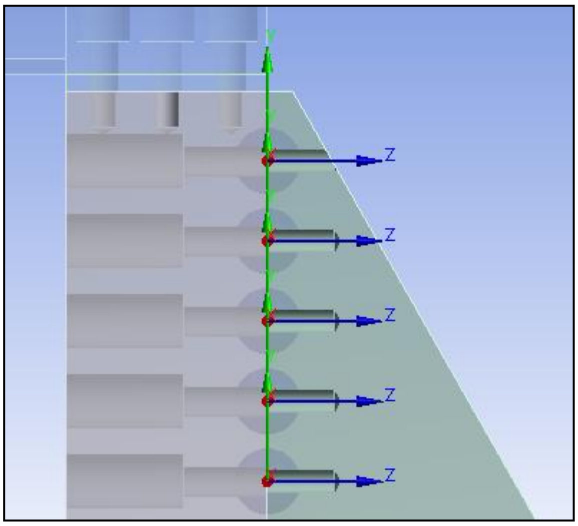

Figure 50. The pinball regions for the holes to be bolted to each other on the vertical and lateral supports – Front view

A modal analysis is performed with the finite element model of the test set-up shown in Fig.51 with mating parts bonded to each other only at the given contact regions. It must be noted that the boundary condition, which is realized by bolting the base plate of the test set-up to the ground as mentioned beforehand, is still modeled with fixed body-to-ground joints using pinball region setting.

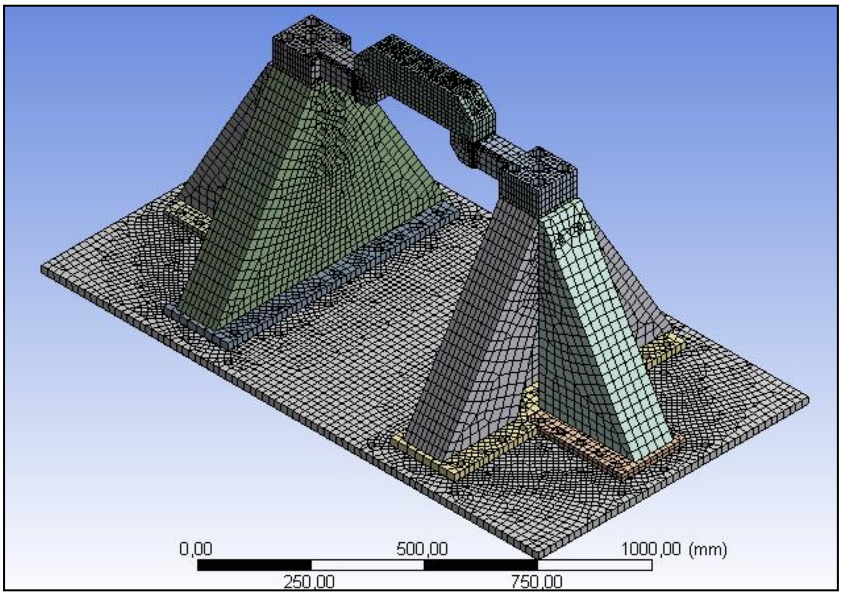

Figure 51. Finite element model of the test set-up with the base plate considering the bolted-joints between the parts (MultiZone Mesh; Relevance: 20; Relevance Center: Medium; Number of Nodes: 318385; Number of Elements: 161794; Aspect Ratio (average): 2.76)

The results of the modal analysis are such that the 3rd, 4th, 5th and 6th modes of this model belong to the deformation of only the corners of the base plate with the corresponding frequencies in the range of 377.07 Hz – 389.03 Hz, as expected. The 10th mode, which occurs at 540.55 Hz, also belongs to the deformation of only the base plate such that the middle region of the base plate deforms this time, as expected. The remaining modes up to 10th mode belong to the structural deformation of the whole test set-up, as shown in Fig.52.

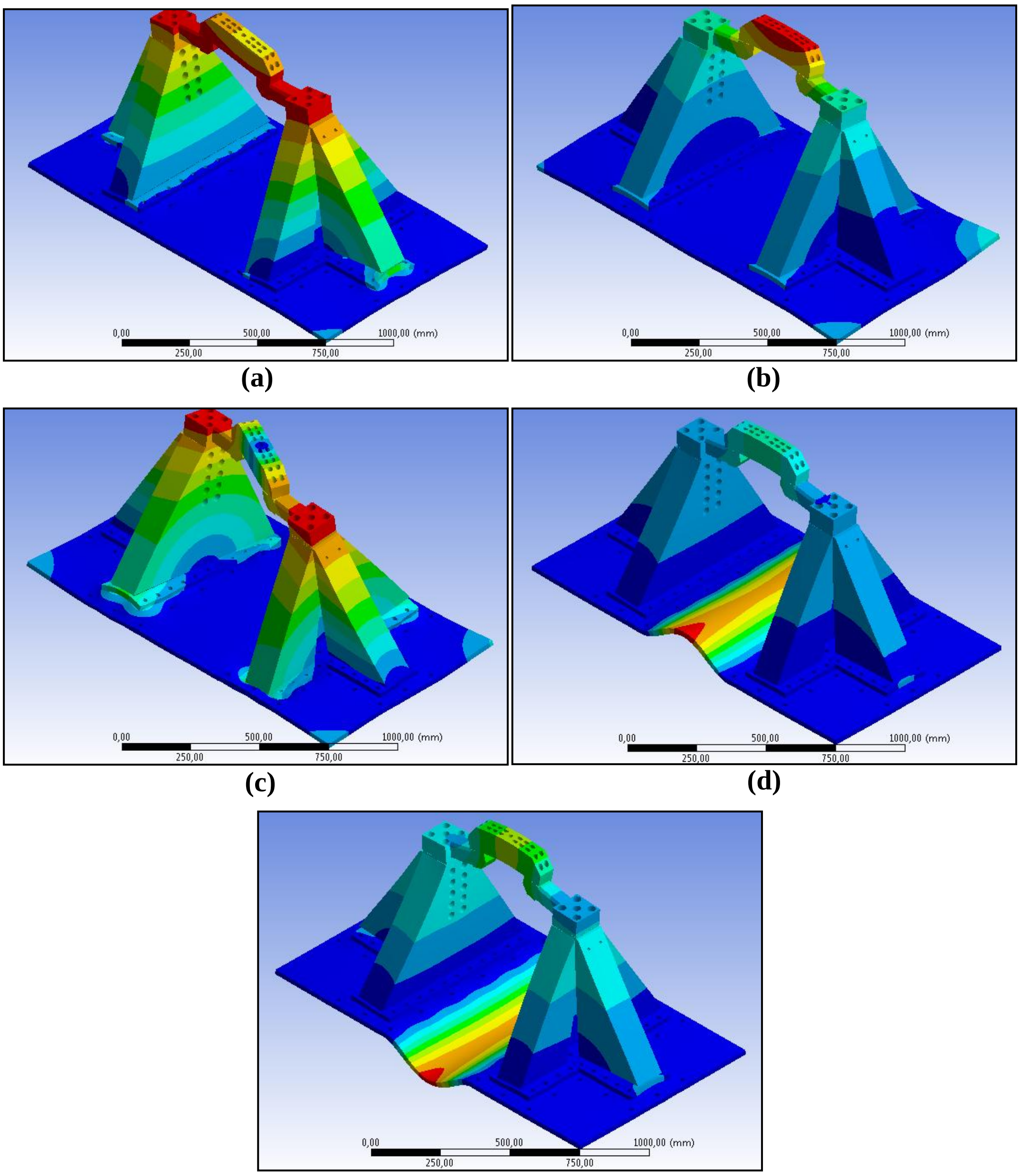

(a) (b) (c) (d) (e)

Figure 52. The mode shapes corresponding to the finite element model of the test set-up with the base plate considering the bolted-joints between the parts: **(a)** 1st mode shape at 286.06 Hz; **(b)** 2nd mode shape at 361.82 Hz; **(c)** 7th mode shape at 433.22 Hz; **(d)** 8th mode shape at 507.39 Hz; **(e)** 9th mode shape at 511.12 Hz

When the modal analysis results of the finite element model of the test set-up with the base plate where the mating parts of the test set-up are bonded to each other at certain contact regions around the holes on the parts through which the bolts are intended to pass are investigated, it is clearly seen that the frequencies at which the structural modes of the whole test set-up occur (disregarding the local modes of the base plate) are quite lower than the ones for the previous finite element model of the test set-up with the base plate, which does not take the bolted-joints between the parts into consideration. It must also be stated that the mode order has not changed this time. Since the latest model is closer to the real world conditions, it can easily be said that the first structural modal frequency of the *whole* test set-up has further decreased from 379 Hz to 286 Hz, which corresponds to an approximately 25% decrease.

3.3.3. Finite Element Modeling Study of the Test Set-up with 3-D Model of the Ground onto which the Test Set-up is Mounted Added

The ground onto which the test set-up is mounted is indeed a concrete block which has its own compliance. To see the effect of the ground's compliance on the modes of the test set-up, a 3-D model of the ground in the shape of a rectangular prism is added to that of the test set-up. Instead of fixed body-to-ground joints introduced at the bottom surface of the base plate around the holes beforehand, fixed body-to-body joints are introduced this time at the contacting surfaces of the base plate and the concrete block around the holes to be bolted to each other. For this purpose, pinball region setting is used again with a radius value assigned to be equal to that of the corresponding contact region determined between the base plate and the ground beforehand. It is realized that in the assembly phase of the base plate to the ground, not all the holes on the base plate are inserted bolts to mount the base plate to the ground. The used holes on the base plate are indicated with circles in Fig.53.

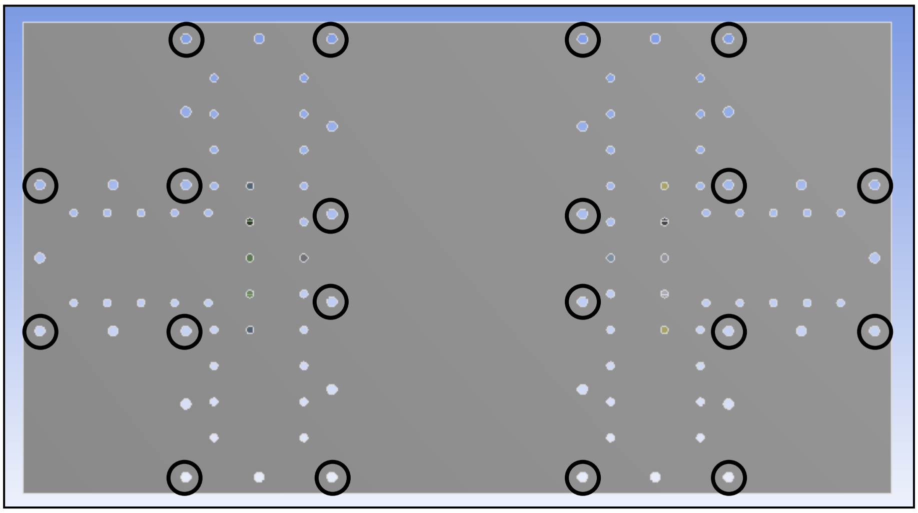

Figure 53. The holes on the base plate which are inserted bolts to mount the base plate to the ground (those which are circled)

The corresponding pinball regions on one of the corners of the base plate and the concrete block are shown in Fig.54.

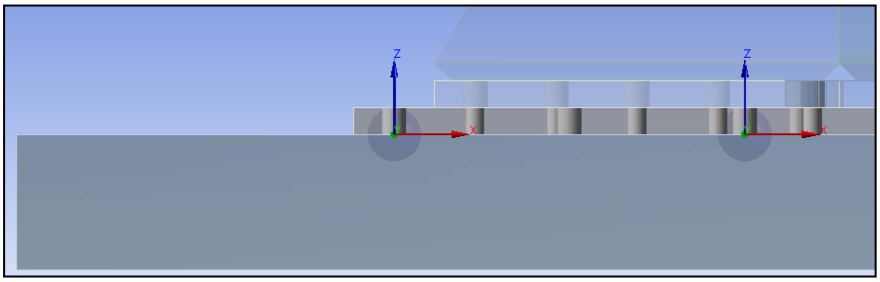

Figure 54. The pinball regions for the holes to be bolted to each other on one of the corners of the base plate and the concrete block representing the compliant ground – Front view

It is known approximately that the concrete block is 100 mm wider than the base plate in both frontward and backward directions and 250 mm wider than the base plate in both rightward and leftward directions; however the dimension in the vertical direction, i.e. the thickness of the concrete block is unknown. Therefore, as an initial assumption the thickness of the rectangular prism representing the concrete block is assigned the value of 100 mm. In addition, the boundary condition of the concrete block is modeled such that except for the top surface onto which the test set-up is mounted, all other surfaces are supported with elastic foundations. Before pouring the concrete, some part of the test laboratory is excavated to form a mold for the concrete block and the excavated area is filled with sand up to a certain level. Therefore, the lateral areas of the concrete block are directly adhered to the soil onto which the test laboratory is built whereas there is a layer of sand between the concrete block and the soil. For this reason, the stiffness of the elastic foundation supporting the bottom surface of the concrete block is taken to be lower than that of the elastic foundation supporting the side surfaces of the concrete block. Since these stiffness values are not possible to be known, they will be estimated. As an initial assumption, the bottom surface of the concrete block is supported with an elastic foundation with a stiffness value of 10^{-2} N/mm^3 whereas the side surfaces of the concrete block are supported with elastic foundations with a common stiffness value of 10^{-1} N/mm^3. Also, the concrete block is initially assigned the predefined Young's modulus value of 3×10^{10} Pa in ANSYS Workbench's built-in material library.

With all these details, a modal analysis is performed with the finite element model of the test set-up with 3-D model of the ground shown in Fig.55.

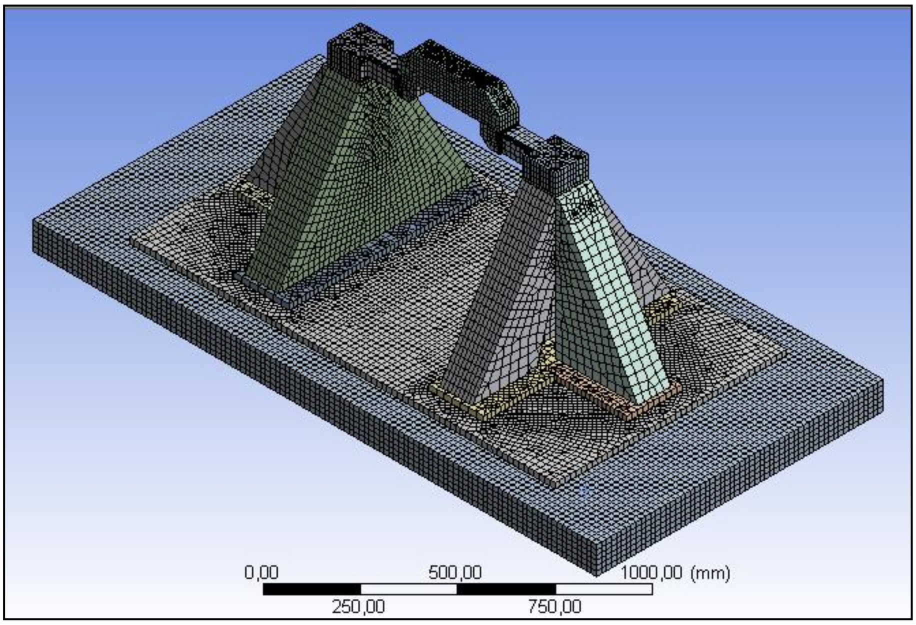

Figure 55. Finite Element Model of the Test Set-up with the Concrete Block Representing the Compliant Ground (Thickness of the concrete block is 100 mm.) (MultiZone Mesh; Relevance: 20; Relevance Center: Medium; Element Size of the Concrete Block: 18 mm; Number of Nodes: 487021; Number of Elements: 193934; Aspect Ratio (average): 2.50)

The results of the modal analysis which cover 12 modes in the frequency range of 40 Hz – 400 Hz are as such: The 8th, 9th and 10th modes of this model in the given frequency range belong to the deformation of only the corners of the base plate with the corresponding frequencies in the range of 346.77 Hz – 353.52 Hz. The remaining modes belong to the structural deformation of the whole test set-up and the 3-D model of the ground, as shown in Fig.56.

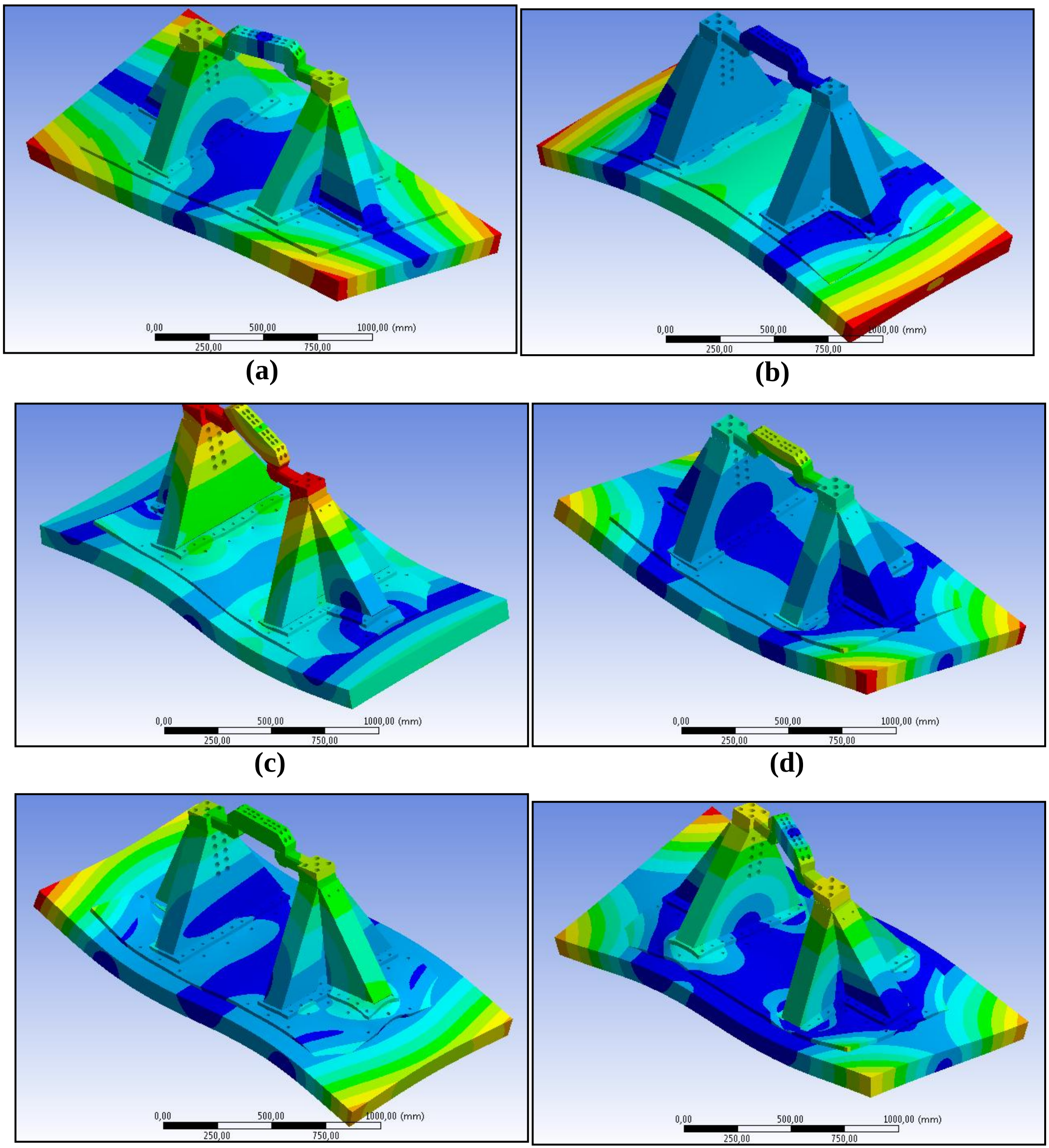

(a) (b)

(c) (d)

(e) (f)

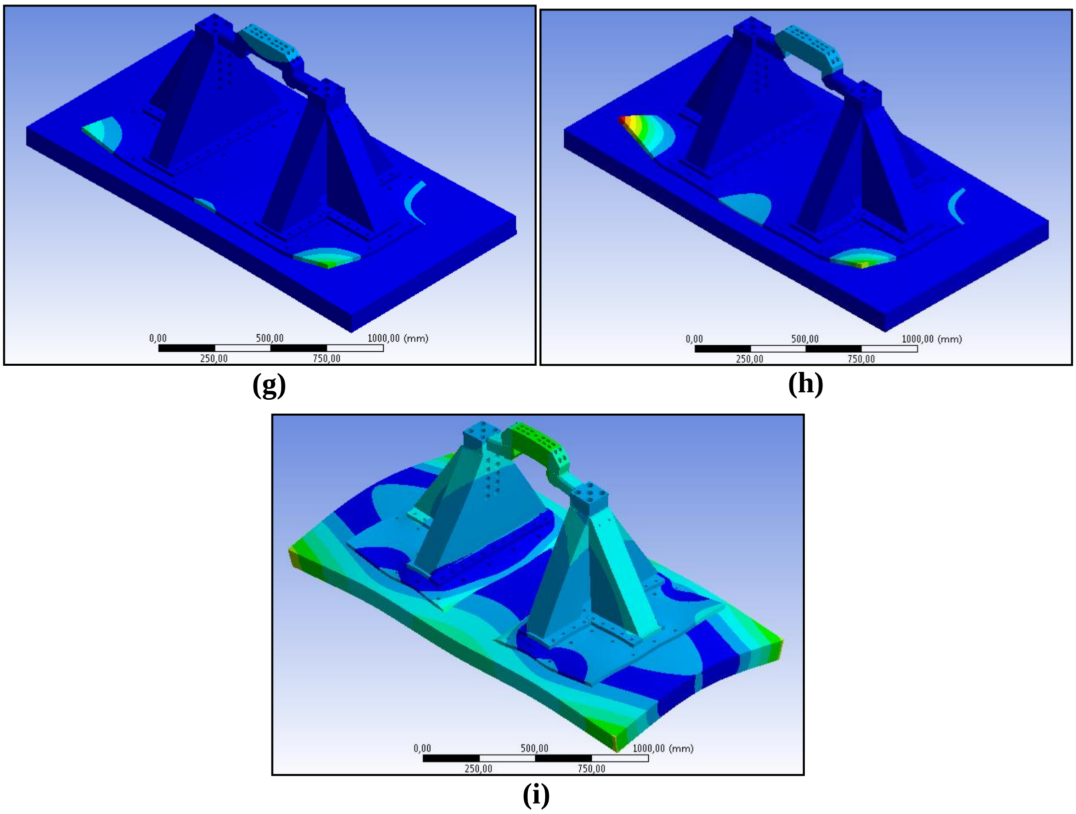

(g) (h)

(i)

Figure 56. The mode shapes corresponding to the finite element model of the test set-up with 3-D model of the ground – first iteration: **(a)** 1st mode shape at 135.74 Hz; **(b)** 2nd mode shape at 165.31 Hz; **(c)** 3rd mode shape at 206.63 Hz; **(d)** 4th mode shape at 248.44 Hz; **(e)** 5th mode shape at 264.9 Hz; **(f)** 6th mode shape at 278.17 Hz; **(g)** 7th mode shape at 338.26 Hz; **(h)** 11th mode shape at 365.91 Hz; **(i)** 12th mode shape at 390.66 Hz

In order to obtain the experimental modal frequencies and the corresponding mode shapes, a modal test is performed on the test set-up installed in the test laboratory. For this purpose, a total number of 30 PCB Piezotronics, Inc. Model 356A32 tri-axial ICP® accelerometers with a nominal sensitivity value of 100 mV/g for each axis are attached on certain points on the upper part of the test set-up, as shown in Fig.57.

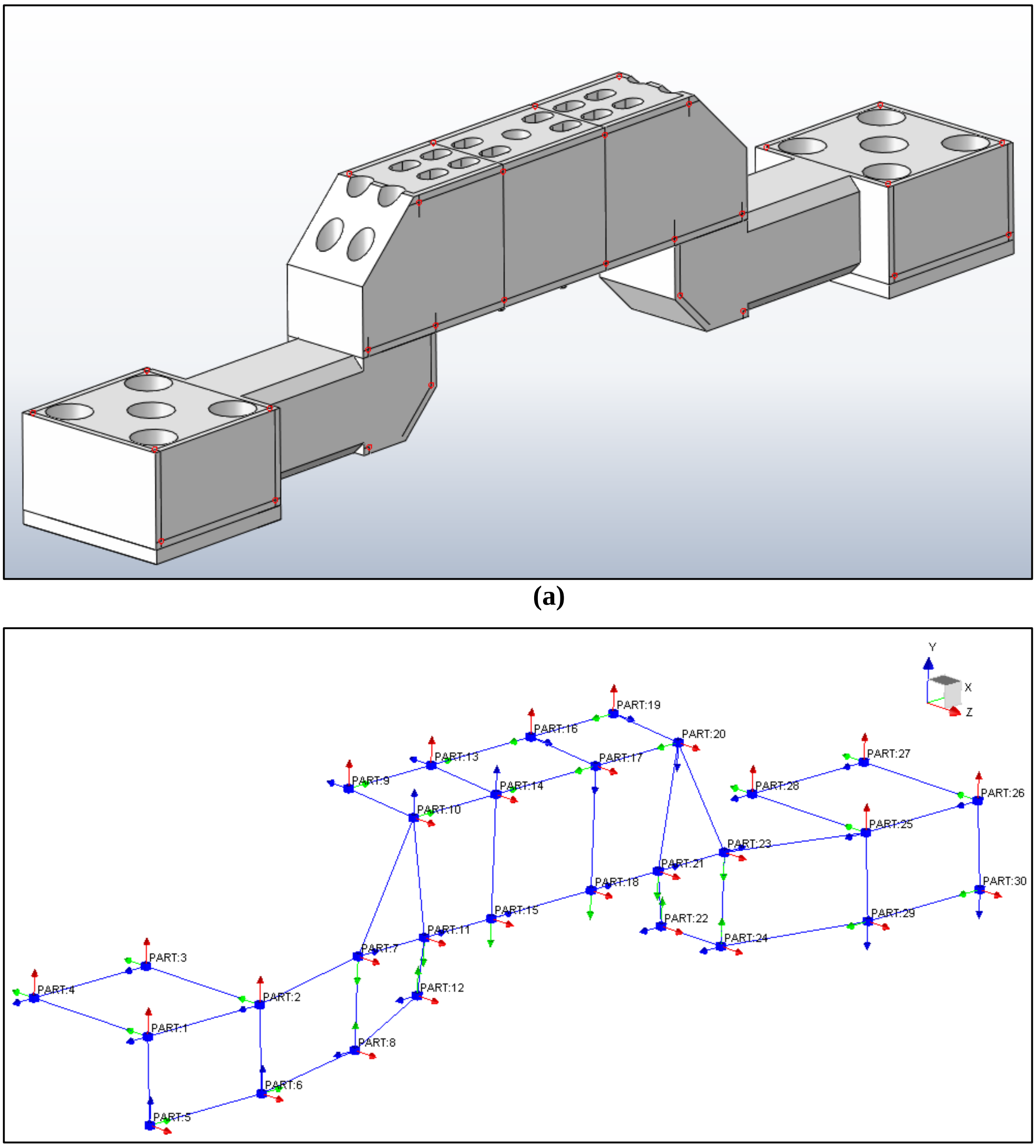

Figure 57. **(a)** Locations of the tri-axial accelerometers to be placed on the upper part of the test set-up; **(b)** Experimental geometric model of the upper part of the test set-up indicating x-, y-, and z-axis of each accelerometer

The upper part of the test set-up is excited by a B&K Model 8206-003 impact hammer with a nominal sensitivity value of 1.1 mV/N at a total number of 10 points which are close to certain pre-attached tri-axial accelerometers, as shown in Fig.58.

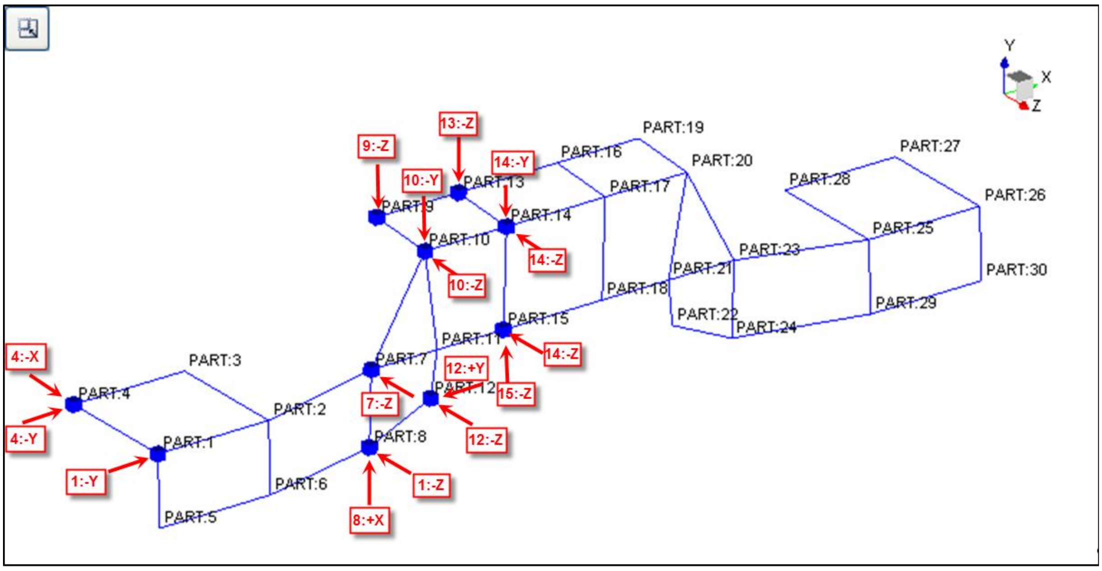

Figure 58. The points at which the upper part of the test set-up is excited by an impact hammer (The directions of excitation are also indicated.)

As can be seen in Fig.58, the upper part of the test set-up is excited in two directions at certain points; therefore a total number of 16 modal tests are performed. LMS Test.Lab is used as the data acquisition and signal processing software for the modal tests, and the settings made on the user interface of the test software for data acquisition and signal processing are shown in Fig.59.

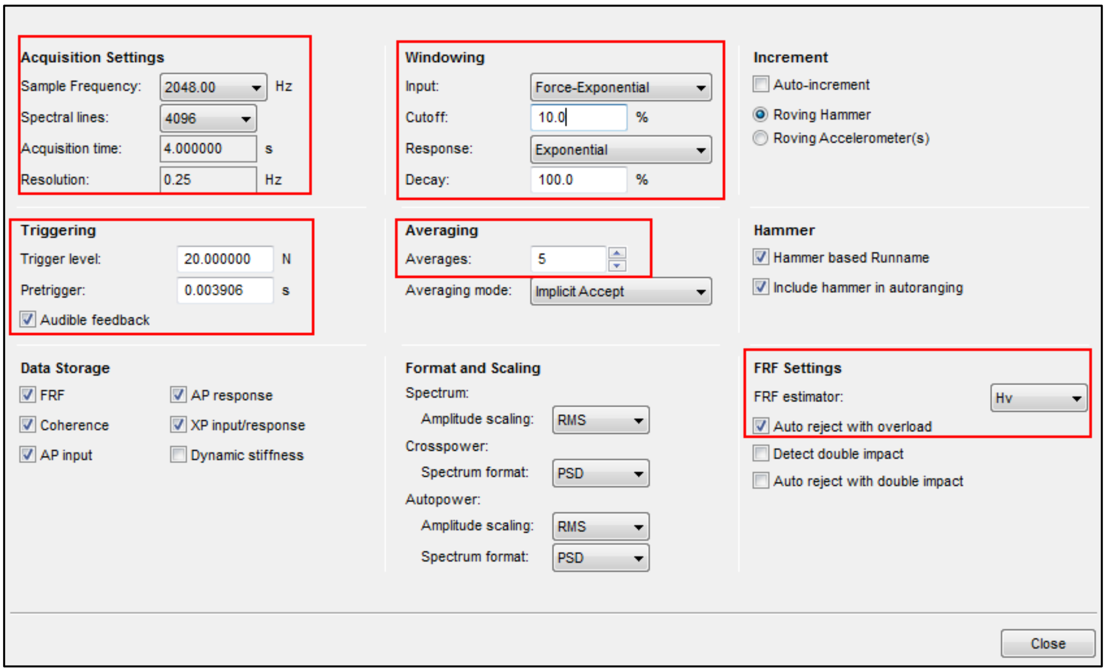

Acquisition Settings
Sample Frequency: 2048.00 Hz
Spectral lines: 4096
Acquisition time: 4.000000 s
Resolution: 0.25 Hz

Windowing
Input: Force-Exponential
Cutoff: 10.0 %
Response: Exponential
Decay: 100.0 %

Increment
☐ Auto-increment
● Roving Hammer
○ Roving Accelerometer(s)

Triggering
Trigger level: 20.000000 N
Pretrigger: 0.003906 s
☑ Audible feedback

Averaging
Averages: 5
Averaging mode: Implicit Accept

Hammer
☑ Hammer based Runname
☑ Include hammer in autoranging

Data Storage
☑ FRF
☑ Coherence
☑ AP input
☑ AP response
☑ XP input/response
☐ Dynamic stiffness

Format and Scaling
Spectrum:
Amplitude scaling: RMS
Crosspower:
Spectrum format: PSD
Autopower:
Amplitude scaling: RMS
Spectrum format: PSD

FRF Settings
FRF estimator: Hv
☑ Auto reject with overload
☐ Detect double impact
☐ Auto reject with double impact

Figure 59. Settings made on LMS Test.Lab user interface for data acquisition and signal processing for modal tests

The auto-power spectral estimate of the excitation induced on the upper part of the test set-up by an impact hammer is shown in Fig.60 for each modal test.

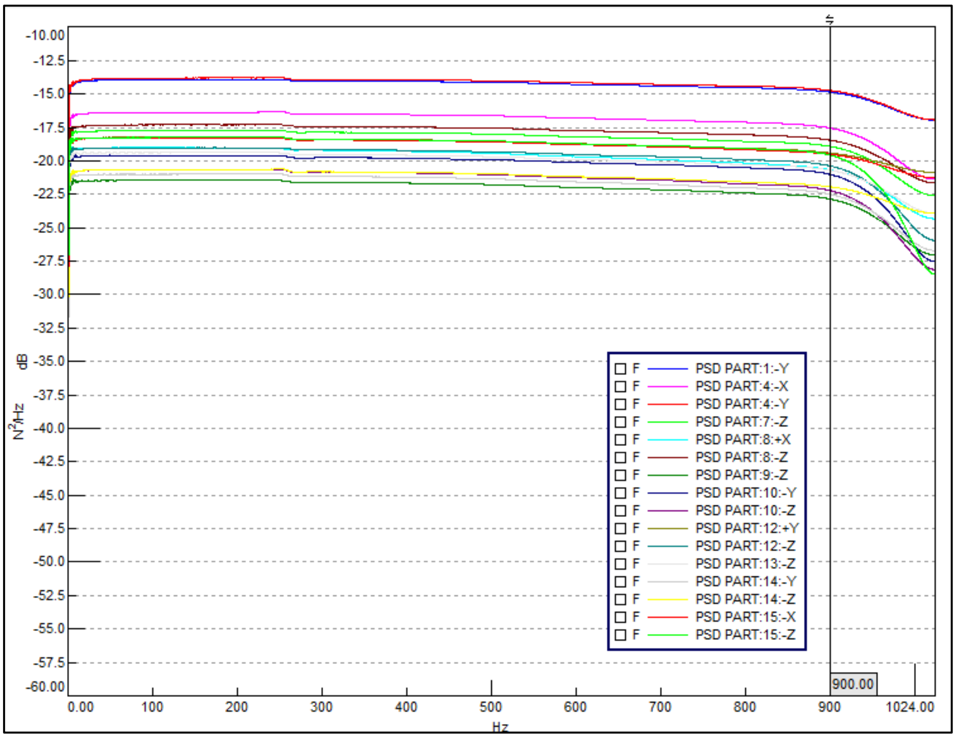

Figure 60. Auto-power spectral estimate of the excitation induced on the upper part of the test set-up by an impact hammer for each modal test

As can be seen in Fig.60, the auto-power spectral estimates of the excitations induced by an impact hammer have almost constant values in the frequency range of approximately 0 Hz – 900 Hz, as expected; therefore the modes of the test set-up up to approximately 1000 Hz are able to be excited in the modal tests. The driving-point FRF of each excitation point obtained at the end of each modal test is shown in Fig.61 with the peaks of the FRF's marked to indicate the possible modal frequencies of the designed test set-up.

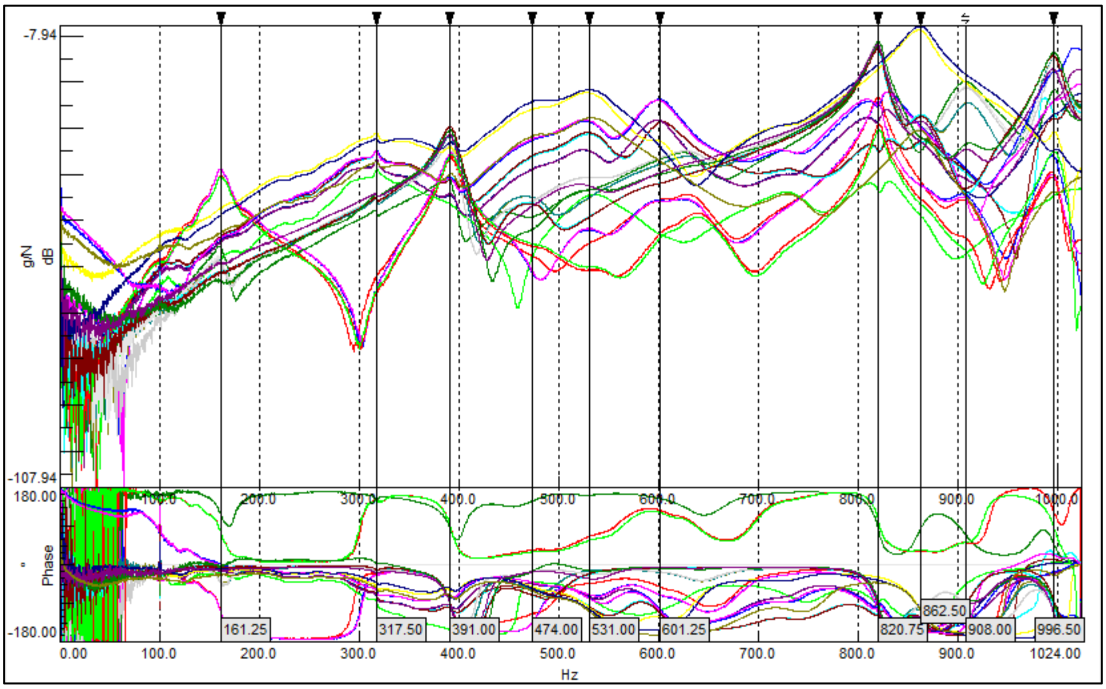

Figure 61. The driving-point FRF of each excitation point obtained at the end of each modal test with the peaks of the FRF's marked to indicate the possible modal frequencies of the designed test set-up

Consequently, the experimental modal frequencies of the designed test set-up obtained as a result of the modal tests are listed in Table 10.

Table 10. Experimental modal frequencies of the designed test set-up obtained as a result of the modal tests

Mode Number	**Modal Frequency (Hz)**
1	162.8
2	317.6
3	393.2
4	439.9
5	474.2
6	479.6
7	530.3
8	601.9
9	629.4
10	823.4
11	862.8
12	904.2

The experimental mode shapes corresponding to the modal frequencies up to 600 Hz are shown in Fig.62.

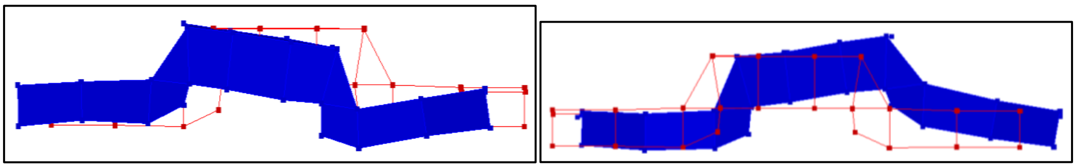

(a)

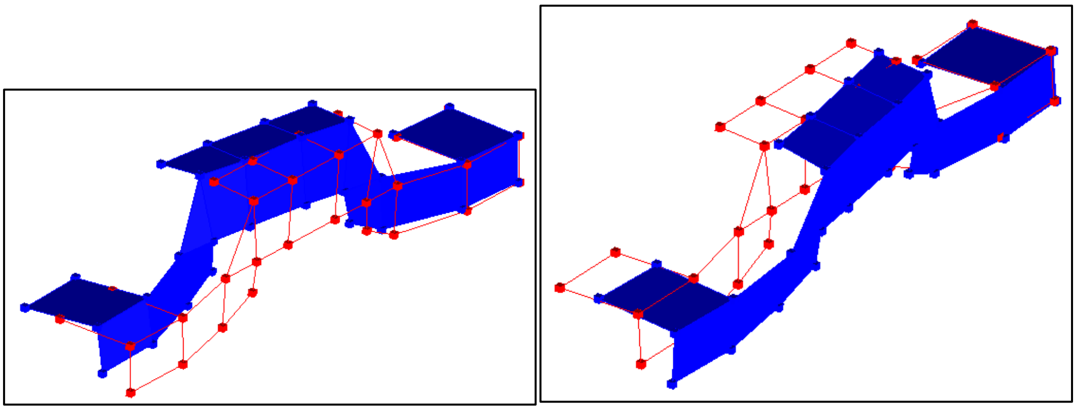

(b)

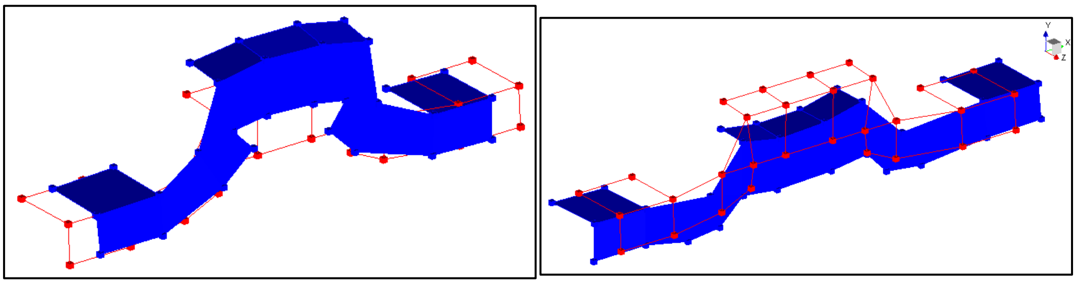

(c)

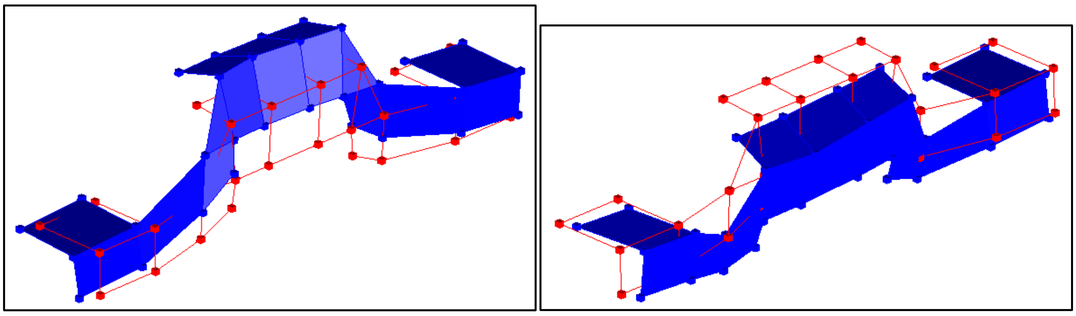

(d)

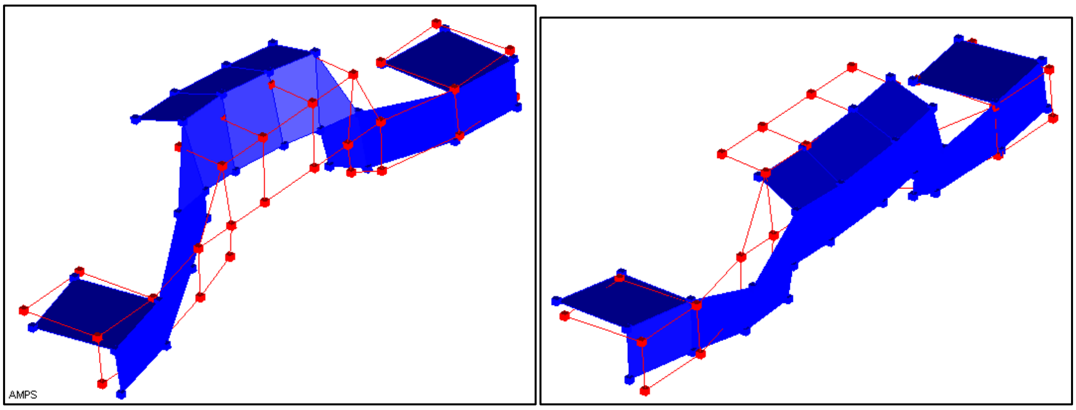

(e)

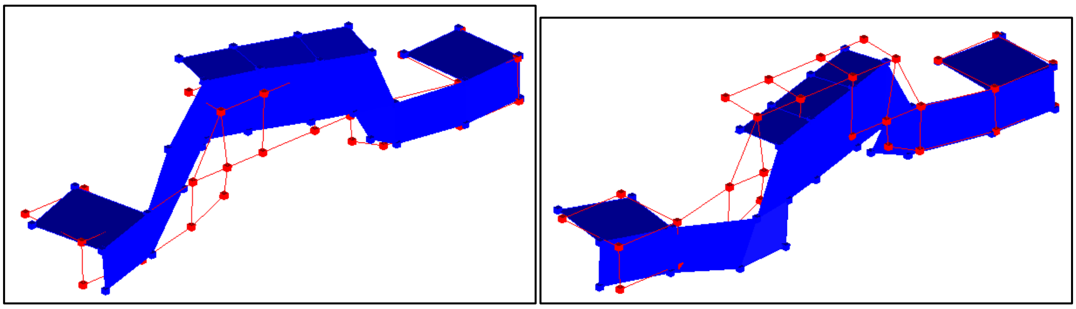

(f)

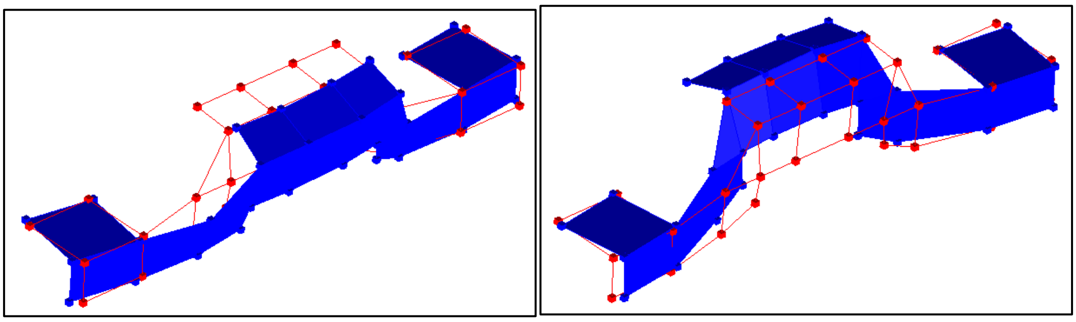

(g)

Figure 62. Experimental mode shapes of the designed test set-up obtained as a result of the modal tests: **(a)** 1st mode shape at 162.8 Hz; **(b)** 2nd mode shape at 317.6 Hz; **(c)** 3rd mode shape at 393.2 Hz; **(d)** 4th mode shape at 439.9 Hz; **(e)** 5th mode shape at 474.2 Hz; **(f)** 6th mode shape at 479.6 Hz; **(g)** 7th mode shape at 530.3 Hz

When the modes of the first iteration of the finite element model of the test set-up with the concrete block are compared with the experimental modes, it can be seen that the 1st modal frequency of the first iteration of the finite element model of the test set-up with the concrete block, which is 135.74 Hz, is lower than the 1st experimental modal frequency, which is 162.8 Hz. Also, the 1st mode shapes do not resemble to each other; instead the 3rd mode shape of the first iteration of the finite element model of the test set-up with the concrete block resembles the 1st experimental mode shape.

In the second iteration, therefore, in order to increase the 1st modal frequency, the stiffness value of the elastic foundation with which the bottom surface of the concrete block is supported is increased to 10^{-1} N/mm^3 and at the same time the common stiffness value of the elastic foundations with which the side surfaces of the concrete block are supported is increased to 10 N/mm^3. By this way, the 3rd mode shape of the first iteration, which is similar to the 1st experimental mode shape, may also become the 1st mode shape. In this iteration, the thickness and Young's modulus of the concrete block remains as 100 mm and $3x10^{10}$ Pa, respectively.

The results of the modal analysis which cover 12 modes in the frequency range of 90 Hz – 360 Hz are as such: The 9th, 10th, 11th and 12th modes of this model in the given frequency range belong to the deformation of only the corners of the base plate with the corresponding frequencies in the range of 347.15 Hz – 359 Hz. The remaining modes belong to the structural deformation of the whole test set-up and the 3-D model of the ground, as shown in Fig.63.

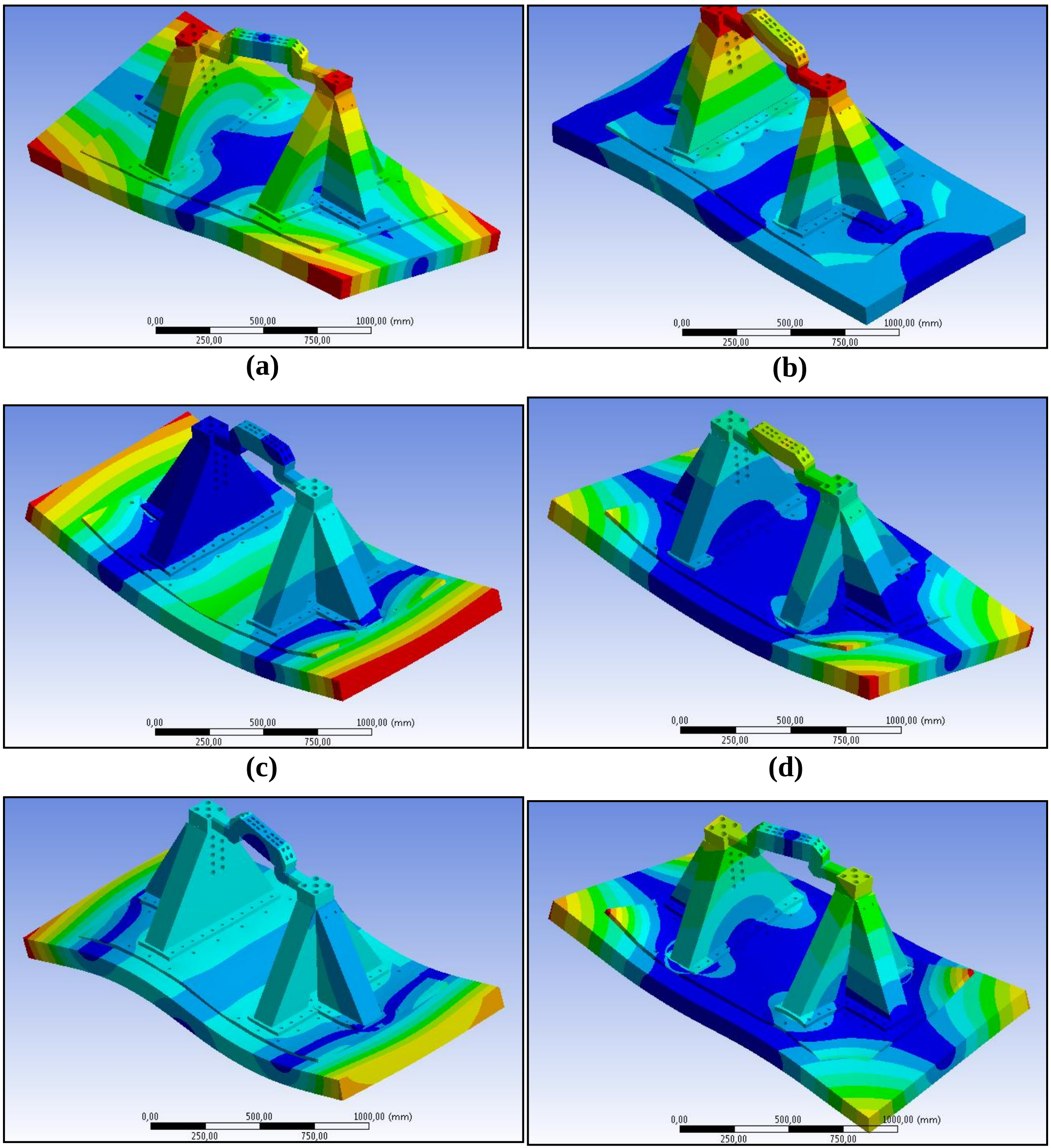

(a) (b)

(c) (d)

(e) (f)

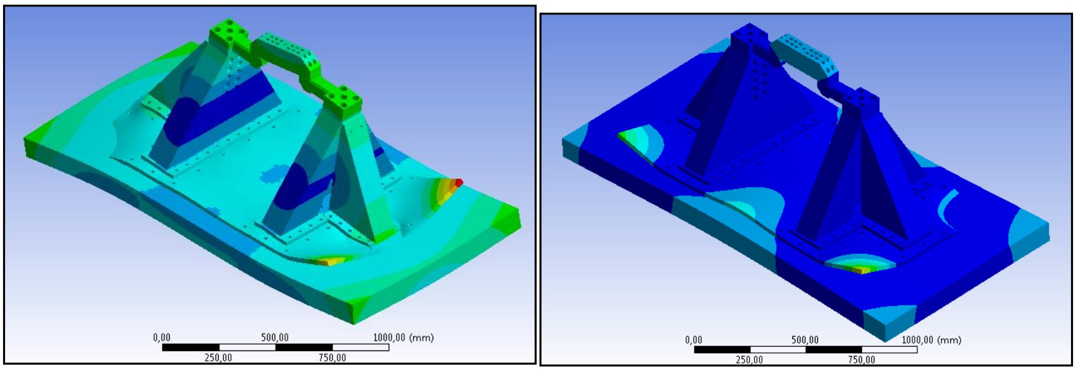

(g) (h)

Figure 63. The mode shapes corresponding to the finite element model of the test set-up with 3-D model of the ground – second iteration: **(a)** 1st mode shape at 157.21 Hz; **(b)** 2nd mode shape at 183.93 Hz; **(c)** 3rd mode shape at 195.5 Hz; **(d)** 4th mode shape at 256.54 Hz; **(e)** 5th mode shape at 265.67 Hz; **(f)** 6th mode shape at 278.36 Hz; **(g)** 7th mode shape at 299.69 Hz; **(h)** 8th mode shape at 335.41 Hz

When the modes of the second iteration of the finite element model of the test set-up with the concrete block are compared with the experimental modes, it can be seen that the 1st modal frequency of the second iteration of the finite element model of the test set-up with the concrete block, which is 157.21 Hz, is still lower than the 1st experimental modal frequency, which is 162.8 Hz. Also, the 1st mode shapes do not resemble to each other; instead the 2nd mode shape of the second iteration of the finite element model of the test set-up with the concrete block, this time, resembles the 1st experimental mode shape.

In the third iteration, it is decided that the common stiffness value of the elastic foundations with which the side surfaces of the concrete block are supported is increased to infinity, i.e. the side surfaces of the concrete block are fixed while the thickness and Young's modulus of the concrete block remains as 100mm and $3\text{x}10^{10}$ Pa, respectively, and also the stiffness value of the elastic foundation with which the bottom surface of the concrete block is supported remains as 10^{-1} N/mm^3. This is done in order to eliminate the low-frequency rigid-body-modes of the test set-up and the concrete block due to elastic support in three orthogonal directions, which are not realistic to occur, and also to minimize the deformation of the concrete block and direct the vibrational energy to the test set-up itself, which is a more realistic behavior. By this way, the 1st modal frequency could further increase, and also the

2nd mode shape of the second iteration, which is similar to the 1st experimental mode shape, may become the 1st mode shape.

The results of the modal analysis which cover 12 modes in the frequency range of 30 Hz – 500 Hz are as such: The 6th, 7th, 8th and 9th modes of this model in the given frequency range belong to the deformation of only the corners of the base plate with the corresponding frequencies in the range of 345.67 Hz – 356.14 Hz. The 12th mode, which occurs at 461.03 Hz, also belongs to the deformation of only the base plate such that the middle region of the base plate deforms this time. The remaining modes belong to the structural deformation of the whole test set-up and the 3-D model of the ground, as shown in Fig.64.

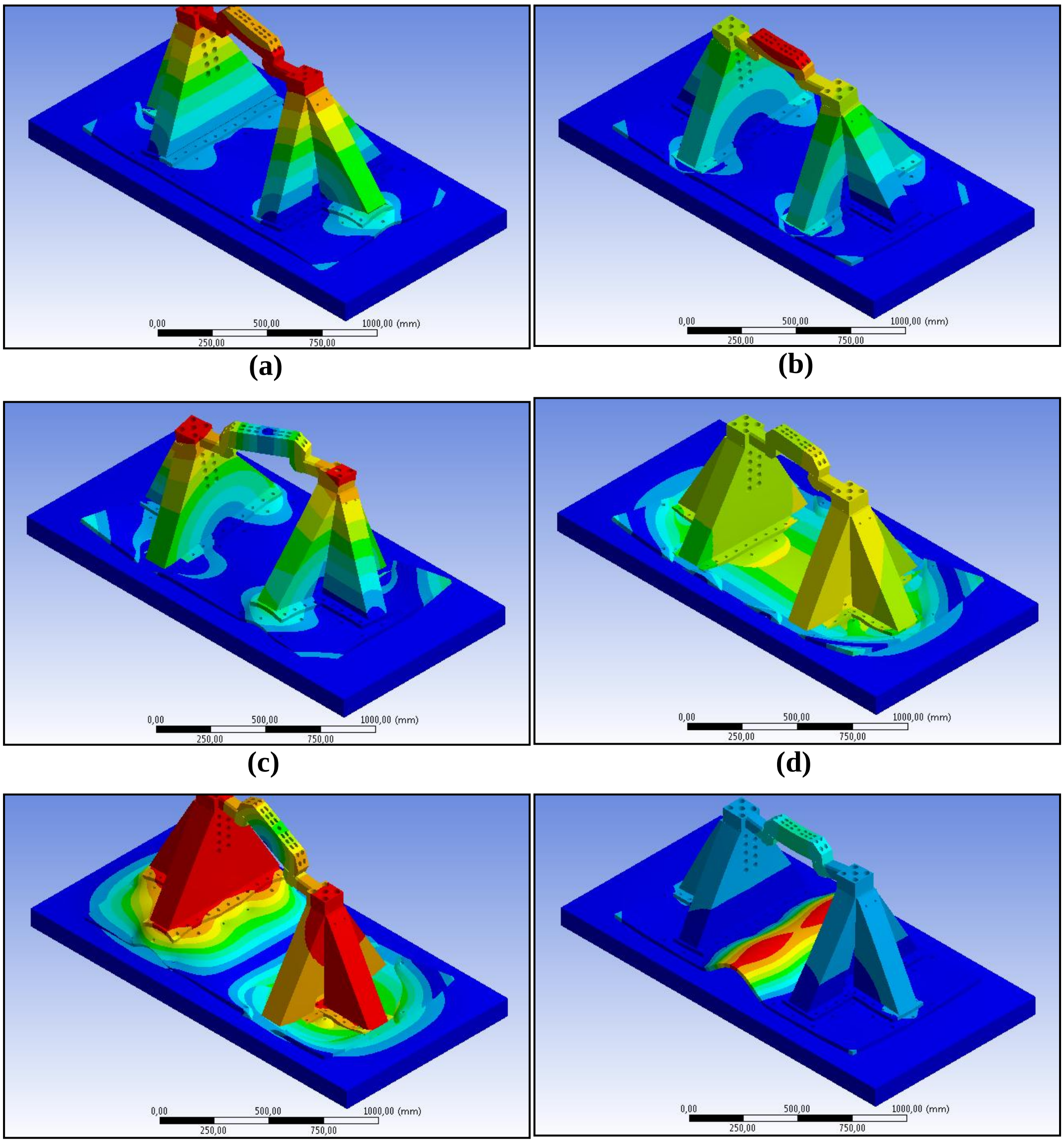

(a) (b)

(c) (d)

(e) (f)

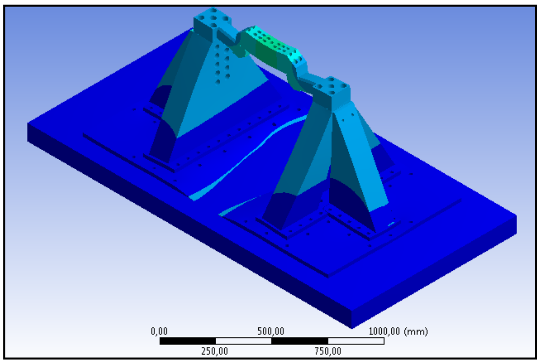

(g)

Figure 64. The mode shapes corresponding to the finite element model of the test set-up with 3-D model of the ground – third iteration: **(a)** 1st mode shape at 200.71 Hz; **(b)** 2nd mode shape at 230.04 Hz; **(c)** 3rd mode shape at 270.94 Hz; **(d)** 4th mode shape at 276.55 Hz; **(e)** 5th mode shape at 317.58 Hz; **(f)** 10th mode shape at 420.42 Hz; **(g)** 11th mode shape at 460.4 Hz

When the modes of the third iteration of the finite element model of the test set-up with the concrete block are compared with the experimental modes, it can be seen that the 1st modal frequency of the third iteration of the finite element model of the test set-up with the concrete block, which is 200.71 Hz, has become higher than the 1st experimental modal frequency, which is 162.8 Hz. However, the 1st mode shapes are achieved to resemble to each other this time.

In the fourth iteration, therefore, in order to decrease the 1st modal frequency the thickness of the concrete block is decided to be decreased to 80 mm while the stiffness value of the elastic foundation with which the bottom surface of the concrete block is supported remains as 0.1 N/mm^3 and the common stiffness value of the elastic foundations with which the side surfaces of the concrete block are supported remains as infinity, i.e. the side surfaces of the concrete block are fixed. Young's modulus of the concrete block also remains as 3x10^{10} Pa.

Since the thickness of the concrete block has been changed, the finite element model of the test set-up with 3-D model of the ground has also changed as shown in Fig.65.

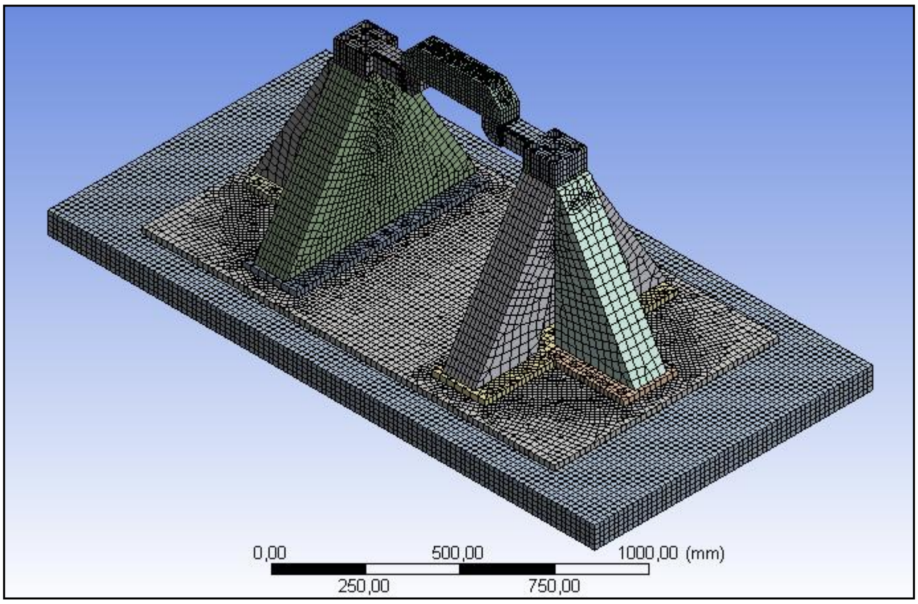

Figure 65. Finite Element Model of the Test Set-up with the Concrete Block Representing the Compliant Ground (Thickness of the concrete block is 80 mm.) (MultiZone Mesh; Relevance: 20; Relevance Center: Medium; Element Size of the Concrete Block: 18 mm; Number of Nodes: 460504; Number of Elements: 187583; Aspect Ratio (average): 2.56)

The results of the modal analysis which cover 12 modes in the frequency range of 30 Hz – 500 Hz are as such: The 6th, 7th, 8th and 9th modes of this model in the given frequency range belong to the deformation of only the corners of the base plate with the corresponding frequencies in the range of 343.7 Hz – 354.37 Hz. The remaining modes belong to the structural deformation of the whole test set-up and the 3-D model of the ground, as shown in Fig.66.

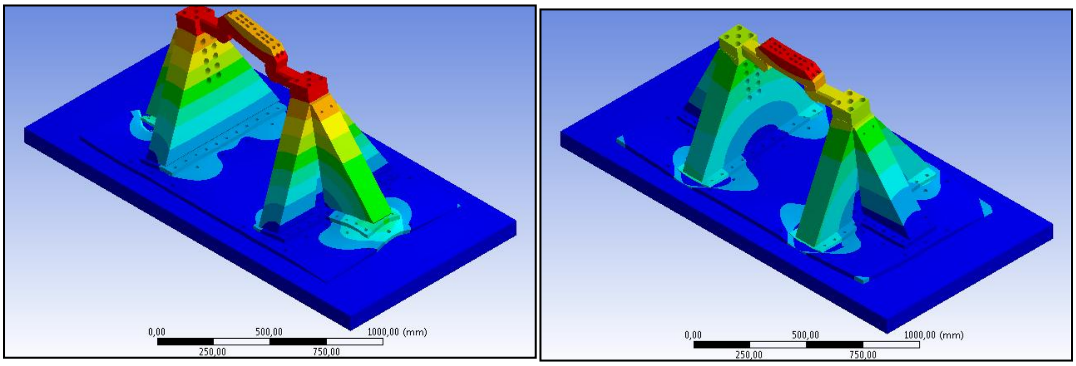

(a) **(b)**

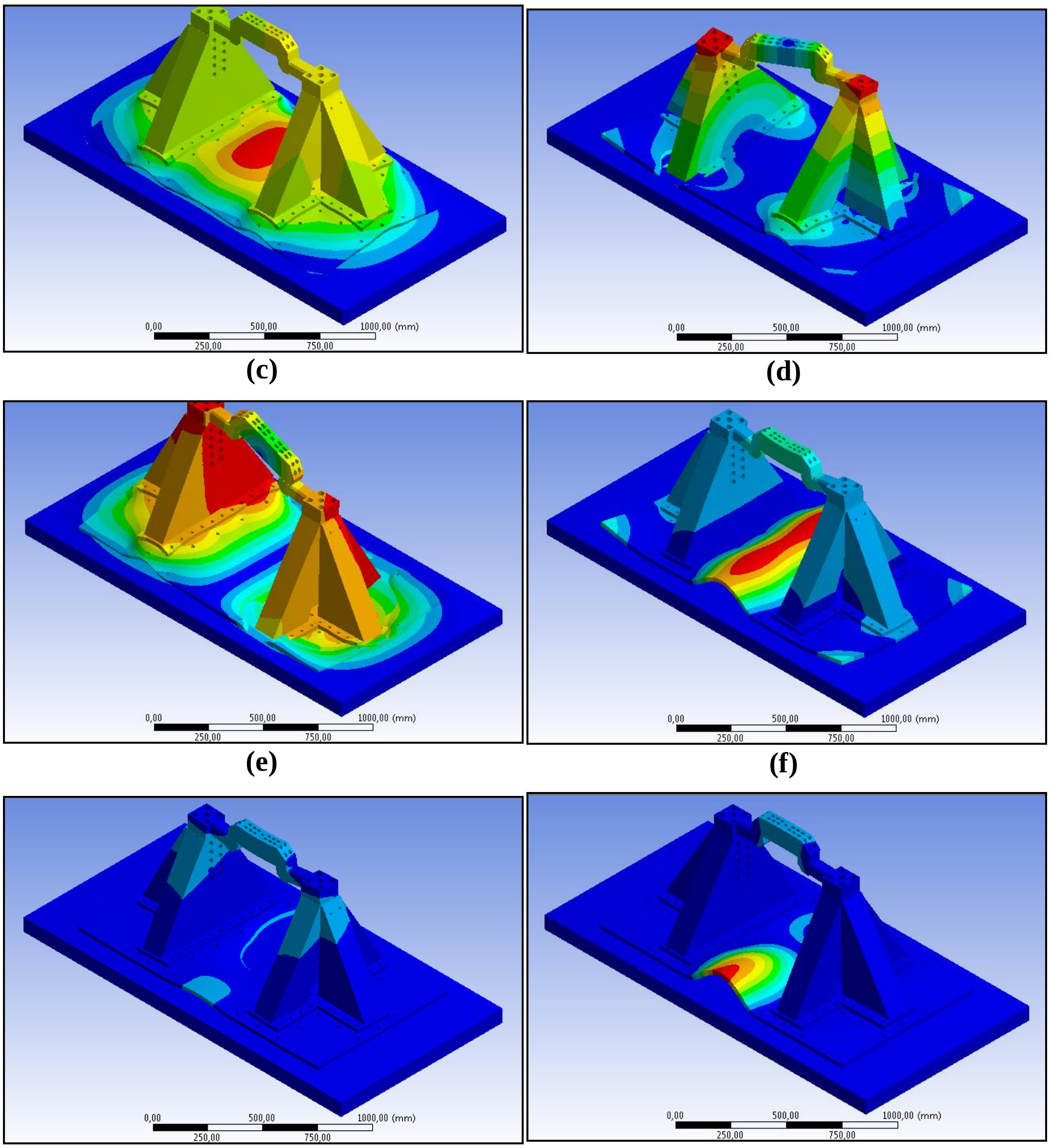

(c) (d)

(e) (f)

(g) (h)

Figure 66. The mode shapes corresponding to the finite element model of the test set-up with 3-D model of the ground – fourth iteration: **(a)** 1st mode shape at 192.08 Hz; **(b)** 2nd mode shape at 223.91 Hz; **(c)** 3rd mode shape at 239.88 Hz; **(d)** 4th mode shape at 264.39 Hz; **(e)** 5th mode shape at 274.72 Hz; **(f)** 10th mode shape at 408.73 Hz; **(g)** 11th mode shape at 458.44 Hz; **(h)** 12th mode shape at 458.87 Hz

When the modes of the fourth iteration of the finite element model of the test set-up with the concrete block are compared with the experimental modes, it can be seen that the 1st modal frequency of the fourth iteration of the finite element model of the test set-up with the concrete block, which is 192.08 Hz, is still higher than the 1st experimental modal frequency, which is 162.8 Hz.

In the fifth iteration, therefore, in order to further decrease the 1st modal frequency the thickness of the concrete block is decided to be decreased to 60 mm while the stiffness value of the elastic foundation with which the bottom surface of the concrete block is supported remains as 0.1 N/mm^3 and the common stiffness value of the elastic foundations with which the side surfaces of the concrete block are supported remains as infinity, i.e. the side surfaces of the concrete block are fixed. Young's modulus of the concrete block also remains as $3x10^{10}$ Pa.

Since the thickness of the concrete block has been changed, the finite element model of the test set-up with 3-D model of the ground has also changed as shown in Fig.67.

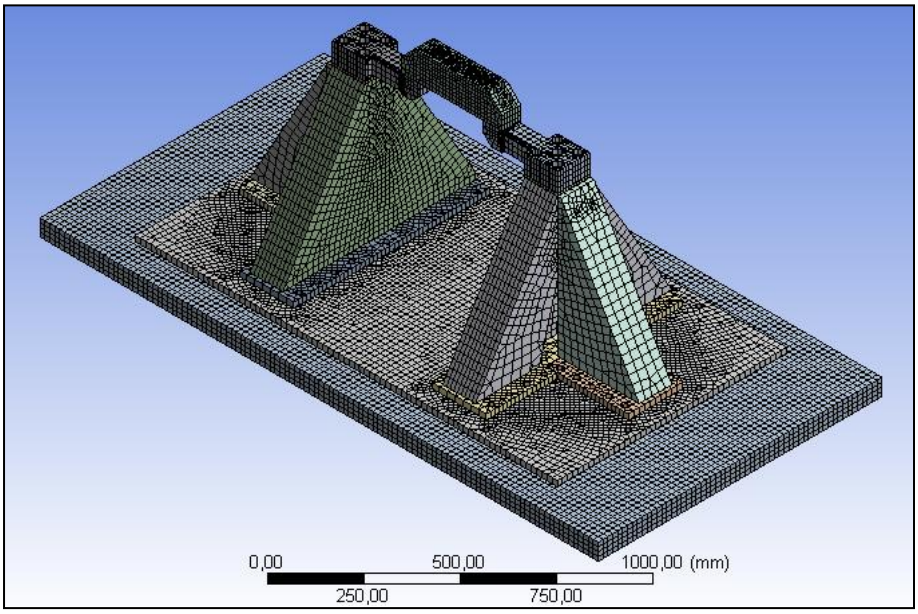

Figure 67. Finite Element Model of the Test Set-up with the Concrete Block Representing the Compliant Ground (Thickness of the concrete block is 60 mm.) (MultiZone Mesh; Relevance: 20; Relevance Center: Medium; Element Size of the Concrete Block: 18 mm; Number of Nodes: 433124; Number of Elements: 180731; Aspect Ratio (average): 2.62)

The results of the modal analysis which cover 12 modes in the frequency range of 30 Hz – 500 Hz are as such: The 6th, 7th, 8th and 9th modes of this model in the given frequency range belong to the deformation of only the corners of the base plate with the corresponding frequencies in the range of 339.07 Hz – 350.31 Hz. The remaining modes belong to the structural deformation of the whole test set-up and the 3-D model of the ground, as shown in Fig.68.

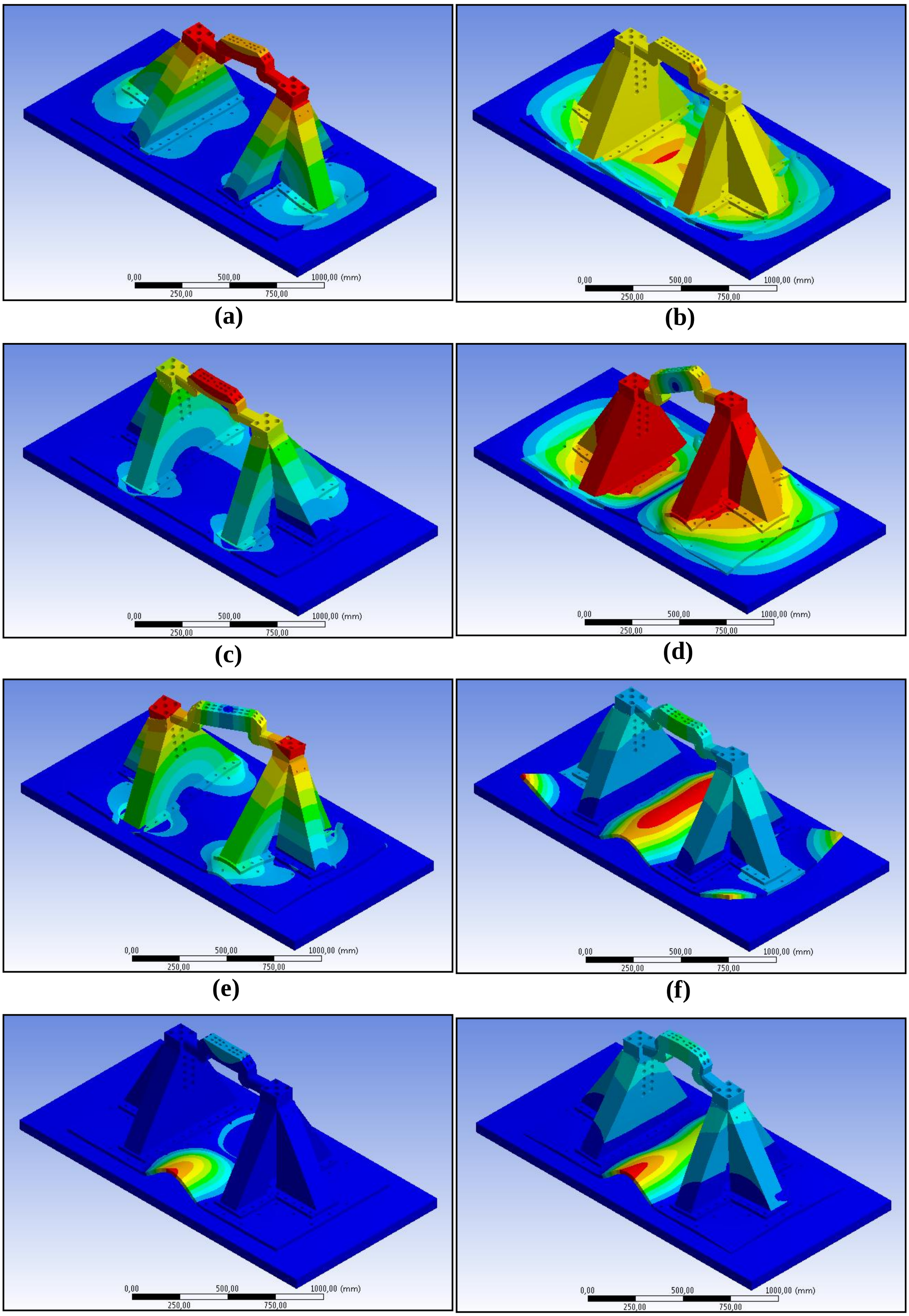

(a) (b)

(c) (d)

(e) (f)

(g) (h)

Figure 68. The mode shapes corresponding to the finite element model of the test set-up with 3-D model of the ground – fifth iteration: **(a)** 1st mode shape at 175.05 Hz; **(b)** 2nd mode shape at 203.03 Hz; **(c)** 3rd mode shape at 211.28 Hz; **(d)** 4th mode shape at 229.69 Hz; **(e)** 5th mode shape at 250.92 Hz; **(f)** 10th mode shape at 390.73 Hz; **(g)** 11th mode shape at 452.87 Hz; **(h)** 12th mode shape at 456.5 Hz

When the modes of the fifth iteration of the finite element model of the test set-up with the concrete block are compared with the experimental modes, it can be seen that the 1st modal frequency of the fifth iteration of the finite element model of the test set-up with the concrete block, which is 175.05 Hz, is still higher than the 1st experimental modal frequency, which is 162.8 Hz.

In the sixth iteration, therefore, in order to further decrease the 1st modal frequency Young's modulus of the concrete block is decided to be decreased to 1.5×10^{10} Pa (included within concrete's Young's modulus range of 1.4×10^{10} Pa – 4.1×10^{10} Pa [30]) while the stiffness value of the elastic foundation with which the bottom surface of the concrete block is supported remains as 0.1 N/mm^3 and the common stiffness value of the elastic foundations with which the side surfaces of the concrete block are supported remains as infinity, i.e. the side surfaces of the concrete block are fixed. The thickness of the concrete block also remains as 60 mm.

The results of the modal analysis which cover 12 modes in the frequency range of 30 Hz – 500 Hz are as such: The 6th, 7th, 8th and 9th modes of this model in the given frequency range belong to the deformation of only the corners of the base plate with the corresponding frequencies in the range of 319.98 Hz – 332.84 Hz. The remaining modes belong to the structural deformation of the whole test set-up and the 3-D model of the ground, as shown in Fig.69.

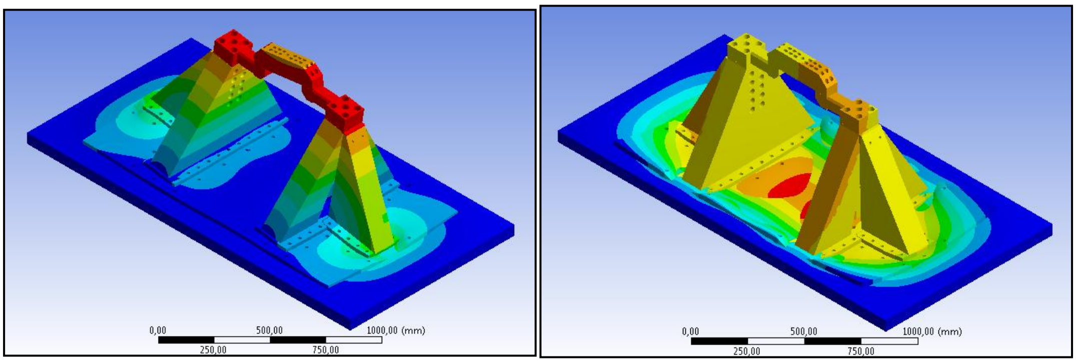

(a) **(b)**

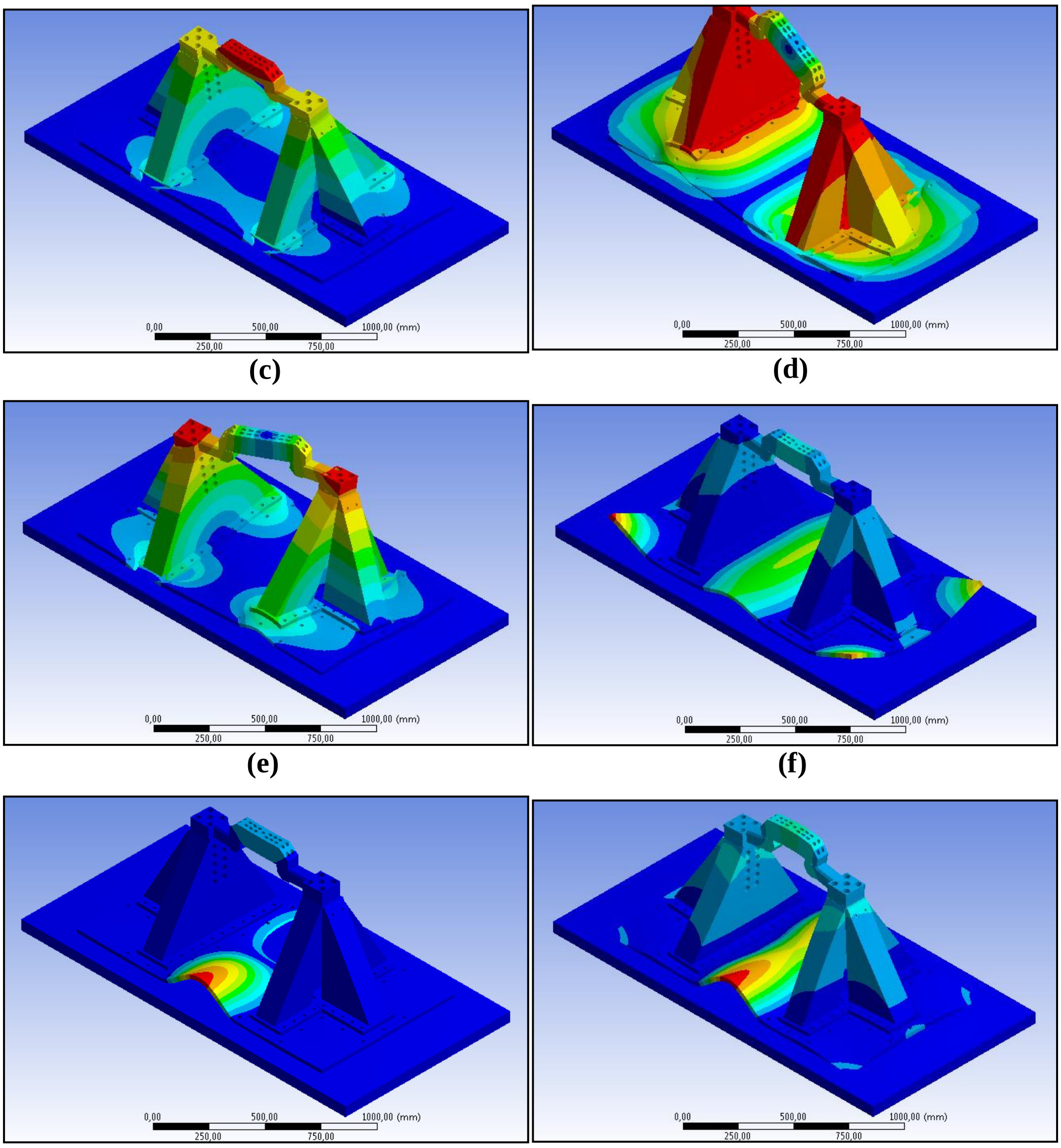

(c) **(d)**

(e) **(f)**

(g) **(h)**

Figure 69. The mode shapes corresponding to the finite element model of the test set-up with 3-D model of the ground – sixth iteration: **(a)** 1st mode shape at 152.11 Hz; **(b)** 2nd mode shape at 171.09 Hz; **(c)** 3rd mode shape at 187.94 Hz; **(d)** 4th mode shape at 193.05 Hz; **(e)** 5th mode shape at 226.44 Hz; **(f)** 10th mode shape at 363.2 Hz; **(g)** 11th mode shape at 430.08 Hz; **(h)** 12th mode shape at 444.86 Hz

When the modes of the sixth iteration of the finite element model of the test set-up with the concrete block are compared with the experimental modes, it can be seen that the 1st modal frequency of the sixth iteration of the finite element model of the test set-up with the concrete block, which is 152.11 Hz, has become lower than the 1st experimental modal frequency, which is 162.8 Hz.

In the seventh iteration, therefore, in order to increase the 1st modal frequency the stiffness value of the elastic foundation with which the bottom surface of the concrete block is supported is increased to 0.3 N/mm^3 while the thickness and Young’s modulus of the concrete block remains as 60mm and 1.5x10^{10} Pa, respectively, and also the common stiffness value of the elastic foundations with which the side surfaces of the concrete block are supported remains as infinity, i.e. the side surfaces of the concrete block are fixed.

The results of the modal analysis which cover 12 modes in the frequency range of 30 Hz – 500 Hz are as such: The 6th, 7th, 8th and 9th modes of this model in the given frequency range belong to the deformation of only the corners of the base plate with the corresponding frequencies in the range of 323.11 Hz – 333.66 Hz. The remaining modes belong to the structural deformation of the whole test set-up and the 3-D model of the ground, as shown in Fig.70.

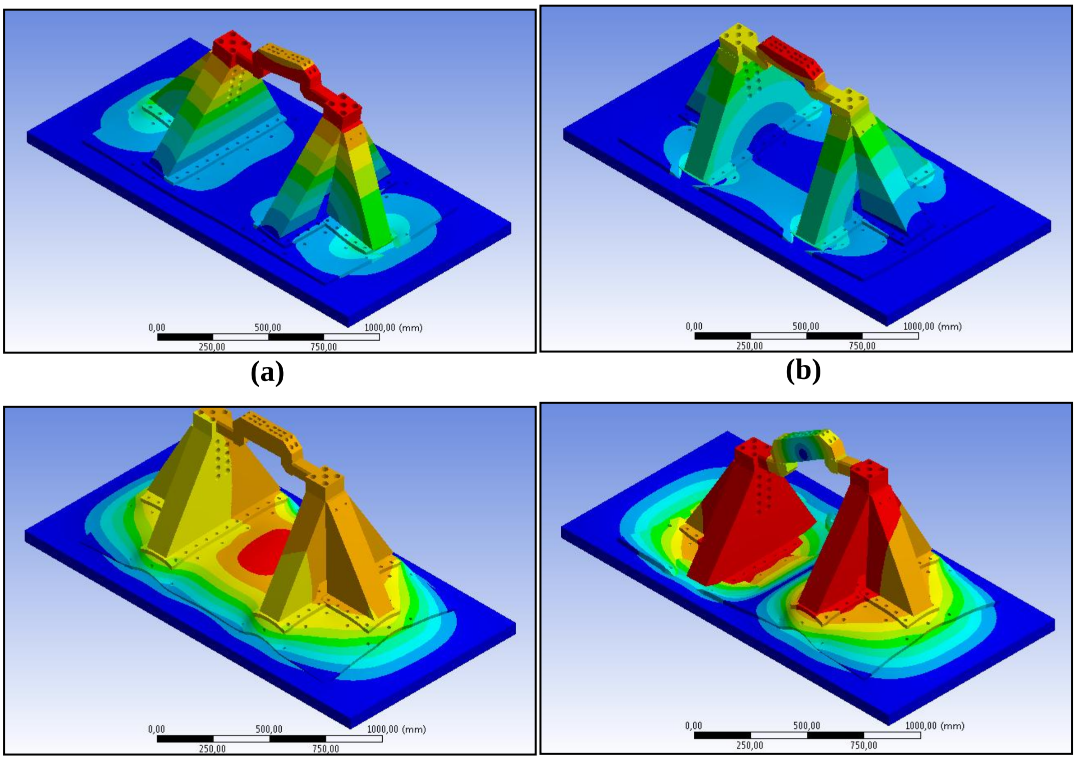

(a) **(b)**

(c) **(d)**

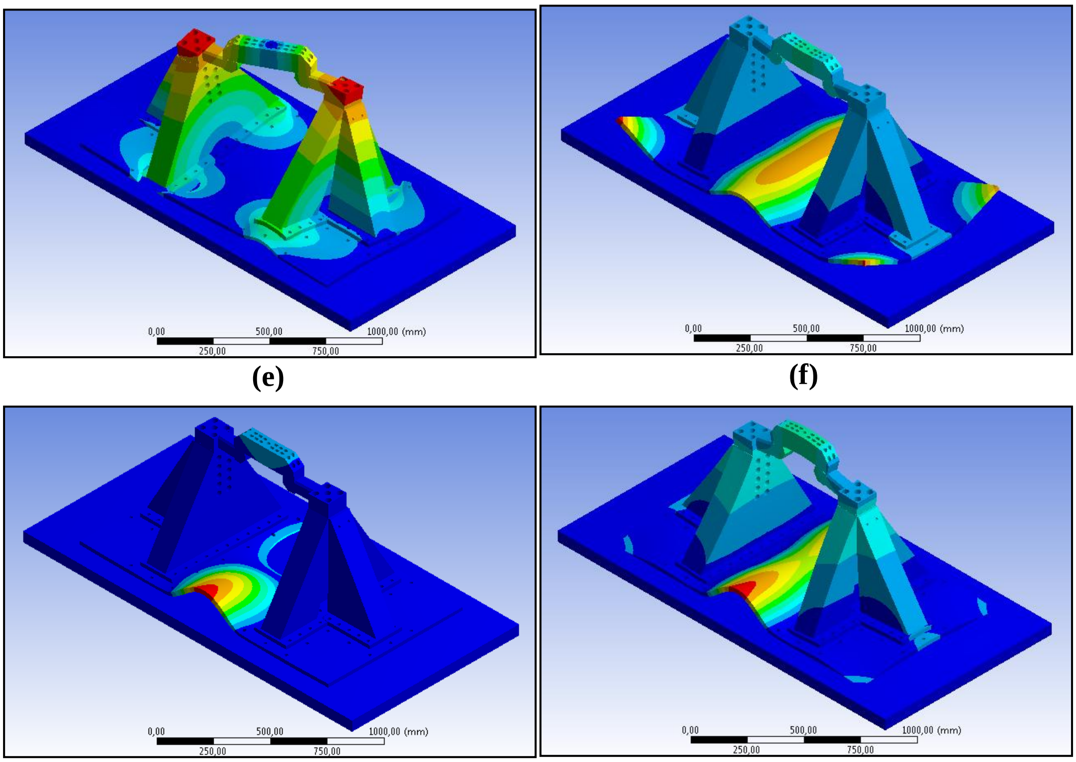

(e) (f)

(g) (h)

Figure 70. The mode shapes corresponding to the finite element model of the test set-up with 3-D model of the ground – seventh iteration: **(a)** 1st mode shape at 157.34 Hz; **(b)** 2nd mode shape at 190.38 Hz; **(c)** 3rd mode shape at 196.34 Hz; **(d)** 4th mode shape at 212.84 Hz; **(e)** 5th mode shape at 228.83 Hz; **(f)** 10th mode shape at 371.62 Hz; **(g)** 11th mode shape at 432.52 Hz; **(h)** 12th mode shape at 446.5 Hz

When the modes of the seventh iteration of the finite element model of the test set-up with the concrete block are compared with the experimental modes, it can be seen that the 1st modal frequency of the seventh iteration of the finite element model of the test set-up with the concrete block, which is 157.34 Hz, is still lower than the 1st experimental modal frequency, which is 162.8 Hz.

In the eighth iteration, therefore, in order to further increase the 1st modal frequency Young's modulus of the concrete block is decided to be increased to 1.8×10^{10} Pa (included within concrete's Young's modulus range of 1.4×10^{10} Pa – 4.1×10^{10} Pa [30]) while the stiffness value of the elastic foundation with which the bottom surface of the concrete block is supported remains as 0.3 N/mm^3 and the common stiffness value of the elastic foundations with which the side surfaces of the concrete block are supported remains as infinity, i.e. the side surfaces of the concrete block are fixed. The thickness of the concrete block also remains as 60 mm.

The results of the modal analysis which cover 13 modes in the frequency range of 30 Hz – 550 Hz are as such: The 6th, 7th, 8th and 9th modes of this model in the given frequency range belong to the deformation of only the corners of the base plate with the corresponding frequencies in the range of 327.97 Hz – 338.54 Hz. The remaining modes belong to the structural deformation of the whole test set-up and the 3-D model of the ground, as shown in Fig.71.

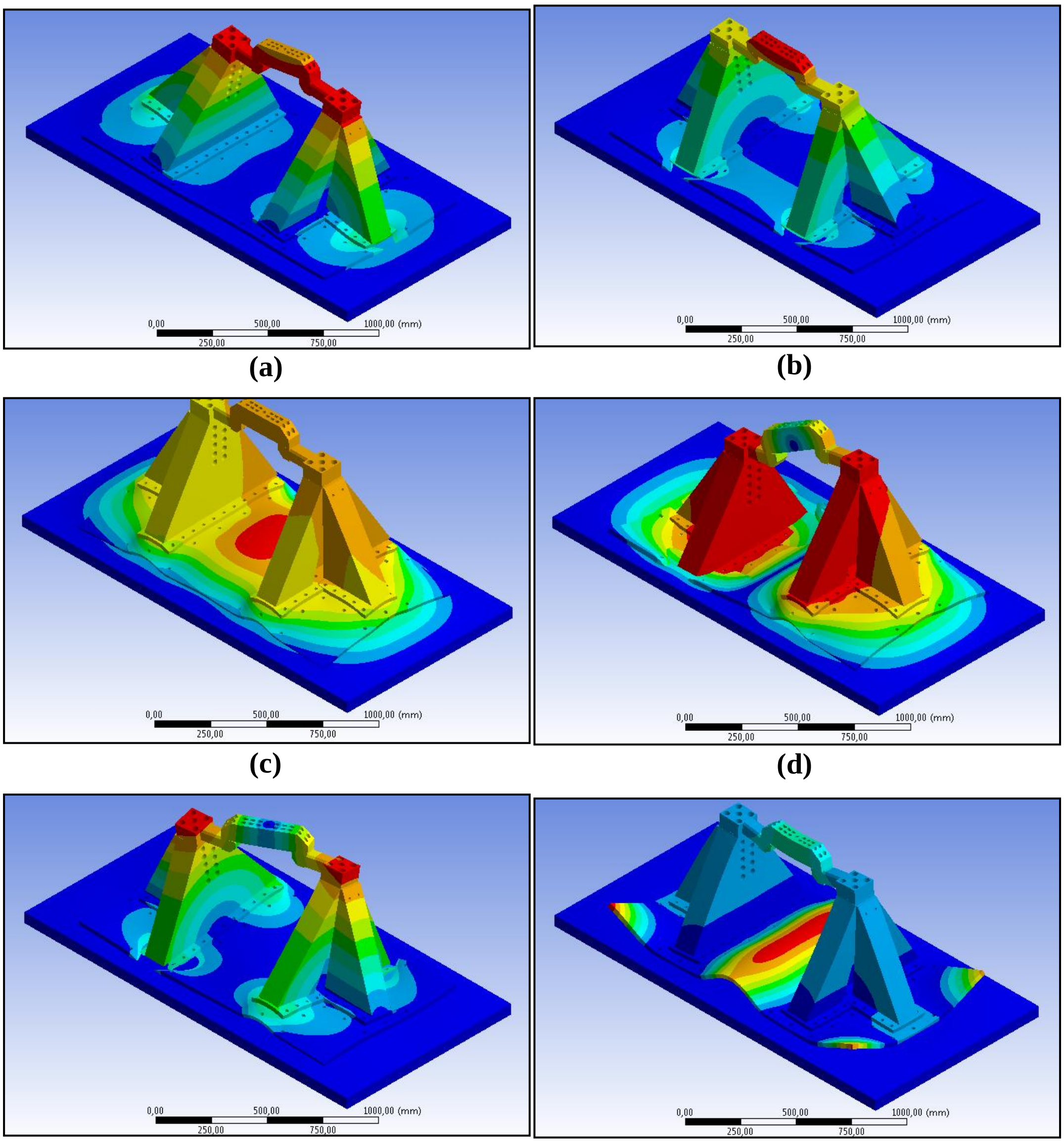

(a) (b) (c) (d) (e) (f)

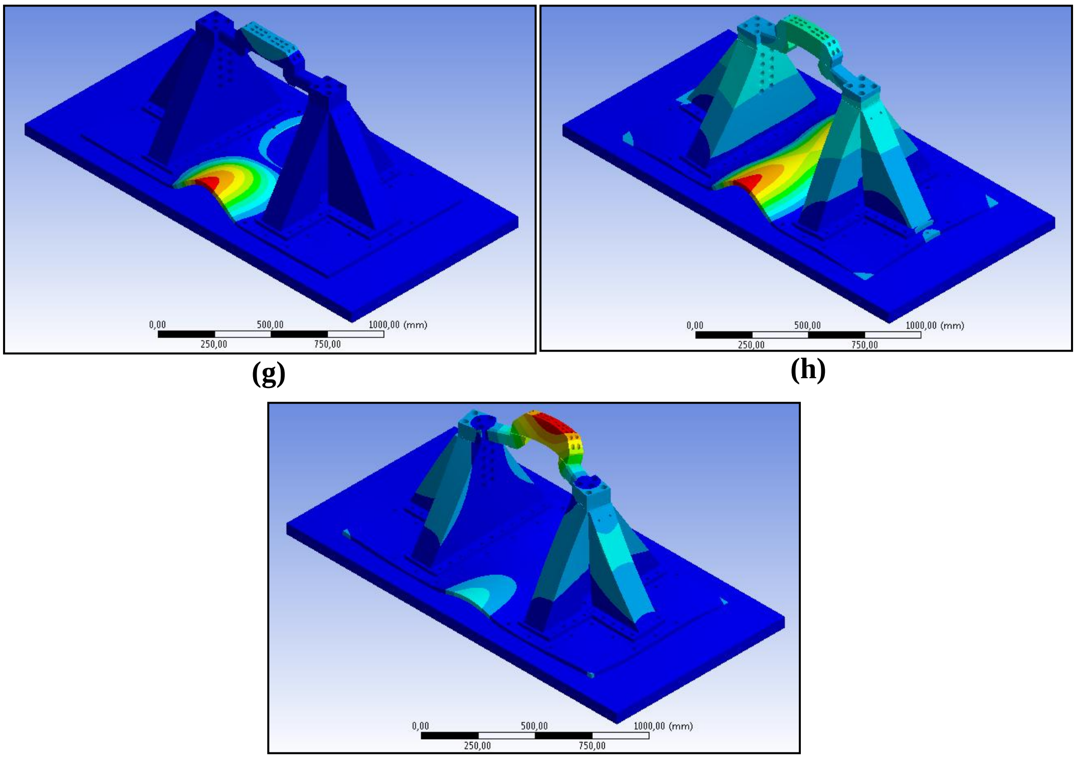

(g) **(h)**

(i)

Figure 71. The mode shapes corresponding to the finite element model of the test set-up with 3-D model of the ground – eighth iteration: **(a)** 1st mode shape at 162.62 Hz; **(b)** 2nd mode shape at 196.43 Hz; **(c)** 3rd mode shape at 203.02 Hz; **(d)** 4th mode shape at 220.73 Hz; **(e)** 5th mode shape at 235.18 Hz; **(f)** 10th mode shape at 378.01 Hz; **(g)** 11th mode shape at 438.87 Hz; **(h)** 12th mode shape at 449.54 Hz; **(i)** 13th mode shape at 527.91 Hz

When the modes of the eighth iteration of the finite element model of the test set-up with the concrete block are compared with the experimental modes, it can be seen that the 1st modal frequency of the eighth iteration of the finite element model of the test set-up with the concrete block, which is 162.62 Hz, is almost the same as the 1st experimental modal frequency, which is 162.8 Hz. The 1st mode shapes already resemble to each other. Therefore, further iterations are not required to be performed.

Besides the 1st mode, the 3rd experimental mode shape is similar to the 10th and 12th mode shapes of the eighth iteration of the finite element model of the test set-up with the concrete block. However, the 3rd experimental modal frequency, which is 393.18 Hz, is in between the 10th and 12th modal frequencies of the eighth iteration of the finite element model of the test set-up with the concrete block, which are 378.01 Hz and 449.54 Hz, respectively. This is most probably due to the fact that the modal tests are not able to distinguish these two modes. In addition, the 7^{th} experimental mode shape is similar to the 13^{th} mode shape of the eighth iteration of the finite element model of the test set-up with the concrete block. The 7^{th} experimental modal frequency, which is 530.34 Hz, is also very close to the 13^{th} modal frequency of the eighth iteration of the finite element model of the test set-up with the concrete block, which is 527.91 Hz.

The problems are that the 2^{nd}, 3^{rd}, 4^{th} and 5^{th} modes of the final iteration of the finite element model of the test set-up with the concrete block, where there is a considerable deformation of the upper part of the test set-up, do not appear within the experimental modes. This is most probably due to the fact that these modes are not able to be excited during the modal tests. In addition, the 2^{nd}, 4^{th}, 5^{th} and 6^{th} experimental modes do not appear within the modes of the final iteration of the finite element model of the test set-up with the concrete block. This is most probably due to the fact these modes are identified considering the highly damped peaks of the driving-point FRF’s obtained as a result of the modal tests, which are likely to be misleading.

As the final remarks, when the modal analysis results of the final iteration of the finite element model of the test set-up with the concrete block are investigated, it is clearly seen that the frequencies at which the structural modes of the whole test set-up occur (disregarding the local modes of the base plate) are quite lower than the ones for the previous finite element model of the test set-up with the base plate, which takes the bolted-joints between the parts into consideration. It must also be stated that although there are a few additional modes (3^{rd} and 4^{th} modes in Fig.71), the mode order has not yet changed. Since the latest model best simulates the real world conditions, it can easily be said that the first structural modal frequency of the *whole* test set-up has eventually decreased from 286 Hz to 163 Hz, which corresponds to an approximately 43% decrease. In conclusion, it is obvious that the first natural frequency of the test set-up, which is 163 Hz, is in fact much lower than the initially estimated one of 520 Hz, which corresponds to an approximately 69% total decrease, and this fact reveals the significance of defining the boundary conditions of the structures and the contact relations between the parts of the structures properly.

It is also quite important to point out that since the excitation induced on the specimens by the vibration exciter is expected to be directly transmitted to the mid-point of the upper block in the vertical direction, the 1st mode of the test set-up is hardly excited during the VEM characterization tests. Instead, the 3rd mode with the frequency of 393 Hz is highly possible to be excited. Therefore, the upper frequency limit of the VEM characterization tests can be specified as approximately 200 Hz, so that the accuracy of the measured data is ensured.

CHAPTER 4

SELECTION OF THE SENSORS, ACTUATOR AND DATA ACQUISITION HARDWARE

In this part of the thesis, the studies carried out to decide on the electrical and electronic test equipment to be employed in the VEM test set-up are presented. The objective is to select the vibration transducers, vibration exciter (i.e., electrodynamic shaker), and data acquisition cards considering their operating principles and technical specifications.

The most important factors to consider while selecting the vibration transducers, the data acquisition cards and the vibration exciter is the possible levels of dynamic quantities such as displacements, accelerations and forces that will be observed during the vibration tests, and the frequency and temperature ranges in which the vibration tests are intended to be carried out. The frequency limit up to which the data obtained during VEM characterization tests is accurate is determined to be the first structural natural frequency of the designed test set-up, which is approximately 500 Hz according to the initial finite element model as mentioned beforehand. The lower frequency limit is generally set by the low frequency response of the amplifiers of the vibration transducers and the vibration exciter [1]. The temperature range of interest in which the VEM characterization tests are carried out is specified to be -50°C to +70°C. The possible levels of displacement, acceleration and force signals that are expected to be observed in VEM characterization tests are significant to be estimated beforehand by simulating the actual testing conditions in order to select the electrical and electronic test equipment considering their measurement and signal generation capabilities. When the VEM’s are in the glassy region, they exhibit the smallest response levels especially at low frequencies. This fact is significant to be considered since low-level signals are highly susceptible to electrical noise, affecting the measurement accuracy adversely [1, 19]. On the other hand, when the VEM’s are in the rubbery region, they exhibit the largest response levels especially at frequencies at which the viscoelastic specimens and the steel rigid block attached to them get into resonance with the fixture behaving as a fixed rigid body. This fact is also significant to be considered due to maximum signal levels that the test equipment can handle. In addition, the maximum strain levels that the specimens are expected to experience are to be estimated since up to 1 % dynamic strain amplitude VEM’s exhibit linear viscoelastic behavior [11].

In order to estimate the possible levels of displacements, accelerations, forces and strains, the two-DOF mathematical model of the test set-up shown in Fig.26 is utilized for both tensile and double-shear specimen configurations [19]. The fixture is assigned an effective mass value of 80 kg and first structural natural frequency value of 500 Hz, which are close to the corresponding values of the initial model of the test set-up. For tensile specimen configuration the effective vibrating mass attached to the specimen is taken as 1.2 kg, and the length and the edge length of the square cross-section of the specimen is assigned the values of 6 cm and 3 cm, respectively, while for double-shear specimen configuration the effective vibrating mass attached to the specimens is taken as 0.7 kg, and the thickness and the edge length of the square cross-section of the specimens are assigned the values of 3 mm and 5 cm, respectively, which are acceptable and close to the actual values. For the purpose of this simulation two codes are written in MATLAB [see Appendix A.2] where the harmonic force amplitude is taken as 15 N, and for tensile specimen the VEM named LD-400 by Lord Corporation [2] and for shear specimen the VEM named 3M-467 by 3M Company [2] are used. The results are presented in Tables 11, 12, 13 and 14 for tensile and double-shear specimen configurations at several frequencies at the minimum and maximum temperatures to evaluate the responses of the specimens in the glassy and rubbery regions, respectively.

Table 11. Vibration response and strain determination of tensile specimen configuration for harmonic force amplitude of 15 N in glassy region

Frequency [Hz]	Temperature: -50°C				
	Harmonic amplitude of normal strain (%)	Harmonic amplitude of rigid block's displacement [m]	Harmonic amplitude of fixture's displacement [m]	Harmonic amplitude of rigid block's acceleration [m/s^2]	Harmonic amplitude of fixture's acceleration [m/s^2]
10	8,05E-05	6,73E-08	1,90E-08	2,66E-04	7,50E-05
20	8,05E-05	6,73E-08	1,90E-08	1,10E-03	3,01E-04
30	8,05E-05	6,74E-08	1,91E-08	2,40E-03	6,78E-04
335	8,29E-05	8,53E-08	3,55E-08	3,78E-01	1,57E-01

Table 12. Vibration response and strain determination of tensile specimen configuration for harmonic force amplitude of 15 N in rubbery region

Frequency [Hz]	Temperature: 70°C				
	Harmonic amplitude of normal strain (%)	Harmonic amplitude of rigid block's displacement [m]	Harmonic amplitude of fixture's displacement [m]	Harmonic amplitude of rigid block's acceleration [m/s^2]	Harmonic amplitude of fixture's acceleration [m/s^2]
10	4,90E-03	2,95E-06	1,90E-08	1,16E-02	7,51E-05
20	4,90E-03	2,94E-06	1,91E-08	4,65E-02	3,02E-04
30	4,90E-03	2,95E-06	1,92E-08	1,05E-01	6,83E-04
335	9,57E-02	5,81E-05	7,08E-07	2,57E+02	3,14E+00

Table 13. Vibration response and strain determination of double-shear specimen configuration for harmonic force amplitude of 15 N in glassy region

Frequency [Hz]	Temperature: -50°C				
	Harmonic amplitude of shear strain (%)	Harmonic amplitude of rigid block's displacement [m]	Harmonic amplitude of fixture's displacement [m]	Harmonic amplitude of rigid block's acceleration [m/s^2]	Harmonic amplitude of fixture's acceleration [m/s^2]
10	2,10E-03	8,20E-08	1,90E-08	3,24E-04	7,50E-05
20	2,00E-03	7,88E-08	1,90E-08	1,20E-03	3,01E-04
30	1,90E-03	7,75E-08	1,91E-08	2,80E-03	6,78E-04
115	1,90E-03	7,57E-08	2,01E-08	3,95E-02	1,05E-02

Table 14. Vibration response and strain determination of double-shear specimen configuration for harmonic force amplitude of 15 N in rubbery region

Frequency [Hz]	Temperature: 70°C				
	Harmonic amplitude of shear strain (%)	Harmonic amplitude of rigid block's displacement [m]	Harmonic amplitude of fixture's displacement [m]	Harmonic amplitude of rigid block's acceleration [m/s^2]	Harmonic amplitude of fixture's acceleration [m/s^2]
10	3,90E+00	1,17E-04	1,94E-08	4,62E-01	7,65E-05
20	3,36E+00	1,01E-04	2,03E-08	1,59E+00	3,20E-04
30	3,14E+00	9,43E-05	2,16E-08	3,35E+00	7,68E-04
115	2,35E+00	7,05E-05	2,80E-08	3,68E+01	1,46E-02

When the results are investigated, first of all, it is clearly seen that it is a wise choice to use accelerometers instead of displacement transducers since the estimated levels of displacements that are expected to be measured during vibration tests are quite low, and therefore it would be difficult to amplify the signals sufficiently. Then, looking at the acceleration levels at low frequencies (10-30 Hz) when both the tensile and shear specimens are in glassy region, it is decided to use accelerometers with 1000 mV/g nominal sensitivity value (the highest sensitivity value commercial accelerometers currently have) in order to minimize the adverse effect of electrical noise and maximize the measurement accuracy by obtaining the largest possible levels of output voltage signals from the accelerometers [19]. The levels of output voltage signals from 1000 mV/g accelerometers corresponding to the acceleration levels given in Tables 11, 12, 13 and 14 are presented in Tables 15 and 16.

Table 15. Output voltage signal levels from 1000 mV/g accelerometers for the responses of tensile specimen configuration to harmonic force amplitude of 15 N in both glassy and rubbery regions

Frequency [Hz]	Temperature: -50°C		Temperature: 70°C	
	Output signal of the accelerometer at the rigid block [mV]	Output signal of the accelerometer at the fixture [mV]	Output signal of the accelerometer at the rigid block [mV]	Output signal of the accelerometer at the fixture [mV]
10	2,71E-02	7,65E-03	1,18E+00	7,66E-03
20	1,12E-01	3,07E-02	4,74E+00	3,08E-02
30	2,45E-01	6,91E-02	1,07E+01	6,96E-02
335	3,85E+01	1,60E+01	2,62E+04	3,20E+02

Table 16. Output voltage signal levels from 1000 mV/g accelerometers for the responses of double-shear specimen configuration to harmonic force amplitude of 15 N in both glassy and rubbery regions

Frequency [Hz]	Temperature: -50°C		Temperature: 70°C	
	Output signal of the accelerometer at the rigid block [mV]	Output signal of the accelerometer at the fixture [mV]	Output signal of the accelerometer at the rigid block [mV]	Output signal of the accelerometer at the fixture [mV]
10	3,30E-02	7,65E-03	4,71E+01	7,80E-03
20	1,22E-01	3,07E-02	1,62E+02	3,26E-02
30	2,85E-01	6,91E-02	3,41E+02	7,83E-02
115	4,03E+00	1,07E+00	3,75E+03	1,49E+00

Looking at the output voltage signal levels at low frequencies (10-30 Hz) when both the tensile and shear specimens are in glassy region, it is concluded that it would be better to use an analog input data acquisition card with 24-bits of analog-to-digital conversion resolution capability and ± 0.1 V range setting option in order to increase the measurement accuracy [19]. It is found out that 335 Hz is the frequency at which the representative tensile specimen in rubbery region and the steel rigid block attached to it gets into resonance with the fixture behaving as a fixed rigid body. When the results in Table 12 at this frequency are investigated, it is seen that the dynamic strain amplitude is smaller than 1 % as it has to be; however the level of maximum acceleration is quite large that the measurement capacity of selected accelerometers could be exceeded. Therefore, in rubbery region it would be better to excite tensile specimens with harmonic force amplitudes much less than 15 N. Similarly, it is found out that 115 Hz is the frequency at which the representative shear specimens in rubbery region and the steel rigid block attached to them gets into resonance with the fixture behaving as a fixed rigid body. When the results in Table 14 at this frequency are investigated, it is seen that this time the level of maximum acceleration is such that the capacity of selected accelerometers could be sufficient to measure; however the dynamic strain amplitude is slightly larger than 1 %. Therefore, in rubbery region it would also be better to excite shear specimens with harmonic force amplitudes less than 15 N.

Once the necessary technical information is acquired, the vibration transducers, data acquisition cards and the vibration exciter (i.e., electrodynamic shaker) are selected also considering the economical constraints.

4.1. Features of the Selected Vibration Transducers

4.1.1. Features of the Accelerometers

Four PCB Piezotronics, Inc. Model 352B ceramic shear ICP® accelerometers are selected [31]. The nominal sensitivity of these accelerometers is 1000 mV/g. The maximum acceleration level to be measured is specified as ± 5g pk. The allowable frequency range is given as 2 Hz to 10,000 Hz, while the allowable temperature range is given as -54°C to +93°C. Since IEPE accelerometers have integral electronics for signal amplification to minimize cable-induced noise, they require low-current excitation [1]. The selected type of accelerometers requires constant current excitation in the range of 2 mA to 20 mA. Finally, it must be noted that the excitation voltage is specified as 20 Vdc to 30 Vdc.

4.1.2. Features of the Force Sensor

One PCB Piezotronics, Inc. Model 208C02 ICP® force sensor is selected [32]. The sensitivity of this force sensor is 11.241 mV/N. The maximum force level to be measured is specified as ± 444.8 N pk. The allowable frequency range is given as

0.001 Hz to 36,000 Hz, while the allowable temperature range is given as -54°C to +121°C. The selected type of force sensor also requires constant current excitation in the range of 2 mA to 20 mA. Finally, it must be noted that the excitation voltage is specified as 20 Vdc to 30 Vdc.

4.2. Features of the Selected Vibration Exciter

Dongling Vibration Co., Ltd. Model ESD-045 permanent magnet modal shaker is selected as the vibration exciter [36]. The maximum sinusoidal force level to be generated is specified as 450 N, which is much larger than the harmonic force amplitude with which the specimens are planned to be excited. The maximum stroke is given as 25 mm (pk-pk) and the maximum acceleration is given as 100g. The allowable frequency range is specified as 2 Hz to 3000 Hz.

4.3. Features of the Selected Data Acquisition Cards

4.3.1. Features of the Analog Input Data Acquisition Cards

Two National Instruments Model NI 9234 4-channel analog input modules with USB connections are selected [33]. This type of analog input cards supplies an IEPE excitation current of 2 mA at each channel so that IEPE sensors can be connected. They have built-in anti-aliasing filters with an alias-free bandwidth of $0.45f_s$. The sampling frequency for this type of analog input cards is formulated as $f_s = \frac{f_m/256}{n}$ where n = 1, 2, …, 31, and f_m stands for the frequency of the internal master time-base and is equal to 13.1072 MHz. The analog-to-digital conversion resolution is 24-bits and the input range is specified as ± 5 V; however the gain setting is not available. Finally, it must be noted that the IEPE compliance voltage of the selected type of analog input cards is given as 19 V max, which is equal to the lower limit of the selected vibration transducers' excitation voltage; therefore the full measurement range of the selected vibration transducers can be utilized [34].

4.3.2. Features of the Analog Output Data Acquisition Card

One National Instruments Model NI 9263 4-channel analog voltage output module with USB connection is selected [35]. The digital-to-analog conversion resolution for this type of analog output card is 16-bits and the output voltage range is specified as ± 10 V.

CHAPTER 5

DEVELOPMENT OF THE TEST SOFTWARE

In this part of the thesis, the studies carried out to develop the test software are presented. Firstly, the general theory of data acquisition and signal processing is briefly explained. Then, the development of the software dedicated to the VEM characterization tests in LabVIEW programming environment is explained in detail together with the FRF estimation procedure. The developed test software in LabVIEW performs two main functions, which are generation of signals to drive the electro-dynamic shaker, and measurement and processing of the signals received from the vibration transducers. Additional functions are also integrated to the test software such as measuring the temperature in the vicinity of the specimen during the tests and saving the resultant data at the end of the tests.

5.1. Theory and Application of Data Acquisition and Signal Processing

The purpose of a data acquisition system is to measure a physical phenomenon and transmit into computer for analysis and presentation. It is composed of the following elements: (1) Transducer; (2) Signal; (3) Signal conditioning; (4) Data acquisition device; (5) Driver level and application level software [37].

Transducers aim at converting a mechanical quantity of interest into a measurable electrical signal, usually in a voltage form. As it is stated in the introduction part, the transducers used in this thesis work are the force sensor, accelerometers and thermocouples.

There are two types of signals, which are digital signals and analog signals. Digital signals contain two types of information, which are state that is either on or off and rate that tells how the digital signal changes state with respect to time. Analog signals, on the other hand, contain three types of information, which are voltage level of the signal such as 3.75 Volts, shape of the signal such as sine-wave that allows further analysis with the peak values, zero-crossings, slopes and areas underneath, and frequency content of the signal in an indirect manner since the signal in the time domain requires Fourier transformation beforehand [37]. In this thesis work, analog signals are handled.

One main purpose of signal conditioning is to convert the low level signals at high impedance from transducers into signals at low impedance that are almost immune to electro-magnetic noise contamination caused mostly by cabling. If an external amplifier were to be used, it would best be placed as close to the transducer as possible in order to avoid electromagnetic noise pick-up as much as possible [1, 37]. However, as stated in the selection of the sensors, actuator and data acquisition hardware part, the transducers used in this thesis work have built-in amplifiers activated with a constant current supply of 2 mA. Another main purpose of signal conditioning is to pass the signals received from the transducers through special low-pass filters, namely “anti-aliasing filters”, before sampling in order to discard the data with frequency content above half the sampling frequency. Sampling of the measured data at discrete points in time causes the spectrum of the data to repeat periodically in the frequency domain such that the period is equal to the sampling frequency. For received signals with frequency content above half the sampling frequency, the corresponding spectral components are projected onto the ones at frequencies below half the sampling frequency due to the periodic repetition of the spectrum in the frequency domain, which is known as aliasing, and this phenomenon results in incorrect spectrum, as shown in Fig.72.

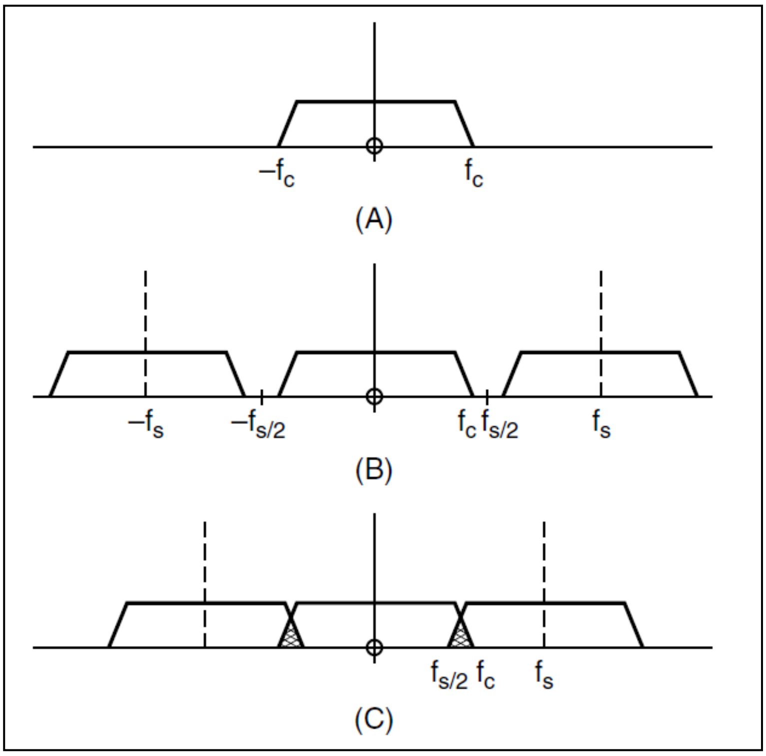

Figure 72. Representation of aliasing **(a)** Spectrum of a continuous band-limited signal with a maximum frequency (also known as cut-off frequency), f_c; **(b)** Spectrum of the sampled signal within a finite length of time with a sampling frequency, $f_s > 2f_c$; **(c)** Spectrum of the sampled signal with a sampling frequency, $f_s < 2f_c$, where the shaded areas display the aliased components [1]

Therefore, in order to obtain correct spectrum the anti-aliasing filtering operation is essential before sampling the measurement data [1, 37]. As stated in the selection of the sensors, actuator and data acquisition hardware part, the analog input data acquisition cards used in the thesis work have built-in anti-aliasing filters, therefore external filtering is not required.

A data acquisition device/card is an agent between the signals coming from the transducers and a software environment, or between the waveforms generated in a software environment and the actuators. As it is stated in the selection of the sensors, actuator and data acquisition hardware part, as an analog input data acquisition card 4-channel USB-based NI 9234 analog input module with 24-bits analog-to-digital conversion resolution and ± 5 Volts range, and as an analog output data acquisition card 4-channel USB-based NI 9263 analog voltage output module with 16-bits digital-to-analog conversion resolution and ± 10 Volts range are used in this thesis work.

The driver level software used in this thesis work is “NI-DAQmx” in order to provide the communication between the National Instruments data acquisition cards and the computer [37]. After the installation of the driver software, the data acquisition device is detected by “NI Device Monitor” whenever it is connected to the computer through a USB port. In order to configure and test National Instruments hardware, the software interface “Measurement and Automation Explorer” is used [37]. Its shortcut icon appears on the desktop once NI-DAQmx is installed on the computer. It has four categories: (1) Data Neighborhood: It is used to view the current and create new virtual channels. (2) Devices and Interfaces: It shows currently installed and detected National Instruments hardware. It also includes utilities for configuring and testing data acquisition devices. Once a data acquisition device is connected to the computer for the first time, a “self test” should be performed. There is also a “test panels” option, which is a great utility for troubleshooting. (3) Scales: It is used to view the current and create new custom scales such as defining the sensitivity of a transducer connected to a specific channel of the data acquisition device. (4) Software: It provides access to LabVIEW programming environment, which is the application level software used in this thesis work.

5.2. Development of the Dedicated Test Software in LabVIEW Environment Following the Frequency-Response-Function Estimation Procedure

LabVIEW is a programming package distributed by National Instruments, which is easy to use with a wide range of general-purpose and special-purpose functions and “virtual instruments” (abbreviated as VI) incorporated into the programming environment so-called “Block Diagram” and offers a user-friendly interface so-called “Front Panel”. The data acquisition and signal processing software dedicated to the VEM characterization tests is developed such that it not only measures and processes signals received from the vibration transducers but also generates signals to drive the electro-dynamic shaker. Images of the designed user interface in LabVIEW are given in Appendix B.

5.2.1. Generation of Signals to Drive the Electro-dynamic Shaker in LabVIEW

Once the driver level software NI-DAQmx is installed and the data acquisition device is connected to the computer, the data acquisition VI’s appear under Measurement I/O → NI-DAQmx in the Functions palette. For transmitting the excitation signals generated in the computer to the electro-dynamic shaker amplifier through the selected data acquisition card, the “DAQ Assistant Express VI” is decided to be used. This VI achieves multiple objectives of creating, editing and running data acquisition tasks using NI-DAQmx [38]. When the VI is placed on the Block Diagram, it launches to create a new task. After selecting Generate Signals → Analog Output → Voltage → Supported Physical Channels, the VI is double-clicked to edit the newly created data acquisition task. First of all, the “Generation Mode” is selected as “Continuous Samples” in order to continuously generate signals to drive the electro-dynamic shaker during the tests. It must be noted that when continuous generation is selected, a “While loop” is automatically created around the VI, and a “Push button” appears to be connected to the “Loop Condition” terminal of the created loop such that when the button is pressed, the loop terminates execution. Then, a tick is put on “Use Waveform Timing” to use the timing information (number of samples and sampling rate) contained in the signal wired to the VI [38]. Finally, in order to avoid regeneration of the data written to the on-board memory of the data acquisition device before starting the task, the “Use Only Onboard Memory” attribute is selected as “false” so that the newly generated data within the “While loop” is continuously transferred from the memory of the computer to that of the data acquisition device [38].

In order to excite the test specimens at all frequencies of interest simultaneously, random signals are decided to be generated to drive the electro-dynamic shaker. For this purpose, a sub-program is developed within the dedicated test software, as shown in Fig.73.

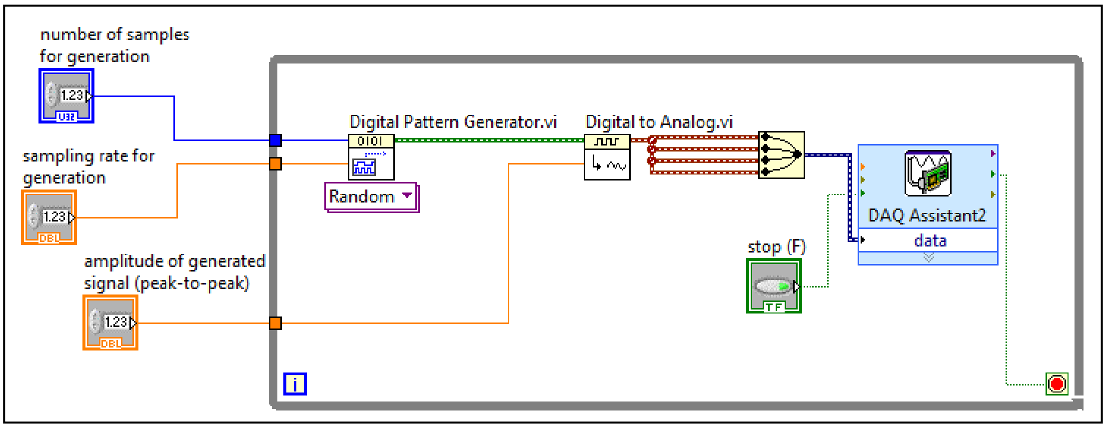

Figure 73. The part of the developed software belonging to the generation of signals to drive the electro-dynamic shaker

In Fig.73, the “Digital Pattern Generator VI” accessed under Programming → Waveform → Digital Waveform in the Functions palette generates a digital waveform composed of a set of randomly assigned “0”s and “1”s, and then the “Digital to Analog VI” accessed under Programming → Waveform converts the generated digital waveform to an analog waveform which is transferred to all four channels of the selected data acquisition device [38]. The “number of samples”, “sampling rate” and “amplitude of generated signal” per channel of the device are variables and can be controlled in the Front Panel.

5.2.2. Measurement and Processing of the Signals Received from the Vibration Transducers in LabVIEW

The flowchart for measurement of the signals coming from the transducers in LabVIEW is given in Fig.74.

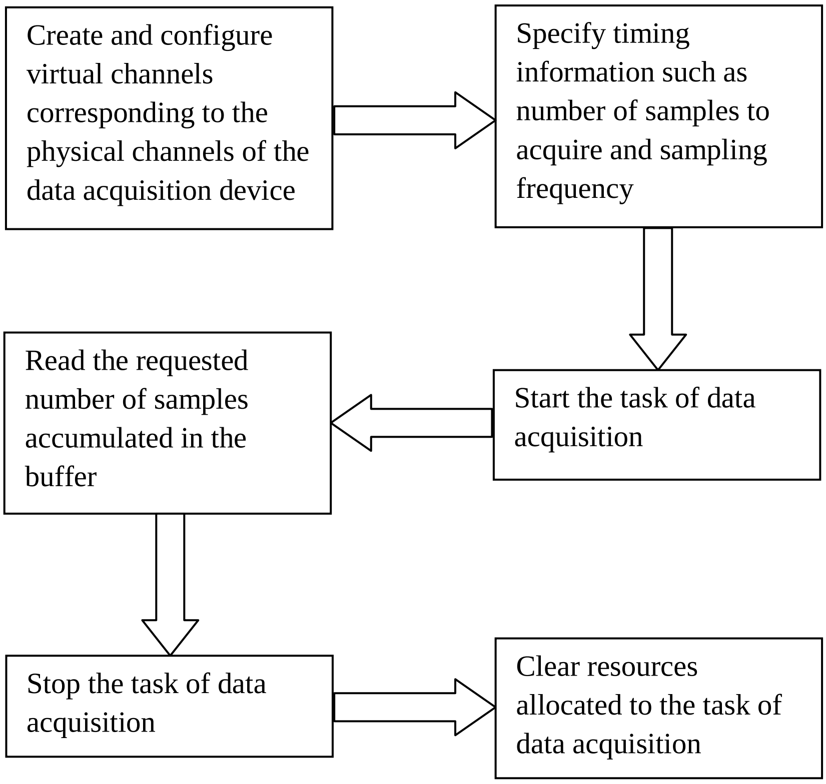

Figure 74. The flowchart for measurement of signals received from the vibration transducers in LabVIEW [37, 38]

For signal measurement, the basic data acquisition VI's are decided to be used instead of the "DAQ Assistant Express VI" because their usage provides more flexible programming facility. Therefore, the flowchart shown in Fig.74 is programmed in LabVIEW by connecting the corresponding basic VI's in the given order and configuring the VI's according to the appropriate cases in the Block Diagram. For testing tensile specimens a total number of four accelerometers two of which are mounted to the left and right sides of the tensile specimen base block and the other two are mounted to the left and right sides of the tensile specimen vibrating block, and one force sensor are used. Therefore, for tensile specimen tests the part of the developed software belonging to the measurement of signals coming from the vibration transducers is shown in Fig.75.

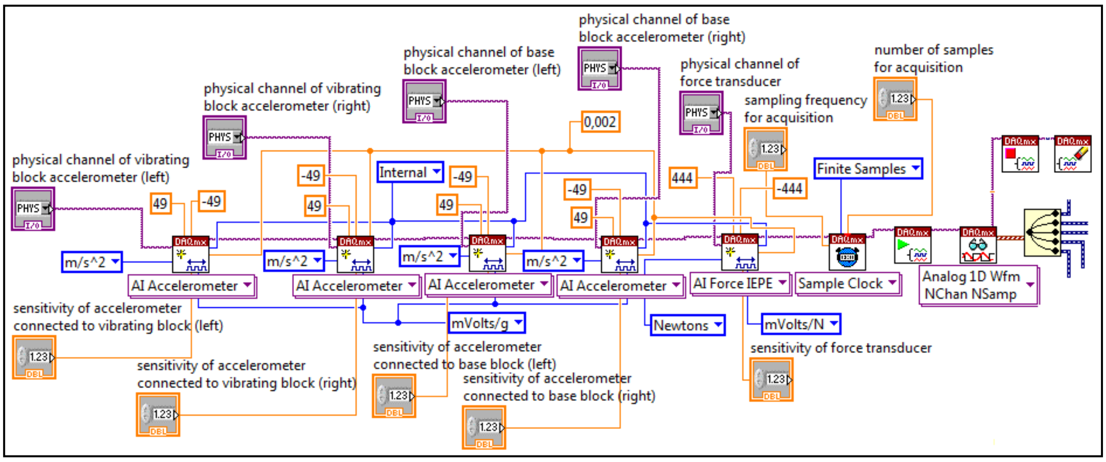

Figure 75. The part of the developed software belonging to the measurement of signals coming from the vibration transducers for tensile specimen tests, where "± 49" sets the limits of the measured acceleration signal in m/s^2 considering the used accelerometers; "± 444" sets the limits of the measured force signal in Newtons considering the used force sensor; "Internal" indicates the built-in current excitation source of the data acquisition device is used; "0.002" is the current excitation value in Amperes.

For testing shear specimens, on the other hand, a total number of three accelerometers which are mounted to the left side block, right side block and the center block, and one force sensor are used. Therefore, for shear specimen tests the part of the developed software belonging to the measurement of signals coming from the vibration transducers is shown in Fig.76.

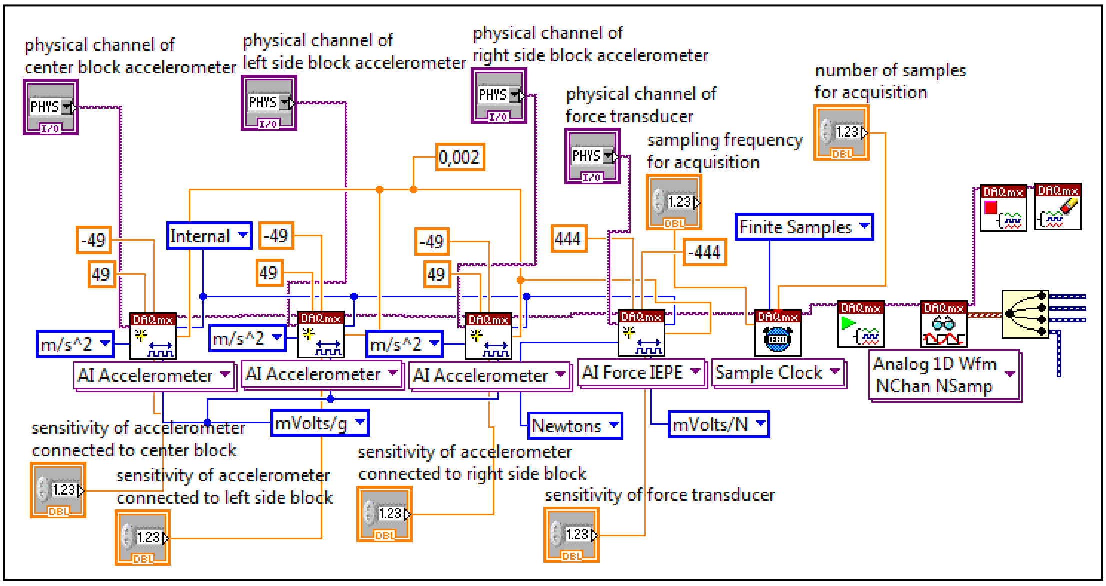

Figure 76. The part of the developed software belonging to the measurement of signals coming from the vibration transducers for shear specimen tests

The “physical channel” of the data acquisition card, “sensitivity” of the vibration transducers, and “sampling frequency” and “number of samples” per channel of the card shown in Fig’s 75 and 76 are variables and their values can be controlled in the Front Panel. The series of data sampled within a finite length of time is collected from each channel in the form of a one-dimensional waveform, which is streamed to the other parts of the developed software with bold-blue wires shown at the right sides of the Fig’s 75 and 76.

After the sampled data at each channel of the data acquisition device is transferred to the computer memory, the digital signal processing operations start. First of all, each sampled data set with a finite record length must be multiplied literally with a data window, which is in fact a weighting function in time domain with an effective length of time equal to the record length, in order to minimize the possible effects of the leakage error.

The frequency limit up to which the measurement data obtained during the VEM characterization tests is accurate is set according to the first structural modal frequency of the fixture of the test set-up, as stated in the design and validation of the test set-up part. In this frequency range, in which the fixture behaves as a rigid body, the viscoelastic specimen, either tensile or shear, and the steel rigid block attached to its end is possible to behave as a single-DOF system in the direction of the applied force, depending on the storage modulus value of the specimen. The fact that the specimen-rigid block assembly gets into resonance in the frequency range of interest especially when the specimen is in rubbery region essentially poses a problem in the digital signal processing phase. Due to the nature of digital signal processing, the measurement data is sampled at predetermined time intervals and recorded within a finite length of time. When the samples of data are converted into frequency domain through the usage of discrete Fourier transform algorithm, the record is assumed to belong to one period of a periodic function. It is highly possible that without special programming precautions this virtual periodic function has discontinuities at start/end points of each period corresponding to the integer multiples of the record length. This phenomenon causes the leakage of spectral energy especially at resonance and anti-resonance points into the side frequencies in the frequency domain; therefore the FRF estimates used in the mathematical modeling of the tested specimens will be erroneous [1]. Since the specimen-rigid block assembly is expected to get into resonance in the frequency range of interest, it is required to utilize special methods to eliminate or at least reduce the effect of this so-called "leakage error" such as using special data windows in time domain.

For stationary signals, which are expected to be involved in most vibration related-laboratory experiments, it is recommended to use "Hanning window", which is shown in Fig.77.

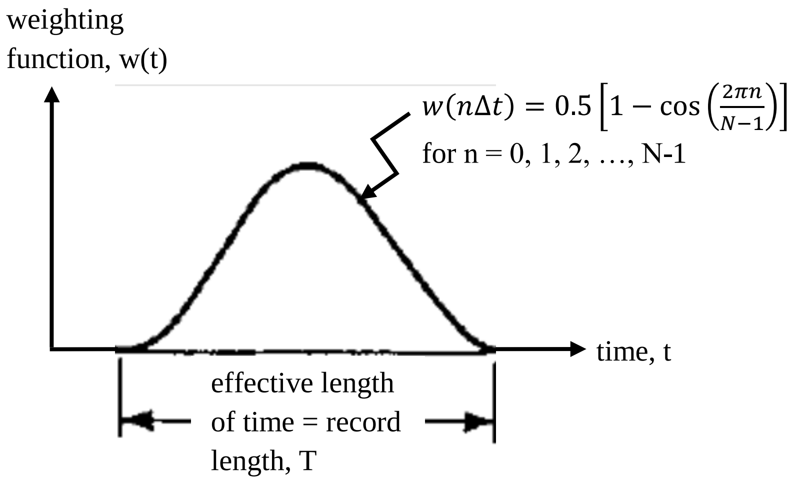

Figure 77. Hanning data window, where *N* is the number of samples; *Δt* is the time spacing between adjacent samples [1, 38]

Since Hanning window has a zero value and slope at the start and end points of the effective length of time, it provides a gradual transition over the discontinuities occurring due to periodic repetition of the sampled data [1]. Therefore, the one-dimensional waveforms corresponding to the acceleration and force signals collected from each channel of the data acquisition device are first converted to one-dimensional arrays of scalars by “Convert from Dynamic Data Express VI”s, and then upon multiplication with the direction information of the corresponding vibration transducer that is controlled in Front Panel to be either “+1” or “-1” the arrays are connected to “Hanning Window VI”s appearing under Signal Processing → Windows in the Functions palette.

After data windowing is applied, the sampled data in the time domain is transformed into the frequency domain by a “fast Fourier transform” (abbreviated as FFT) algorithm, which is approximately a hundred times faster than the “discrete Fourier transform” [1]. The discrete Fourier transform is formulated as:

$$X(m\Delta f) = \sum_{n=0}^{N-1}\left[x(n\Delta t)e^{-j(2\pi m\Delta f n\Delta t)}\right] \text{ for } m = 0, 1, 2, \ldots, N-1 \ldots \text{(Eqn.17)}$$

where x(nΔt) is the sampled data, X(mΔf) is the Fourier transform result of the sampled data, and Δf is the frequency spacing between adjacent spectral components (also known as frequency resolution), which is formulated as $\Delta f = \frac{f_s}{N}$ [1, 38]. The FFT calculator of LabVIEW is accessed under Signal Processing → Transforms in the Functions palette. Table 17 illustrates the pattern of the elements of the FFT of a sampled data series for an even number of samples, which is also equal to the size of FFT, and for “true” “Shift” value of LabVIEW’s FFT calculator, which specifies that the DC component is at the center of the FFT of the sampled data series.

Table 17. Properties of FFT calculator in LabVIEW [38]

N is even (k = N/2)		
	FFT Element	**Corresponding Frequency**
Shift = True	X_0	- (f_s/2 = Cut-off frequency)
	X_1	$-(k-1)\,\Delta f$
	X_2	$-(k-2)\,\Delta f$
	. . .	. . .
	X_{k-2}	$-2\Delta f$
	X_{k-1}	$-\Delta f$
	X_k	DC component
	X_{k+1}	Δf
	X_{k+2}	$2\Delta f$
	. . .	. . .
	X_{N-3}	$(k-3)\,\Delta f$
	X_{N-2}	$(k-2)\,\Delta f$
	X_{N-1}	$(k-1)\,\Delta f$

However, there is not a built-in frequency calculator corresponding to the elements of FFT, as listed in Table 17, in LabVIEW; therefore for this purpose a sub-program is developed, as shown in Fig.78.

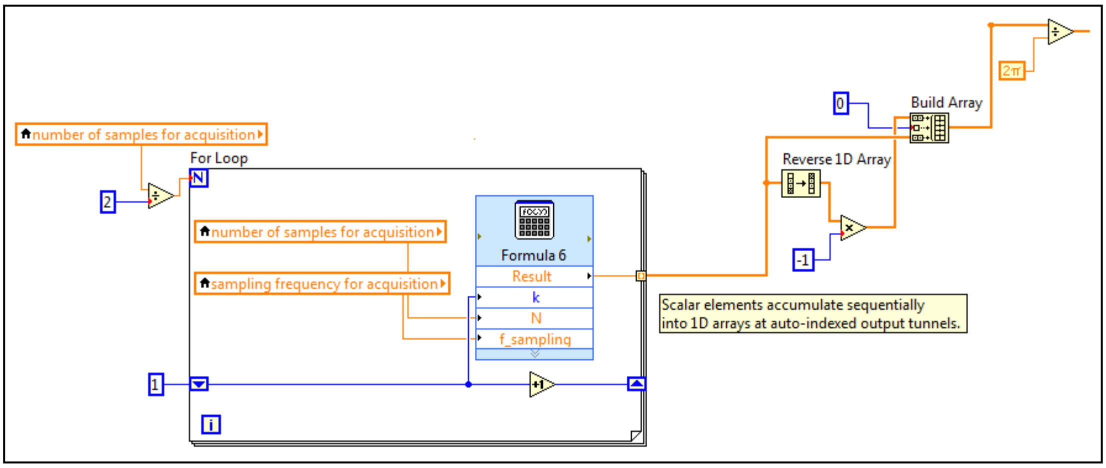

Scalar elements accumulate sequentially into 1D arrays at auto-indexed output tunnels.

Figure 78. Part of the software developed for VEM characterization that calculates frequencies corresponding to the spectral components of sampled data in time

The "Formula Express VI" (accessed under Mathematics → Script & Formula in the Functions palette) in "For Loop" (accessed under Programming → Structures in the Functions palette) shown in Fig.78 calculates the positive frequencies listed in Table 17 in rad/s as such: "number of samples" and "sampling frequency" are inserted into the formula as inputs in a "Local Variable" format (accessed under Programming → Structures in the Functions palette) and the index "k" enters the loop as a constant valued "1". It is then increased by one at each iteration utilizing the "Shift Register", which is indicated by up and down arrows on the right and left borders of the loop, respectively, as shown in Fig.78, and is used to pass the values from previous iterations through the loop to the next iteration [38]. The number of iterations is specified as "Number of samples/2" and connected to "Count" terminal of the loop, "N". After the iterations have finished, the order of the resultant one-dimensional array that is composed of the positive frequencies is reversed using "Reverse 1D Array" function (accessed under Programming → Array in the Functions palette) and all elements of the resulting array are multiplied by "-1". Finally, "Build Array" function, which is also accessed under Programming → Array in the Functions palette and concatenates multiple arrays or appends elements to an n-dimensional array (For example, if two one-dimensional arrays {1, 2} and {3, 4, 5} are wired to "Build Array", and "Concatenate Inputs" is selected from the shortcut menu, the output is the one-dimensional array {1, 2, 3, 4, 5}.), is used such that the reversed array, a constant valued "0" and the array built by the outputs of the iterations in the “for loop” are inserted into the function in the given order in order to realize the range of the frequencies from $-\pi f_s$ to $+\pi f_s$ [38].

After the components of the FFT of each sampled signal coming from the accelerometers and the force sensor and the corresponding frequencies are calculated, the auto- and cross-power spectral estimates are determined using the following formulae:

$$S_{xx_k} = X_k^* \, X_k \; \text{... (Eqn.18a)}$$

$$S_{xy_k} = X_k^* \, Y_k \; \text{... (Eqn.18b)}$$

$$S_{yy_k} = Y_k^* \, Y_k \; \text{... (Eqn.18c)}$$

where k = 0, ±1, ±2, …, ±N/2 and $S_{-k} = S_k^*$ [26].

The final step before obtaining FRF estimates is to apply “ensemble averaging” in order to minimize statistically the effects of random noise in measurements [1]. This is achieved by taking “n” sets of measurements successively, and then averaging linearly the resulting spectral estimates for each set of measurements. For this purpose, the part of the developed software including measurement of signals → Hanning window → FFT calculation → power spectral estimates is surrounded by a “For loop”. “Number of ensemble averaging” which is specified as a “Numeric Control” on the Front Panel (accessed under Modern → Numeric) is connected to “Count” terminal of the loop. For the first iteration, the arrays that enter into the loop to represent the initial spectral estimates for each set of measurements are formed by “Initialize Array” function (accessed under Programming → Array), which creates an “number of samples”-dimensional array in which every element is initialized to the value of “Element”, which is specified as “0”. After the loop executes, the terminals on the right border of the loop return the latest values of added spectral estimates for each set of measurement stored in the “Shift Registers”. In fact, the resultant spectral estimates would be divided by the “number of ensemble averaging” and multiplied by $\left(\frac{T}{N^2}\right)$ (*T*: record length; *N*: number of samples) to obtain the correct values of spectral estimates (power spectral densities); however this is not done because the ratio of the spectral estimates will be taken to calculate FRF estimates [26].

The final step is to obtain the FRF estimates. As stated in the design and validation of the test set-up part, the mathematical modeling of the test set-up requires relative displacement FRF of the rigid block attached to the specimens, as formulated in Eqn.8. Therefore, the relative acceleration FRF of the rigid block is to be estimated from the spectral estimates of the measured acceleration and force signals, and then converted to the relative displacement FRF making the basic modification formulated in Eqn.9. The "H_1 technique", which is the most common formulation, is selected to calculate FRF estimates assuming that the extraneous noise contaminates the output signals, which are measured acceleration signals, rather than the input signals, which are measured force signals [1, 38]. In addition to the FRF estimation, the "coherence" functions are also estimated to see if there is any nonlinearity involved in the test system, if there are any inputs to the test set-up other than the force input originated from the electro-dynamic shaker, and/or if there is excessive extraneous noise contaminating the measured signals [1, 26].

For tensile specimen tests, the driving-point acceleration FRF of the rigid block is calculated by linearly averaging the acceleration FRF's corresponding to the signals coming from accelerometers mounted on the left and right sides of the vibrating block, and similarly the cross-point acceleration FRF of the fixture is calculated by linearly averaging the acceleration FRF's corresponding to the signals coming from accelerometers mounted on the left and right sides of the base block, as stated in the design and validation of the test set-up part. Therefore the following formulae are used to calculate these FRF's:

$$\left(H_{rb_{driv\,pt\,accel}}\right)_{tensile} = \frac{1}{2}\left(\frac{S_{Fa_{vibr\,block\,left}}}{S_{FF}} + \frac{S_{Fa_{vibr\,block\,right}}}{S_{FF}}\right) \text{... (Eqn.19a)}$$

$$\left(H_{fix_{cross\,pt\,accel}}\right)_{tensile} = \frac{1}{2}\left(\frac{S_{Fa_{base\,block\,left}}}{S_{FF}} + \frac{S_{Fa_{base\,block\,right}}}{S_{FF}}\right) \text{... (Eqn.19b)}$$

Then, the relative acceleration FRF of the rigid block for tensile specimen tests is calculated as:

$$\left(H_{rb_{rel\,accel}}\right)_{tensile} = \left(H_{rb_{driv\,pt\,accel}}\right)_{tensile} - \left(H_{fix_{cross\,pt\,accel}}\right)_{tensile} \text{ ... (Eqn.19c)}$$

and the relative displacement FRF of the rigid block for tensile specimen tests is obtained as:

$$\left(H_{rb_{rel\,disp}}\right)_{tensile} = -\frac{\left(H_{rb_{rel\,accel}}\right)_{tensile}}{\omega^2} \text{ ... (Eqn.19d)}$$

For tensile specimen tests, the coherence functions between the force and the accelerations of the left and right sides of the vibrating block and the base block are calculated using the following formulae, respectively:

$$\left(COH_{Fa_{vibr\,block\,left}}\right)_{tensile} = \frac{\left|S_{Fa_{vibr\,block\,left}}\right|^2}{S_{FF}\ S_{a_{vibr\,block\,left}\,a_{vibr\,block\,left}}} \text{ ... (Eqn.20a)}$$

$$\left(COH_{Fa_{vibr\,block\,right}}\right)_{tensile} = \frac{\left|S_{Fa_{vibr\,block\,right}}\right|^2}{S_{FF}\ S_{a_{vibr\,block\,right}\,a_{vibr\,right}}} \text{ ... (Eqn.20b)}$$

$$\left(COH_{Fa_{base\,block\,left}}\right)_{tensile} = \frac{\left|S_{Fa_{base\,block\,left}}\right|^2}{S_{FF}\ S_{a_{base\,block\,left}\,a_{base\,block\,left}}} \text{ ... (Eqn.20c)}$$

$$\left(COH_{Fa_{base\,block\,right}}\right)_{tensile} = \frac{\left|S_{Fa_{base\,block\,right}}\right|^2}{S_{FF}\ S_{a_{base\,block\,right}\,a_{base\,block\,right}}} \text{ ... (Eqn.20d)}$$

For shear specimen tests, on the other hand, the driving-point acceleration FRF of the rigid block is equal to the driving-point acceleration FRF of the center block, and the cross-point acceleration FRF of the fixture is calculated by linearly averaging the acceleration FRF’s corresponding to the signals coming from accelerometers mounted on the left and right side blocks, as stated in the design and validation of the test set-up part. Therefore the following formulae are used to calculate these FRF’s:

$$\left(H_{rb_{driv\,pt\,accel}}\right)_{shear} = \frac{S_{Fa_{cb}}}{S_{FF}} \text{ ... (Eqn.21a)}$$

$$\left(H_{fix_{cross\,pt\,accel}}\right)_{shear} = \frac{1}{2}\left(\frac{S_{Fa_{left\,side\,block}}}{S_{FF}} + \frac{S_{Fa_{right\,side\,block}}}{S_{FF}}\right) \text{... (Eqn.21b)}$$

Then, the relative acceleration FRF of the rigid block for shear specimen tests is calculated as:

$$\left(H_{rb_{rel\,accel}}\right)_{shear} = \left(H_{rb_{driv\,pt\,accel}}\right)_{shear} - \left(H_{fix_{cross\,pt\,accel}}\right)_{shear} \text{... (Eqn.21c)}$$

and the relative displacement FRF of the rigid block for shear specimen tests is obtained as:

$$\left(H_{rb_{rel\,disp}}\right)_{shear} = -\frac{\left(H_{rb_{rel\,accel}}\right)_{shear}}{\omega^2} \text{... (Eqn.21d)}$$

For shear specimen tests, the coherence functions between the force and the accelerations of the center block and the left and right side blocks are calculated using the following formulae, respectively:

$$\left(COH_{Fa_{cb}}\right)_{shear} = \frac{\left|S_{Fa_{cb}}\right|^2}{S_{FF}\,S_{a_{cb}\,a_{cb}}} \text{... (Eqn.22a)}$$

$$\left(COH_{Fa_{left\,side\,block}}\right)_{shear} = \frac{\left|S_{Fa_{left\,side\,block}}\right|^2}{S_{FF}\,S_{a_{left\,side\,block}\,a_{left\,side\,block}}} \text{... (Eqn.22b)}$$

$$\left(COH_{Fa_{right\,side\,block}}\right)_{shear} = \frac{\left|S_{Fa_{right\,side\,block}}\right|^2}{S_{FF}\,S_{a_{right\,side\,block}\,a_{right\,side\,block}}} \text{... (Eqn.22c)}$$

5.2.3. Additional Programming in LabVIEW

The developed test software has some additional features other than signal generation and signal measurement with FRF estimation. These are: (1) Temperature measurement; (2) Setting delay between signal generation and signal measurement; (3) Determination of the storage modulus and loss factor of tested viscoelastic specimens; (4) Saving the resultant data; (5) Plotting the measured signals and the resultant data.

Since dynamic properties of viscoelastic materials are also temperature dependent, characterization tests are to be conducted at various predetermined temperatures. For this purpose, the upper part of the test set-up, which contains the test specimen, is placed into a thermal chamber, which controls the temperature. Although the nominal temperature value at which the test is desired to be conducted is known in advance, the temperature of the specimen is still measured by thermocouples placed at certain points on the test set-up close to the specimen since the test temperature entered into the control panel of the thermal chamber surely exhibits differences within the chamber due to thermal characteristics of the test set-up. In addition, the temperature of the specimen is to be tracked throughout the test since the viscoelastic specimen dissipates heat when it experiences deformation dynamically due to its inherent internal damping mechanism [12, 13]. Therefore, a temperature measurement part similar to the vibration transducer signal measurement is added to the developed test software, as shown in Fig.79.

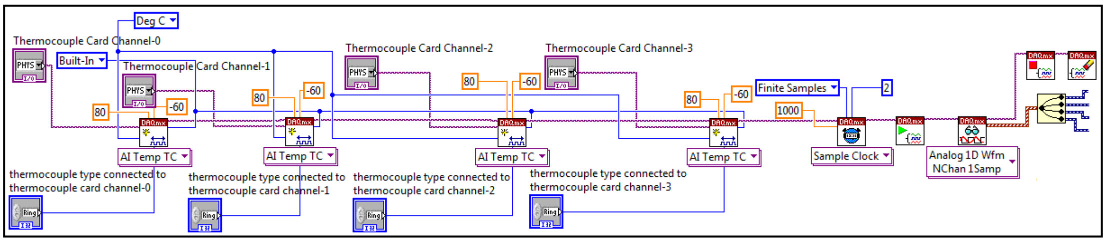

Figure 79. The part of the developed software belonging to the measurement of signals coming from the thermocouples, where “-60/+80” sets the limits of the measured temperature in deg-C considering the planned temperature range of tests; “1000” is the sampling frequency per channel of the card

The thermocouple card used in the test system is National Instruments NI 9211 4-channel thermocouple input module with USB connection. “thermocouple card channel” and corresponding “thermocouple type” shown in Fig.79 are variables and their values can be controlled in the Front Panel. One sample per channel is collected during the record length of the signals coming from the vibration transducers and to repeat this for each vibration transducer signal measurement cycle up to the “number of ensemble averaging”, the temperature measurement sub-program shown in Fig.79 is placed into the same “For loop” of the former. The acquired temperature data is then linearly averaged per channel and the resultant average temperature per channel is then multiplied with a weighting factor controllable in the Front Panel such that the sum of four weighting factors corresponding to four channels of the thermocouple card is equal to “1”. Finally, the weighted average temperatures are summed to determine the test temperature.

Setting a delay between the signal generation and the signal measurement is essential in order to wait for the transient responses to die out so that steady-state signals are measured. For this purpose, the “For loop” containing the signal measurement and processing operations is surrounded with an “Event” structure accessed under Programming → Structures in the Functions palette. The “Event” structure is composed of “Event cases”, and it waits until an “Event” occurs to execute the corresponding “Case” [38]. In the developed test software, the event is specified to be the “Value change” of a “Push button”, which is named as “Start Acquisition” in the Front Panel, and the corresponding case is the measurement and processing of the signals. When the “Push button” is pressed in the Front Panel after some time since the signal generation starts, the event which the “Event” structure is waiting for to handle occurs to execute the signal measurement and processing case. It is recommended to surround an “Event” structure with a “While loop”, and connect the “Push button”, which is placed in the “Event” structure, to the “Loop condition” terminal of the loop, which is specified as “Stop if true” [38]. Therefore, when the “Start Acquisition” is pressed, the signal measurement and processing case is executed; then the “While loop” reads the “True” value of the button and checks against the loop termination condition of “Stop if true” to stop the execution of the loop.

The developed test software calculates the storage modulus and loss factor values of the tested viscoelastic materials as a function of frequency at a specified test temperature using Eqn.12 together with Eqn.13 and Eqn.14. For tensile specimen tests, “effective vibrating mass”, “length of VEM” and “cross-sectional area of VEM” are identified as “Numerical control” on the corresponding Front Panel, while for shear specimen tests “the effective vibrating mass”, “thickness of VEM” and “cross-sectional area of VEM” are identified as “Numerical control” on the corresponding Front Panel.

LabVIEW offers a file I/O format designed specifically for engineering data management, which is named as “TDMS”. This file format provides saving and documenting the test data in a well-organized and search-ready manner, as shown in Fig.80 [39].

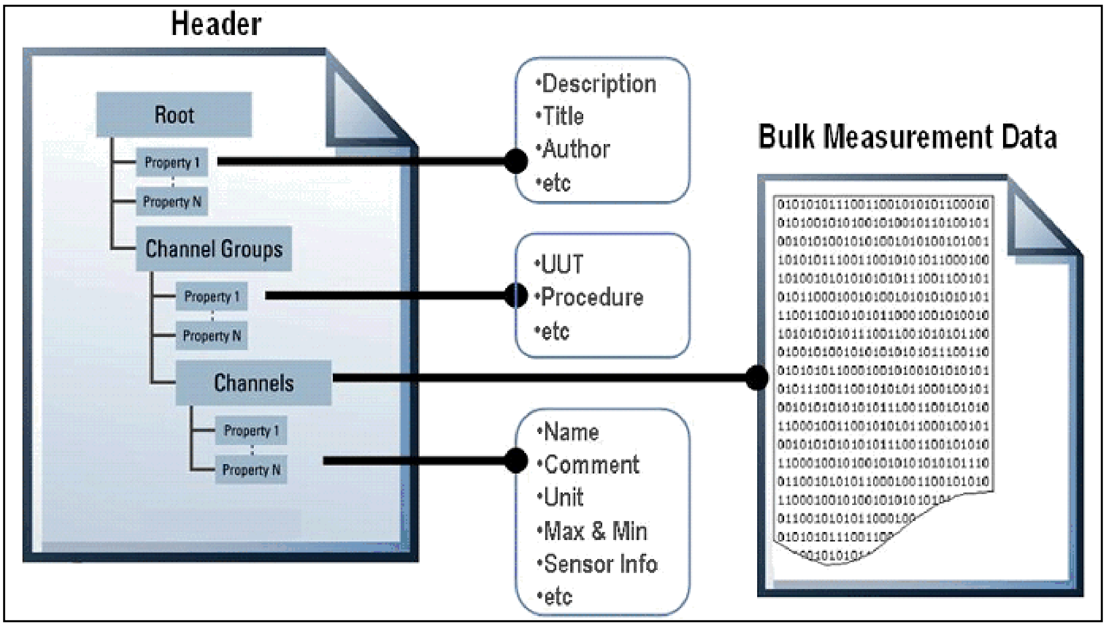

Figure 80. “TDMS” file format in LabVIEW offering three levels of hierarchy, namely “Root”, “Group”, and “Channel”, with each level allowing an unlimited number of custom properties to be defined [40]

It is also advantageous that “TDMS” files can be opened in MS Excel [39]. Therefore, it is decided to save the necessary data obtained using the developed software for viscoelastic material characterization tests in this file format. The sets of data that are saved for each test are the frequencies corresponding to the spectral estimates, the storage modulus and loss factor values calculated for the tested viscoelastic specimen, the test temperatures, the estimated FRF and coherence function values, and the test settings such as number of samples to acquire and effective vibrating mass. As an example of the sub-program developed for TDMS file saving using the basic functions accessed under Programming → File I/O → TDM Streaming, the test settings data logging is shown in Fig.81.

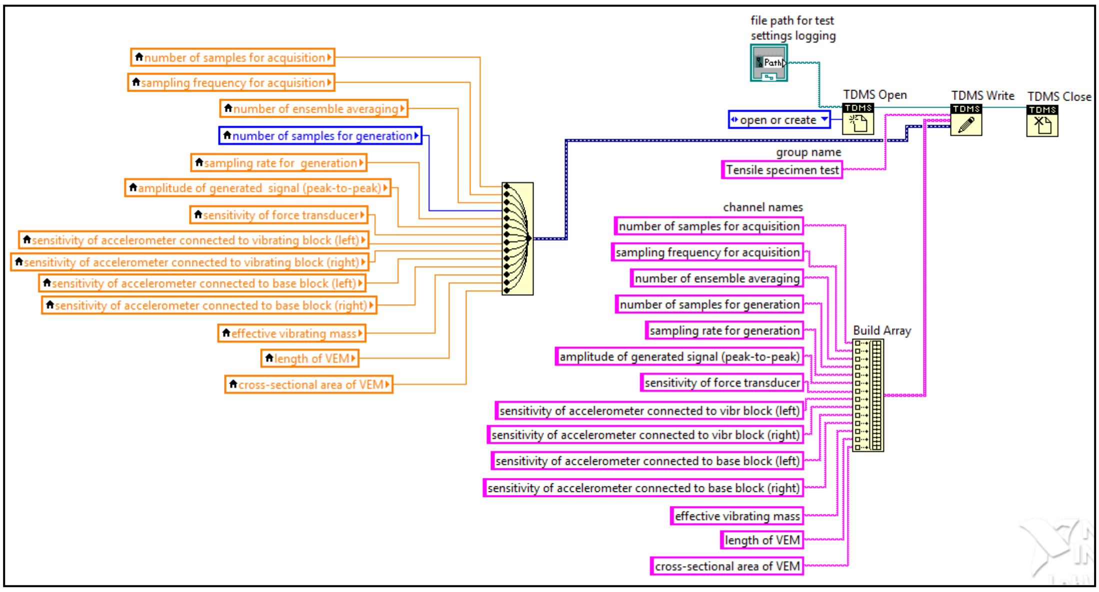

Figure 81. Saving test settings in a TDMS file whose path is selectable in the Front Panel

Finally, the desired sets of data are plotted using “Build XY Graph Express VI”, which appears on the Block Diagram as a result of placing “Express XY Graph”, accessed under Modern → Graph in controls palette, on the Front Panel. Vibration transducer signals are monitored during the signal measurements. Then, the resultant auto-power spectral estimates, driving-point, cross-point and relative acceleration FRF estimates, coherence function estimates, and the calculated storage modulus and loss factor values are plotted against the corresponding frequencies.

CHAPTER 6

DEVELOPMENT OF THE TEST PROCEDURE AND PRESENTATION OF SAMPLE TEST RESULTS

In this part of the thesis, first of all, the test procedure that is to be followed to characterize viscoelastic materials is described in detail. The test procedure involves preparation of the test specimens, installation of the selected electrical and electronic test equipment and performing of the tests, in succession. Then, the test results belonging to a viscoelastic specimen are presented with certain discussions.

6.1. Viscoelastic Material Characterization Test Procedure

For the purpose of conducting VEM characterization tests, first of all, the specimens must be prepared in advance at the desired shapes and sizes. As it is stated in the design and validation of the test set-up part, the tensile specimens that will be tested in the designed test set-up are to be in the form of a prism with a square cross-section and a length in the range of 6 cm – 9 cm, and the double-shear specimens that will be tested in the designed test set-up are to be in the form of a thin slab with a square cross-section and a thickness in the range of 1 mm – 9 mm. In addition, the material type is also important in terms of the bonding of the specimen to its blocks. It is also stated in the design and validation of the test set-up part that for tensile and double-shear specimens that require permanent bonding, for example specimens produced only by injection molding, the vibrating block-base block pairs and the center block-double connector for side block v2 pairs, respectively, must be re-manufactured, and for tensile and double-shear specimens that are self-adhesive or that can be temporarily bonded, the vibrating block-base block pairs and the center block-double side block pairs, respectively, can be re-used.

After the specimens are prepared and bonded to their blocks, the selected electrical and electronic test equipment must be installed. The thermal chamber, which is ESPEC Model SU-661 having a temperature control range of -60°C – +150°C, an internal volume of 64 liters, and a temperature setting and indication panel, is integrated to the test set-up such that the side hole extensions pass through the cable ports of 100 mm diameter located on the side walls of the thermal chamber. The 3-D model of the thermal chamber without its door is shown in Fig.82.

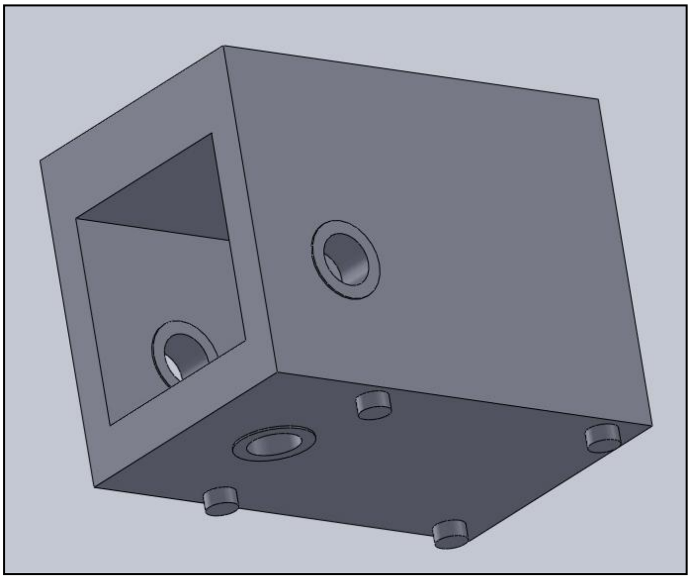

Figure 82. 3-D model of the thermal chamber integrated to the designed test set-up (without the door)

The force transducer and the accelerometers are fastened to the specimen blocks using 10-32 UNF set screws. The electrodynamic shaker accommodates a thin rod stinger of a certain length, and the threaded end of the stinger passes through the cable port of 100 mm diameter located on the bottom wall of the thermal chamber to be fastened to the force transducer while the other end is clamped into the shaker with a chuck-and-collet type clamp. The data acquisition cards (two NI 9234 4-channel analog input modules, one NI 9263 4-channel analog voltage output module and one NI 9211 4-channel thermocouple input module) are all placed into NI cDAQ-9174 4-slot chassis. The force transducer and the accelerometers are connected to NI 9234 analog input modules through BNC cables. In order to connect NI 9263 analog voltage output module to the amplifier of the shaker, two wires are tightened into one channel of NI 9263 analog voltage output module and a special connector that has two wire clips and a BNC connector is used. The measuring junctions of the T-type thermocouples are plastered to the desired points on the test set-up and the two wires extending out of the connection heads of the thermocouples are tightened into the corresponding channels of NI 9211 thermocouple input module. Finally, NI cDAQ-9174 chassis is connected to the computer through a USB cable, so that the tests can be carried out readily.

In VEM characterization tests, it is a common application to conduct a test by varying the frequency at a constant temperature, then to repeat the tests at different temperatures. Therefore, firstly one of the predetermined test temperatures in the range of -50°C – +70°C is entered into the control panel of the thermal chamber. Then, the temperatures at certain points inside the chamber are tracked on the computer using thermocouples connected to the channels of NI 9211 thermocouple input module until the desired test temperature is reached. Once the constant test temperature is ensured, the necessary information is entered into the designed user interface in LabVIEW, which is (1) input and output signal properties including sampling frequency and number of samples for acquisition, which must be equal to one of the sampling frequencies of NI 9234 analog input module and one of the positive integer powers of 2, respectively, sampling frequency and number of samples for generation, number of ensemble averaging, and amplitude of generated signal (peak-to-peak); (2) sensor settings including sensitivities, physical channels and directions of vibration transducers; (3) temperature settings including thermocouple types connected to corresponding thermocouple card channels, and weighting factors to multiply with temperature data in order to determine test temperature in the vicinity of test specimen; (4) set-up properties including effective vibrating mass, length of tensile specimen or thickness of shear specimen, and cross-sectional area of tensile or shear specimen; (5) file paths for saving the resultant data. Then, the developed test software in LabVIEW is run, and the shaker starts to excite the test specimen. After some time has passed to ensure that the transient response has died out, the start acquisition button on the user interface is pressed so that the signals from the vibration transducers and the thermocouples are started to be measured and at the same time monitored on the user interface. Once the data acquisition has finished and the stop generation button on the user interface is pressed to end up the test, the test temperature in the vicinity of the test specimen, auto-power spectral estimate graphs of the vibration transducer signals, driving-point, cross-point and relative acceleration FRF graphs, coherence function graphs, and frequency dependent storage modulus and loss factor graphs of the test specimen at the test temperature are all displayed on the user interface. Finally, the tests are repeated at the other predetermined test temperatures to obtain the frequency dependent storage modulus and loss factor data of the tensile or shear test specimen at a set of temperatures.

6.2. Sample Viscoelastic Material Characterization Test Results

Once the test system composed of the test set-up and the electrical and electronic test equipment involving the thermal chamber, the shaker with its amplifier, and the data acquisition system with the test computer is installed in the test laboratory as shown in Fig.83, tests are conducted on several tensile and shear specimens of the materials EPDM, Neoprene and Silicon.

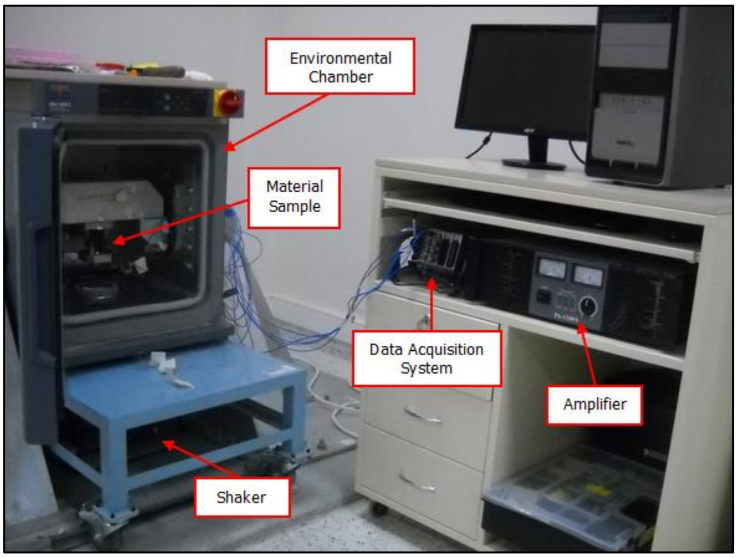

Figure 83. Test system composed of the test set-up, the thermal chamber, the shaker with its amplifier and the data acquisition system with the test computer

One of the tested tensile specimens is the synthetic rubber EPDM of 50 Shore A hardness shown in Fig.84 with the vibration transducers and the thermocouples.

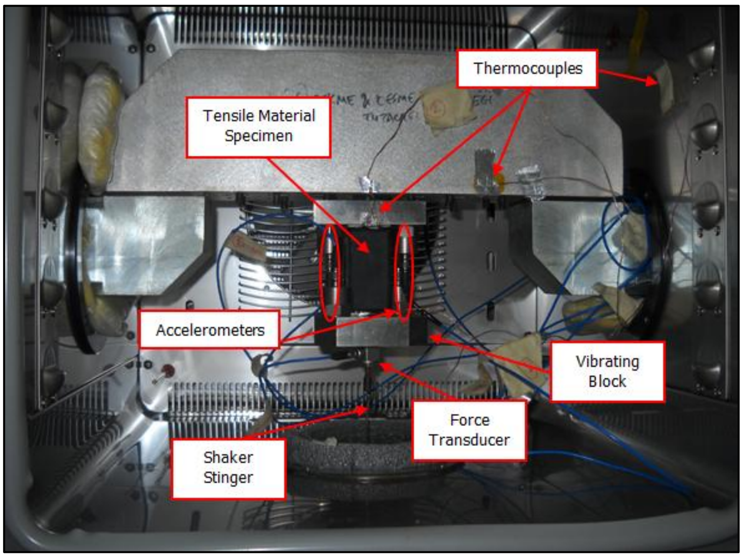

Figure 84. The prepared tensile test specimen and the placed vibration transducers and thermocouples

At the end of the characterization tests, the storage modulus and loss factor data up to approximately 800 Hz are obtained at a set of test temperatures in the range of -55°C – +20°C. Then, the useful frequency range of the data at each test temperature is specified such that the noisy data at low frequencies and the erroneous data at frequencies close to the first structural modal frequency of the test set-up are discarded. After that, the “frequency-temperature superposition” operation is performed as described in the literature survey part, and as a result the master curves for both storage modulus and loss factor are obtained at discrete frequencies and temperatures, as shown in Fig.85. The shift factors corresponding to each test temperature are also determined during this operation.

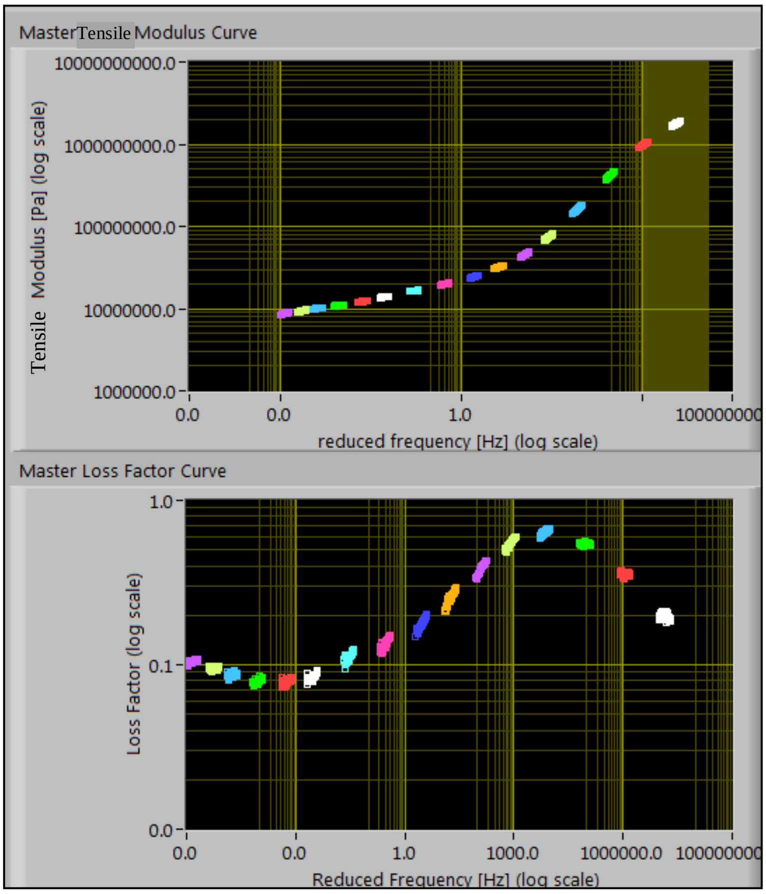

Figure 85. Master curves for the tensile specimen of the material EPDM of 50 Shore A hardness at discrete frequencies and temperatures

The Arrhenius shift factor equation is used for curve fitting to the determined shift factors corresponding to discrete temperatures, so that the shift factor at any desired temperature is obtained. Finally, in order to introduce a unique continuous relation between the storage modulus and loss factor of the tested specimen and the frequency and temperature of any desired value, a 15-parameter model is adopted for curve fitting to the master curves shown in Fig.85. The parameters of the model is determined upon a challenging trial-and-error procedure, and in the end the continuous master curves belonging to the material EPDM of 50 Shore A hardness are obtained as shown in Fig.86.

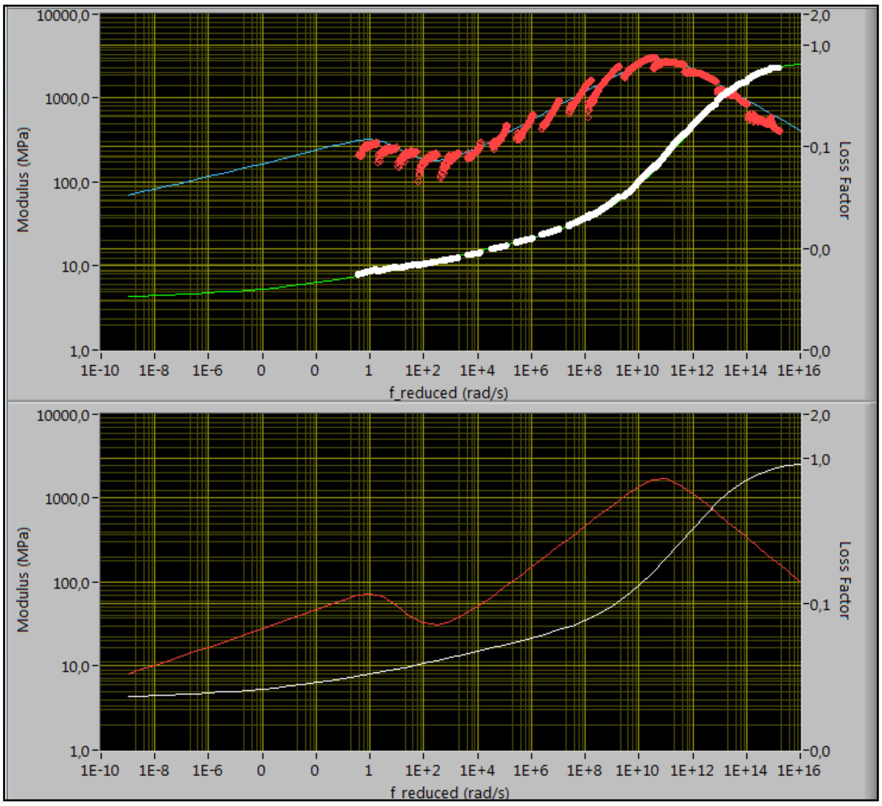

Figure 86. Continuous master curves for the tensile specimen of the material EPDM of 50 Shore A hardness together with the overlapping master curves at discrete frequencies and temperatures

Besides the aforementioned tests, another tensile specimen of the same material EPDM of 50 Shore A hardness is tested, and the results appear to be consistent for both tensile specimens, as expected. Shear specimens of the same material EPDM of 50 Shore A hardness are also tested, and it is seen that for a Poisson's ratio value of 0.499, the tensile and shear complex modulus results agree with each other, as expected.

Finally, in another study, a resilient mount is designed with a specific geometry, and certain finite element analyses are carried out to estimate the frequency and temperature dependent dynamic stiffness of this mount corresponding to different elastomeric material usage such as EPDM, Neoprene and Silicon. In these analyses, the material properties of the elastomeric materials are assigned the complex modulus data obtained as a result of the aforementioned characterization tests of these materials by use of the designed test system. Then, several mounts of the same specific geometry are fabricated of the given elastomeric materials, and certain characterization tests are also conducted on these sample mounts to determine their frequency and temperature dependent dynamic stiffness experimentally. Consequently, the dynamic stiffness data of the sample mounts obtained as a result of the finite element analyses is compared with the experimentally obtained dynamic stiffness data, and it is seen that there is a close match between them. Therefore, it can easily be said that the designed test system functions properly, and the outputs of the designed test system are sufficiently accurate.

CHAPTER 7

CONCLUSION

The thesis work titled “Development of a test system for viscoelastic material characterization” is an outcome of the synthesis of multiple disciplines associated with mechanical engineering. Mechanical vibrations is the dominating discipline while the engineering of materials, modeling and simulation of structures, and data acquisition and signal processing regarding experimental mechanics are all concerned in the thesis studies. Therefore, this thesis work serves as a valuable resource regarding all these research areas of mechanical engineering for future references. First of all, the forced non-resonant “driving-point” method to determine the unique dynamic characteristics of viscoelastic materials is investigated thoroughly. Therefore, this thesis work can readily be referred in case of the intention to implement the driving-point method for viscoelastic material characterization. The effects of inherent dynamic behavior of assumedly rigid structures are also studied extensively, and a great experience in modeling these structures for the purpose of simulating their dynamic behavior in consistence with the real world conditions is shared with those whom are planning to design a structure especially with multiple parts to be assembled using bolted-joints. Furthermore, the missions of all essential components of a data acquisition system and the objectives and outcomes of all fundamental steps of signal processing are examined, and an easy-to-use data acquisition and signal processing software is developed in LabVIEW. Therefore, the prospective users of LabVIEW can highly benefit from this thesis work, which presents a great know-how in terms of the implementation of data acquisition and signal processing in LabVIEW programming environment.

Having completed the thesis studies with all the aforementioned valuable outcomes and observed the performance of the developed test system for viscoelastic material characterization, there are certain notifications and recommendations for the purpose of improving the performance of the developed test system. Considering the method of characterization, a method other than the driving-point method could have been adopted in order to accommodate a wider frequency range for accurate and reliable measurements. It must be stated that the driving-point method is preferred because the indirect method is found out to be highly sensitive to errors involved in measurements, and there is lack of experience regarding the direct method. Nevertheless, these two methods could still have been further investigated to achieve the best performance of the test system. Especially, the direct method is implemented in most of the commercial test systems, and with a robustly-designed and well-established test set-up the upper frequency limit can be as high as 1000 Hz. Having implemented the driving-point there are still several things that can be done in order to improve the performance current test system. One thing is to determine the FRF of the fixture, which is modeled as a single-DOF system composed of an effective mass and an effective stiffness in the direction of the applied force, either by a finite element analysis or by modal testing such that the results are reliable and consistent, and insert it in the original frequency dependent complex stiffness equation. This way, the upper frequency limit of the characterization tests can be increased to a certain frequency above the first natural frequency of the fixture that is expected to be excited during the tests. Another thing is to employ linear bearings at two opposite sides of the rigid block attached to the tensile specimens. This way, the undesired bending deformations of the tensile specimens can be avoided literally, and the necessity for an effective linear averaging of the signals coming from two accelerometers symmetrically placed on the rigid block about its mass center can be eliminated. According to the current design of the test set-up, the vibration exciter is to be placed on the middle part of the base plate, and due to the presence of the thermal chamber covering the upper part of the test set-up and the four-legged frame placed on the floor to carry the thermal chamber, it is highly difficult to reach the vibration exciter to make the necessary adjustments. Therefore, the embodiment design of the test set-up would be revised to resolve this problem. Regarding the finite element modeling studies of the test set-up, simplified solid bolt models can be used to increase the accuracy of the models by taking into account the mass and more importantly the stiffness of the bolts, provided that a more powerful computer especially with a RAM capacity larger than 4 GB is used. Furthermore, the developed software for characterization tests can be revised such that the records can be overlapped, i.e. while a record is being taken, the next record can also be started to taken in order to reduce the data acquisition time. This can also minimize the temperature increase of the specimens during the tests due to shortened time for deformation of the specimens, so that almost constant temperature tests can be realized as intended. Another improvement regarding the developed software for characterization tests is that a closed-loop control algorithm can be integrated to control the generated signals to drive the vibration exciter, so that the possible distortion of the signals is minimized and the reliability of the measured data is improved. As a final improvement, an additional software can also be developed in LabVIEW for the purpose of setting and controlling the temperature of the thermal chamber through a user interface, and the communication between the thermal chamber and the computer can be provided by a GPIB card.

REFERENCES

[1] Harris, C.M., and Piersol, A.G. (Eds.), *Harris's Shock and Vibration Handbook*, 5th Ed., McGraw-Hill, 2002

[2] Jones, D.I.G., *Handbook of Viscoelastic Vibration Damping*, John Wiley & Sons Ltd., 2001

[3] Budynas, R.G., and Nisbett, K.J., *Shigley's Mechanical Engineering Design*, 8th Ed., McGraw-Hill, 2008

[4] Macioce, P., *Viscoelastic Damping*, Sound and Vibration Magazine, April 2003

[5] ISO 10846-2 2008 Acoustic and vibration – Laboratory measurement of vibro-acoustic transfer properties of resilient elements – Part 2: Direct method for determination of the dynamic stiffness of resilient supports for translatory motion

[6] ISO 10846-3 2002 Acoustic and vibration – Laboratory measurement of vibro-acoustic transfer properties of resilient elements – Part 3: Indirect method for determination of the dynamic stiffness of resilient supports for translatory motion

[7] ISO 10846-5 2008 Acoustic and vibration – Laboratory measurement of vibro-acoustic transfer properties of resilient elements – Part 5: Driving point method for determination of the low-frequency transfer stiffness of resilient supports for translatory motion

[8] ISO 18437-4 2008 Mechanical vibration and shock – Characterization of the dynamic mechanical properties of visco-elastic materials – Part 4: Dynamic stiffness method

[9] ISO 6721-4 2008 Plastics – Determination of dynamic mechanical properties – Part 4: Tensile vibration – Non-resonance method

[10] ISO 6721-6 1996 Plastics – Determination of dynamic mechanical properties – Part 6: Shear vibration – Non-resonance method

[11] ASTM D 4065-06 Standard Practice for Plastics: Dynamic Mechanical Properties: Determination and Report of Procedures

[12] ASTM D 5992-96 Standard Guide for Dynamic Testing of Vulcanized Rubber and Rubber-Like Materials Using Vibratory Methods

[13] Allen, B.R., *A Direct Complex Stiffness Test System for Viscoelastic Material Properties*, SPIE Conference on Smart Structures & Materials, San Diego, Feb. 1996

[14] Kergourlay, G., Balmés, E., and Legal, G., *A characterization of frequency – temperature – pre-stress effects in viscoelastic films,* Journal of Sound and Vibration, vol. 297, pp. 391-407, 2006

[15] Smith, G.M., Bierman, R.L., and Zitek, S.J., *Determination of Dynamic Properties of Elastomers over Broad Frequency Range,* Society of Experimental Mechanics, vol. 23, no. 2, pp. 158-164, 1983

[16] Thompson, D.J., van Vliet, W.J., and Verheij, J.W., *Developments of the Indirect Method for Measuring the High Frequency Dynamic Stiffness of Resilient Elements,* Journal of Sound and Vibration, vol. 213, issue 1, pp. 169-188, 1998

[17] Cardillo, R.M., *Dynamic Testing of Elastomer Mountings*, Journal of Applied Polymer Science, vol. 8, pp. 53-71, 1964

[18] Nadeau, S., and Champoux, Y., *Application of the Direct Complex Stiffness Method to Engine Mounts*, Experimental Techniques, vol. 24, issue 3, pp. 21-23, 2000

[19] Ozgen, G.O., Erol, F., and Batihan, A.C., *Dynamic Stiffness-Based Test Systems for Viscoelastic Material Characterization: Design Considerations*, Topics in Modal Analysis I, Volume 5: Proceedings of IMAC XXX, A Conference on Structural Dynamics, 2012

[20] Ozgen, G.O., *Design and development of a complex shear modulus measurement setup for viscoelastic materials*, SAE Technical Paper 2005-01-2285, 2005

[21] Ungar, E.E., *Damping Materials*, Ewins, D., and Rao, S.S. (Eds.), Encyclopedia of Vibration, Elsevier Ltd., pp. 327-331, 2001

[22] Kim, J., Yoon, J.-C., Kang, B.-S., *Finite element analysis and modeling of structure with bolted joints*, Applied Mathematical Modeling, vol. 31, issue 5, pp. 895-911, 2007

[23] Oliver, M., *Modeling Threaded Bolted Joints in ANSYS Workbench*, 2012, retrieved from ansys.com

[24] Montgomery, J., *Methods for Modeling Bolts in the Bolted Joint*, 2002, retrieved from ansys.com

[25] Middle East Technical University, Ankara Turkey, ME 708, Fall 2010 Lecture Notes

[26] Middle East Technical University, Ankara Turkey, ME 520, Fall 2011 Lecture Notes

[27] Maryland Metrics Fastener Catalog, retrieved from mdmetric.com

[28] ANSYS 12.1 Mechanical Help

[29] http://www.engineeringtoolbox.com/density-solids-d_1265.html, last accessed on 01/24/2014

[30] http://www.engineeringtoolbox.com/concrete-properties-d_1223.html, last accessed on 02/10/2014

[31] http://www.pcb.com/products.aspx?m=352B#.UhLaHpJM9lY, last accessed on 01/24/2014

[32] http://www.pcb.com/Products.aspx?m=208C02#.UhLa7ZJM9lY, last accessed on 01/24/2014

[33] NI 9234 Operating Instructions and Specifications retrieved from ni.com

[34] http://digital.ni.com/public.nsf/allkb/3CEFD95B14604C7386257598006C6233, last accessed on 01/24/2014

[35] NI 9263 Operating Instructions and Specifications retrieved from ni.com

[36] http://www.testunit.com/en/showp.php?id=/157.html, last accessed on 01/24/2014

[37] Lecture on *Data Acquisition and Waveforms* retrieved from http://etidweb.tamu.edu/ftp/ENTC250/Nate/LabVIEW6.ppt

[38] National Instruments LabVIEW 2010 Help

[39] *Data Storage and Reporting with NI LabVIEW*, retrieved from ni.com

[40] *Writing TDM and TDMS Files in LabVIEW*, retrieved from ni.com

[41] http://www.saginomiya.co.jp/eng/dynamic/jidousha/rubber/rubber01.html, last accessed on 02/08/2014

[42] http://www.mts.com/en/products/producttype/test-systems/load-frames-uniaxial/servohydraulic/elastomer/index.htm, last accessed on 02/08/2014

[43] http://www.acoemgroup.com/Elastomers-4-0-70-application, last accessed on 02/08/2014

[44] http://www.inovatesting.net/index.php?eID=tx_nawsecuredl&u=0&file=fileadmin/Inova/leaflets/english/Elastomer.pdf&t=1391964612&hash=ed3ecb213d6dfe815af21f0a6e59e60b, last accessed on 02/08/2014

APPENDIX A

MATLAB CODES

A.1. MATLAB Code Written to Investigate the Error in the Complex Stiffness of a Viscoelastic Specimen when the Fixture's Frequency-Response-Function is Neglected

```
clc; clear all; close all;

%A code generated to investigate the error in complex stiffness of a tested
%specimen when fixture's compliance is neglected.

f=0:1000; %frequency range of analysis [Hz]
N_freq=length(f);

%Effective vibrating mass for double-shear specimen configuration [kg]
m_eff=0.7;

%Complex shear modulus of one test specimen (Material: 3M-467 by 3M
%Company)
T=25; %room temperature [deg C]
i=(-1)^0.5;
a1=0.0425;
b1=0.214;
c1=0.00125;
beta=0.505;
TA=5278;
T0=23.9;
alfa=10^(TA*(1/(T+273)-1/(T0+273)));
shear_mod=(a1+b1*(i*f*alfa).^beta)./(1+c1*(i*f*alfa).^beta)*1e6; %[Pa]

%Dimensions of one test specimen
t=3*10^(-3); %thickness [m]
A=(50*10^(-3))*(50*10^(-3)); %cross-sectional area [m^2]
```

```
%Actual complex stiffness for one test specimen [N/m]
k_vem=shear_mod*(A/t);

%Properties of the fixture
m_fix=80; %mass [kg]
wn_fix=500*(2*pi); %first natural frequency [rad/s]
k_fix=wn_fix^2*m_fix; %stiffness [N/m]

%Amplitude of the harmonic excitation [N]
F=1;

%Complex dynamic stiffness matrix of the two dof system
K_comp=zeros(2,2,N_freq);
for ii=1:N_freq
    K_comp(:,:,ii)=[-m_eff*(2*pi*f(ii)).^2+2*k_vem(ii)   -2*k_vem(ii); ...
                -2*k_vem(ii)   -m_fix*(2*pi*f(ii)).^2+k_fix+2*k_vem(ii)];
end

%Receptance matrix of the two dof system
H_sys=zeros(2,2,N_freq);
for ii=1:N_freq
    H_sys(:,:,ii)=inv(K_comp(:,:,ii));
end

%Harmonic amplitude of displacement vector
Y_comp=zeros(2,1,N_freq);
for ii=1:N_freq
    Y_comp(:,:,ii)=H_sys(:,:,ii)*[F;0];
end

%Relative displacement to input force FRF
H_rel=(squeeze(Y_comp(1,1,:))-squeeze(Y_comp(2,1,:))).'/F;

%Complex stiffness of the tested material obtained from mathematical
%modeling neglecting the fixture's compliance
kk_vem=1/2*(1+m_eff*(2*pi*f).^2.*H_rel)./H_rel;

%%%

figure
plot(f,real(shear_mod),'go')
hold on
plot(f,t/A*real(kk_vem),'LineWidth',2)
title('Shear Storage Modulus vs. Frequency');
xlabel('f [Hz]');
ylabel('G_{storage} [Pa]');
legend('Actual G_{storage} of 3M-467',...
```

```
    'G_{storage} obtained from math. modeling');

figure
plot(f,imag(shear_mod)./real(shear_mod),'go')
hold on
plot(f,imag(kk_vem)./real(kk_vem),'LineWidth',2)
title('Loss Factor vs. Frequency');
xlabel('f [Hz]');
ylabel('loss factor');
legend('Actual Loss Factor of 3M-467',...
    'Loss Factor obtained from math. modeling');
```

A.2. MATLAB Codes Written to Determine the Vibration Response and Dynamic Strain of Test Specimens for an Excitation Force of 15 N Harmonic Amplitude

A.2.1. Tensile Specimens

```
clear all; clc;

%Determination of vibration response and dynamic strain of tensile specimen
%for an excitation force of 15 N harmonic amplitude

%Excitation frequency [Hz]
 f=input('Excitation frequency [Hz] = ');

%Effective vibrating mass [kg]
m_eff=1.2;

%Complex tensile modulus of test specimen (Material: LD-400 by Lord
%Corporation)
T=input('Test temperature [deg C] = '); %test temperature [deg C]
i=(-1)^0.5;
a1=338.2;
b1=2485;
c1=0.12;
beta=0.47;
TA=12222;
T0=15.6;
alfa=10^(TA*(1/(T+273)-1/(T0+273)));
tensile_mod=(a1+b1*(i*f*alfa).^beta)./(1+c1*(i*f*alfa).^beta)*1e6; %[Pa]

%Dimensions of test specimen
L=60*10^(-3); %length [m]
A=(30*10^(-3))*(30*10^(-3)); %cross-sectional area [m^2]

%Complex stiffness of test specimen [N/m]
```

```
k_vem=tensile_mod*(A/L);

%Properties of the fixture
m_fix=80; %mass [kg]
wn_fix=500*2*pi; %first natural frequency [rad/s]
k_fix=wn_fix^2*m_fix; %stiffness [N/m]

%Amplitude of the harmonic excitation [N]
F=15;

%Complex dynamic stiffness matrix of the two dof system
K_comp=[-m_eff*(2*pi*f)^2+k_vem   -k_vem; ...
    -k_vem   -m_fix*(2*pi*f)^2+k_fix+k_vem];

%Harmonic amplitude of displacement vector
Y_comp=K_comp\[F;0];

%%%

%Amplitude of tensile strain on the specimen [%]
tens_str=100*abs(Y_comp(1,1)-Y_comp(2,1))/L;
display(tens_str)

%Amplitude of absolute displacement of the rigid block attached to the
%specimen
Y1=abs(Y_comp(1,1));
display(Y1)

%Amplitude of absolute displacement of the fixture
Y2=abs(Y_comp(2,1));
display(Y2)

%Amplitude of acceleration of the rigid block attached to the specimen
Y1_doubledot=(2*pi*f)^2*abs(Y_comp(1,1));
display(Y1_doubledot)

%Amplitude of acceleration of the fixture
Y2_doubledot=(2*pi*f)^2*abs(Y_comp(2,1));
display(Y2_doubledot)
```

A.2.2. Shear Specimens

```
clear all; clc;

%Determination of vibration response and dynamic strain of double-shear
%specimen for an excitation force of 15 N harmonic amplitude

%Excitation frequency [Hz]
```

```
 f=input('Excitation frequency [Hz] = ');

%Effective vibrating mass [kg]
m_eff=0.7;

%Complex shear modulus of one test specimen (Material: 3M-467 by 3M
%Company)
T=input('Test temperature [deg C] = '); %test temperature [deg C]
i=(-1)^0.5;
a1=0.0425;
b1=0.214;
c1=0.00125;
beta=0.505;
TA=5278;
T0=23.9;
alfa=10^(TA*(1/(T+273)-1/(T0+273)));
shear_mod=(a1+b1*(i*f*alfa).^beta)./(1+c1*(i*f*alfa).^beta)*1e6; %[Pa]

%Dimensions of one test specimen
t=3*10^(-3); %thickness [m]
A=(50*10^(-3))*(50*10^(-3)); %cross-sectional area [m^2]

%Complex stiffness for one test specimen [N/m]
k_vem=shear_mod*(A/t);

%Properties of the fixture
m_fix=80; %mass [kg]
wn_fix=500*2*pi; %first natural frequency [rad/s]
k_fix=wn_fix^2*m_fix; %stiffness [N/m]

%Amplitude of the harmonic excitation [N]
F=15;

%Complex dynamic stiffness matrix of the two dof system
K_comp=[-m_eff*(2*pi*f)^2+2*k_vem   -2*k_vem; ...
    -2*k_vem   -m_fix*(2*pi*f)^2+k_fix+2*k_vem];

%Harmonic amplitude of displacement vector
Y_comp=K_comp\[F;0];

%%%

%Amplitude of shear strain on one specimen [%]
shear_str=100*abs(Y_comp(1,1)-Y_comp(2,1))/t;
display(shear_str)

%Amplitude of absolute displacement of the rigid center block attached to
%the specimens
```

```
Y1=abs(Y_comp(1,1));
display(Y1)

%Amplitude of absolute displacement of the fixture
Y2=abs(Y_comp(2,1));
display(Y2)

%Amplitude of acceleration of the rigid center block attached to the
%specimens
Y1_doubledot=(2*pi*f)^2*abs(Y_comp(1,1));
display(Y1_doubledot)

%Amplitude of acceleration of the fixture
Y2_doubledot=(2*pi*f)^2*abs(Y_comp(2,1));
display(Y2_doubledot)
```

APPENDIX B

IMAGES OF THE DESIGNED USER INTERFACE IN LABVIEW

B.1. User Interface of the Tensile Specimen Test Software

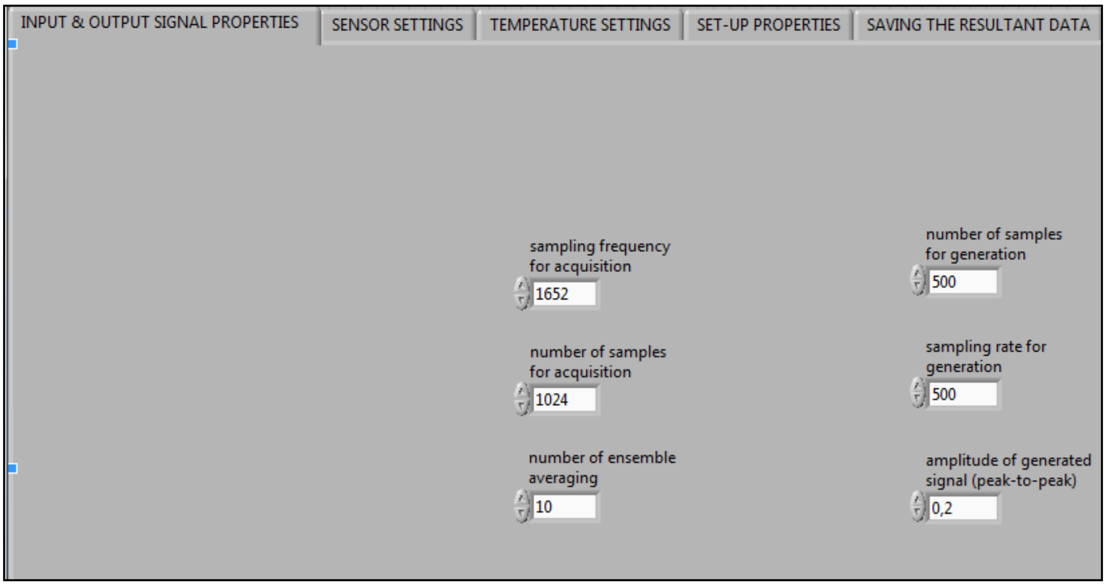

sampling frequency for acquisition: 1652

number of samples for acquisition: 1024

number of ensemble averaging: 10

number of samples for generation: 500

sampling rate for generation: 500

amplitude of generated signal (peak-to-peak): 0,2

Figure 87. The tab of the user interface for tensile specimen testing where the measured and generated signal properties are specified

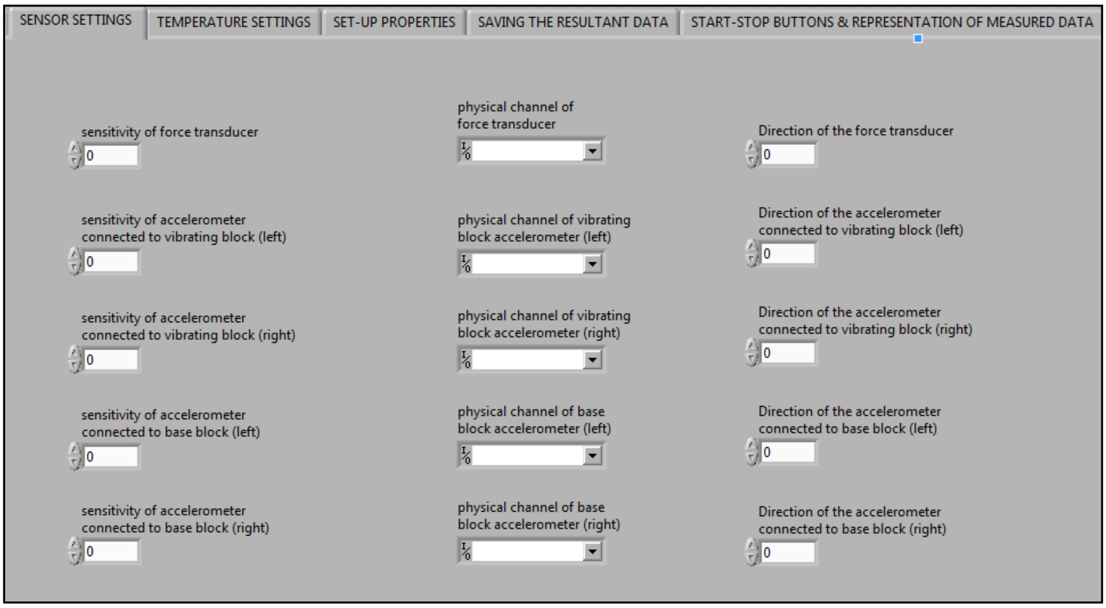

sensitivity of force transducer: 0

physical channel of force transducer:

Direction of the force transducer: 0

sensitivity of accelerometer connected to vibrating block (left): 0

physical channel of vibrating block accelerometer (left):

Direction of the accelerometer connected to vibrating block (left): 0

sensitivity of accelerometer connected to vibrating block (right): 0

physical channel of vibrating block accelerometer (right):

Direction of the accelerometer connected to vibrating block (right): 0

sensitivity of accelerometer connected to base block (left): 0

physical channel of base block accelerometer (left):

Direction of the accelerometer connected to base block (left): 0

sensitivity of accelerometer connected to base block (right): 0

physical channel of base block accelerometer (right):

Direction of the accelerometer connected to base block (right): 0

Figure 88. The tab of the user interface for tensile specimen testing where the vibration transducer settings are made

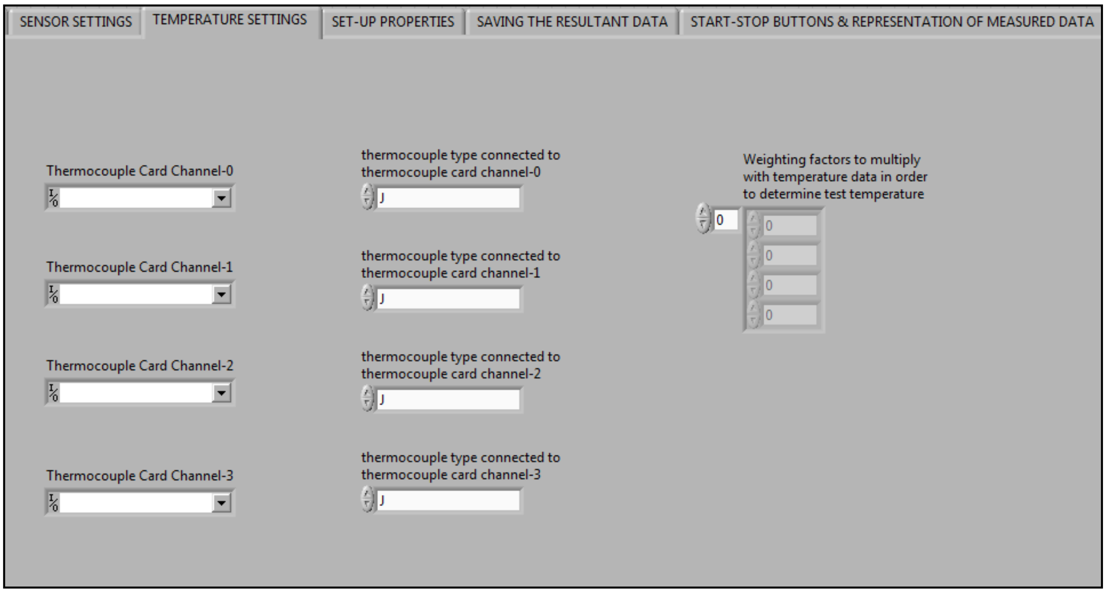

Thermocouple Card Channel-0:

thermocouple type connected to thermocouple card channel-0: J

Thermocouple Card Channel-1:

thermocouple type connected to thermocouple card channel-1: J

Thermocouple Card Channel-2:

thermocouple type connected to thermocouple card channel-2: J

Thermocouple Card Channel-3:

thermocouple type connected to thermocouple card channel-3: J

Weighting factors to multiply with temperature data in order to determine test temperature: 0; 0, 0, 0, 0

Figure 89. The tab of the user interface for tensile specimen testing where the temperature related settings are made

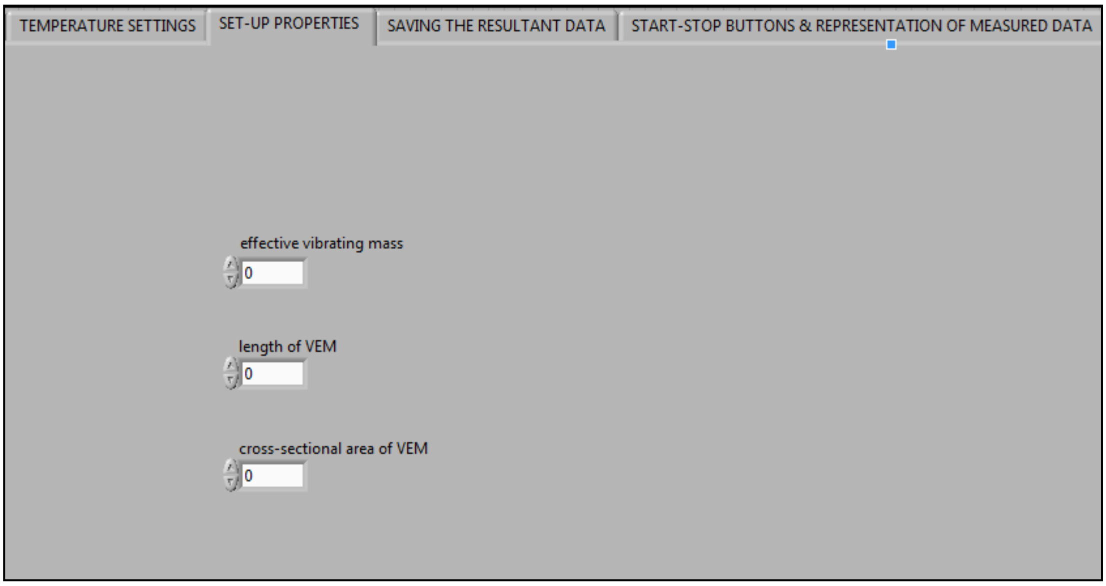

effective vibrating mass 0

length of VEM 0

cross-sectional area of VEM 0

Figure 90. The tab of the user interface for tensile specimen testing where the test set-up properties are specified

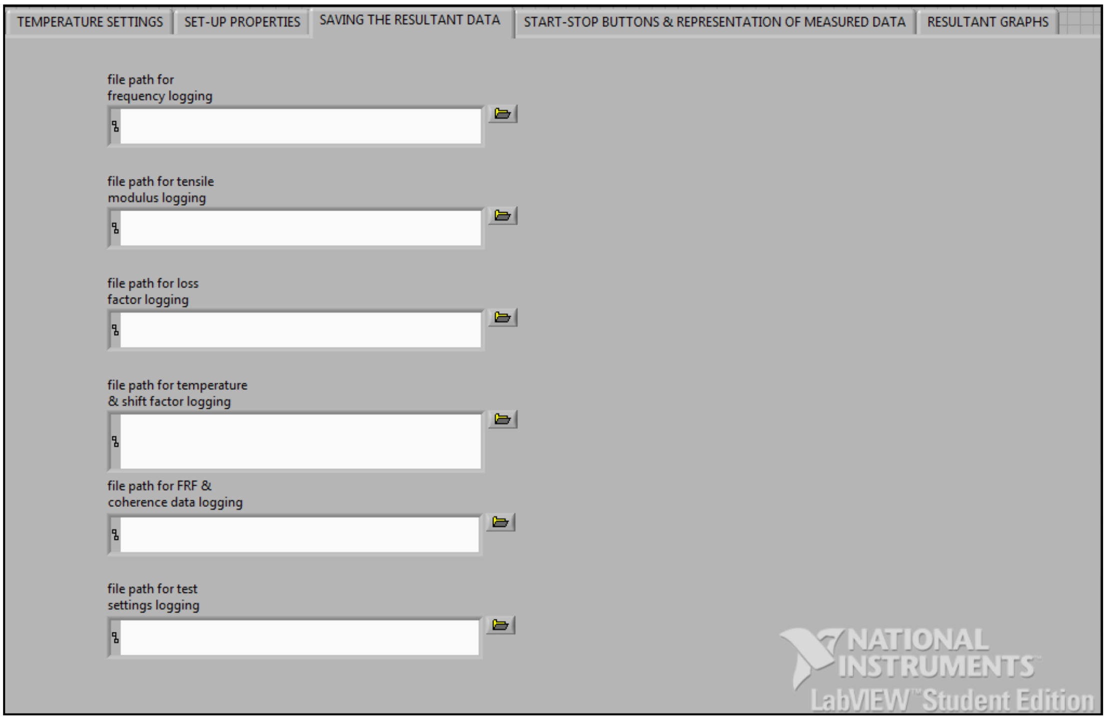

Figure 91. The tab of the user interface for tensile specimen testing where the file locations to save the resultant data are specified

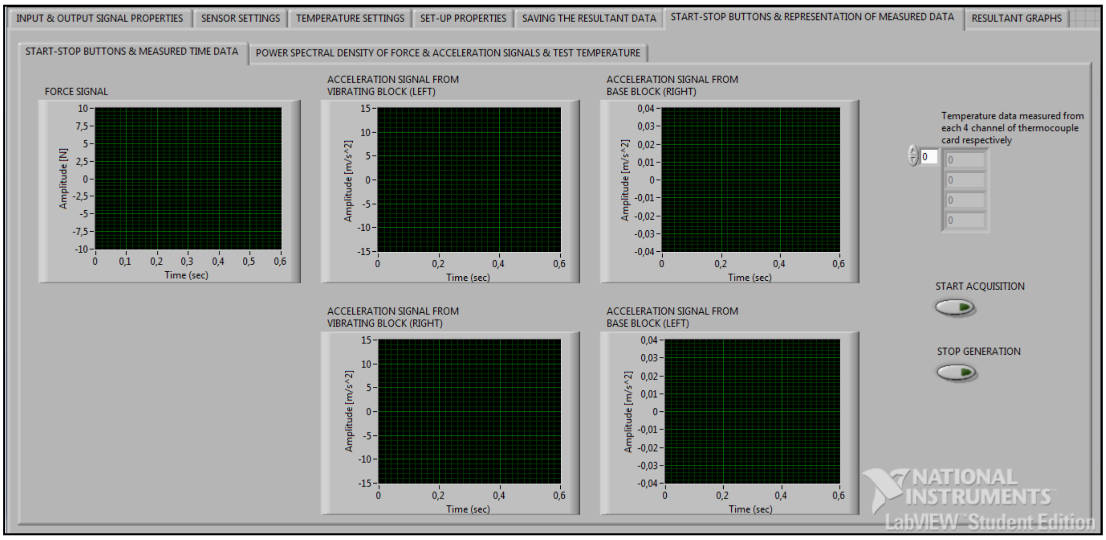

Temperature data measured from each 4 channel of thermocouple card respectively

0

0
0
0
0

Figure 92. The sub-tab of the user interface for tensile specimen testing where the start/stop buttons are located and the sets of measured data are displayed for each record

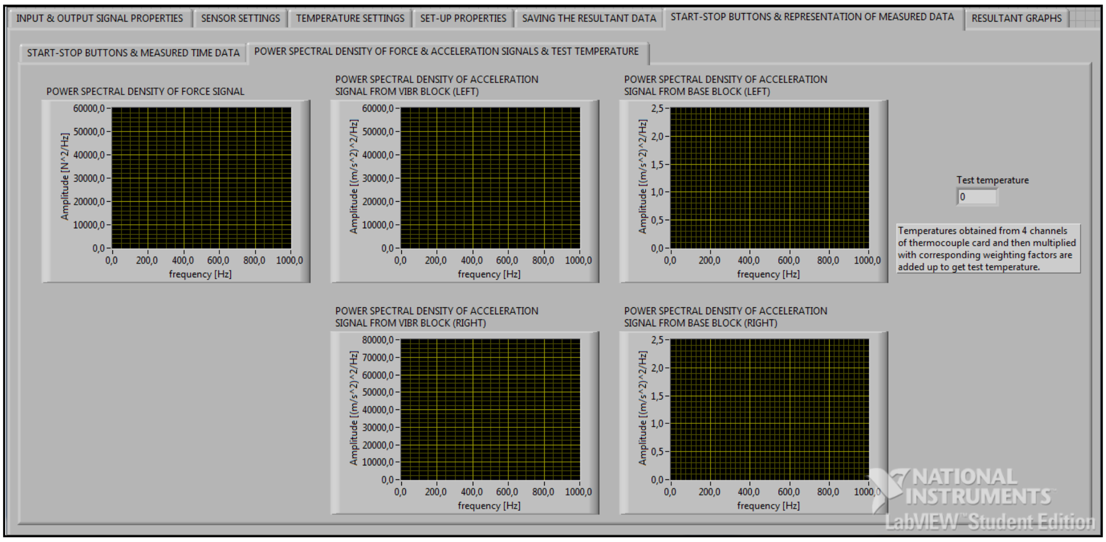

Test temperature
0

Temperatures obtained from 4 channels of thermocouple card and then multiplied with corresponding weighting factors are added up to get test temperature.

Figure 93. The sub-tab of the user interface for tensile specimen testing where the power spectral densities of the measured vibration transducer signals and the test temperature are displayed

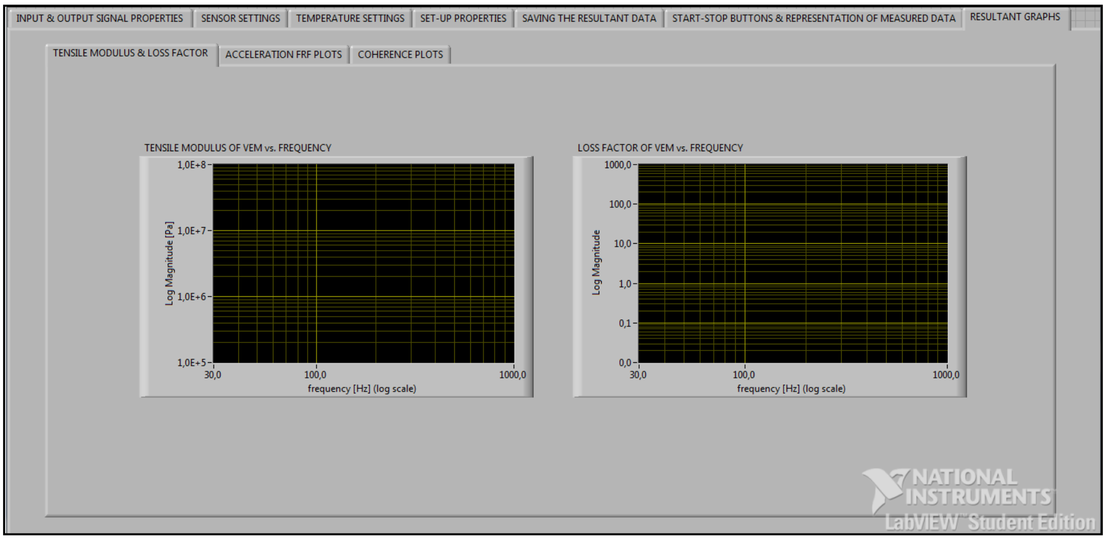

Figure 94. The sub-tab of the user interface for tensile specimen testing where the resultant frequency dependent storage modulus and loss factor data are displayed

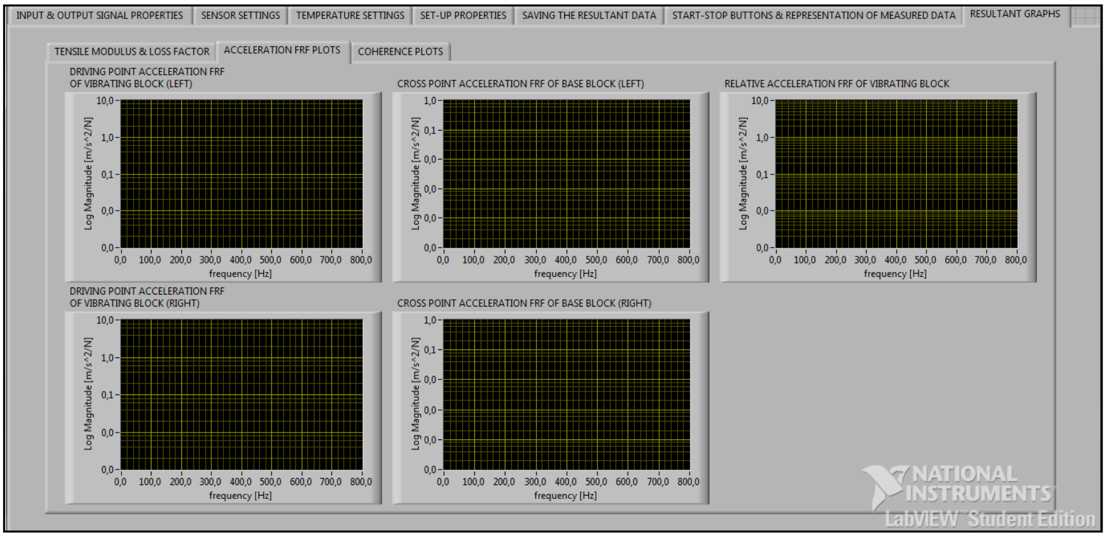

Figure 95. The sub-tab of the user interface for tensile specimen testing where the sets of resultant acceleration FRF data are displayed

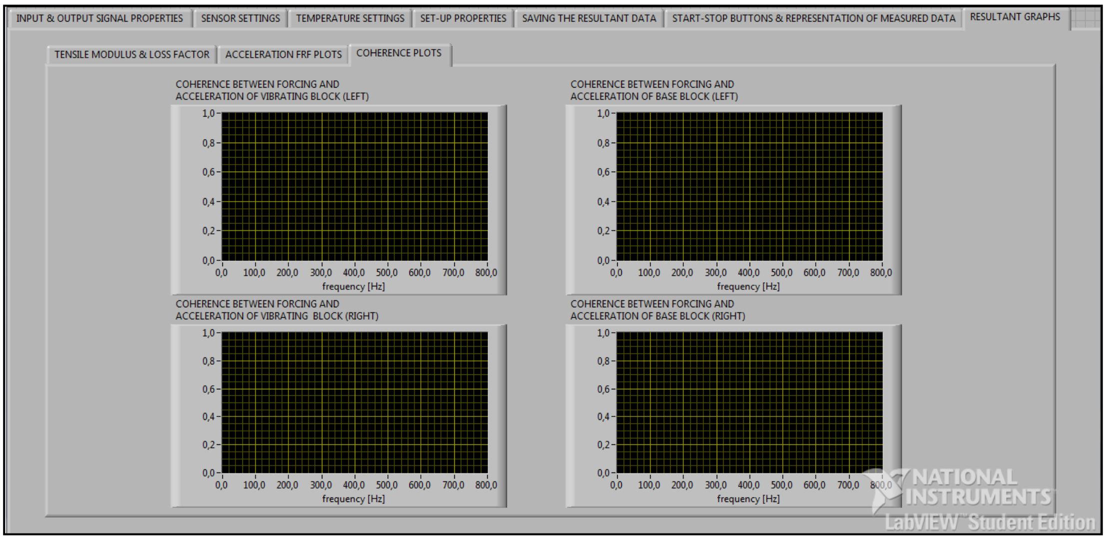

Figure 96. The sub-tab of the user interface for tensile specimen testing where the sets of resultant coherence data are displayed

B.2. User Interface of the Shear Specimen Test Software

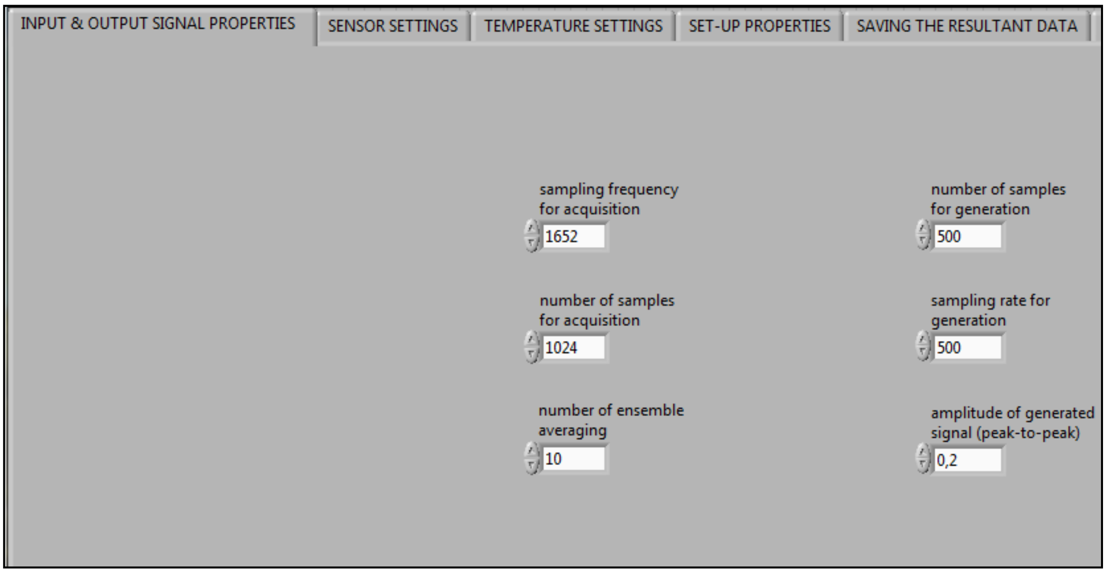

sampling frequency for acquisition: 1652

number of samples for acquisition: 1024

number of ensemble averaging: 10

number of samples for generation: 500

sampling rate for generation: 500

amplitude of generated signal (peak-to-peak): 0,2

Figure 97. The tab of the user interface for shear specimen testing where the measured and generated signal properties are specified

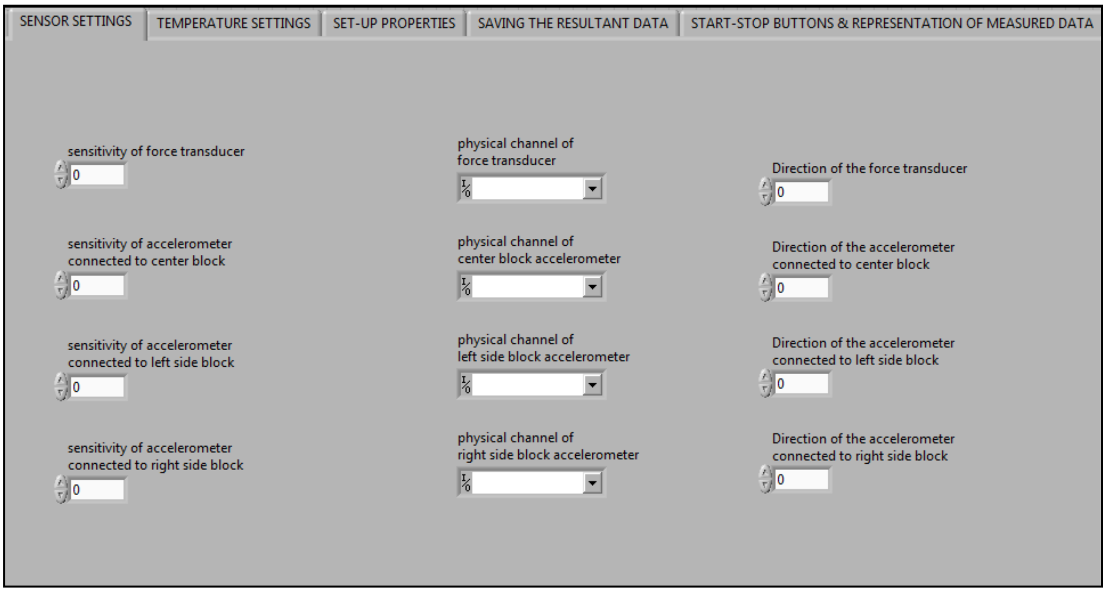

sensitivity of force transducer: 0

sensitivity of accelerometer connected to center block: 0

sensitivity of accelerometer connected to left side block: 0

sensitivity of accelerometer connected to right side block: 0

physical channel of force transducer:

physical channel of center block accelerometer:

physical channel of left side block accelerometer:

physical channel of right side block accelerometer:

Direction of the force transducer: 0

Direction of the accelerometer connected to center block: 0

Direction of the accelerometer connected to left side block: 0

Direction of the accelerometer connected to right side block: 0

Figure 98. The tab of the user interface for shear specimen testing where the vibration transducer settings are made

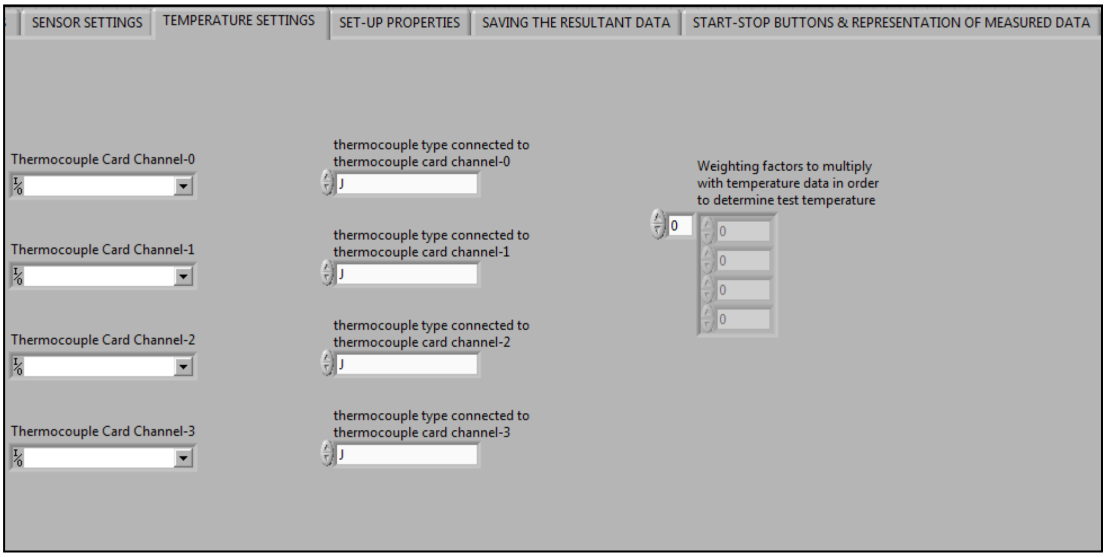

Thermocouple Card Channel-0:

Thermocouple Card Channel-1:

Thermocouple Card Channel-2:

Thermocouple Card Channel-3:

thermocouple type connected to thermocouple card channel-0: J

thermocouple type connected to thermocouple card channel-1: J

thermocouple type connected to thermocouple card channel-2: J

thermocouple type connected to thermocouple card channel-3: J

Weighting factors to multiply with temperature data in order to determine test temperature: 0; 0, 0, 0, 0

Figure 99. The tab of the user interface for shear specimen testing where the temperature related settings are made

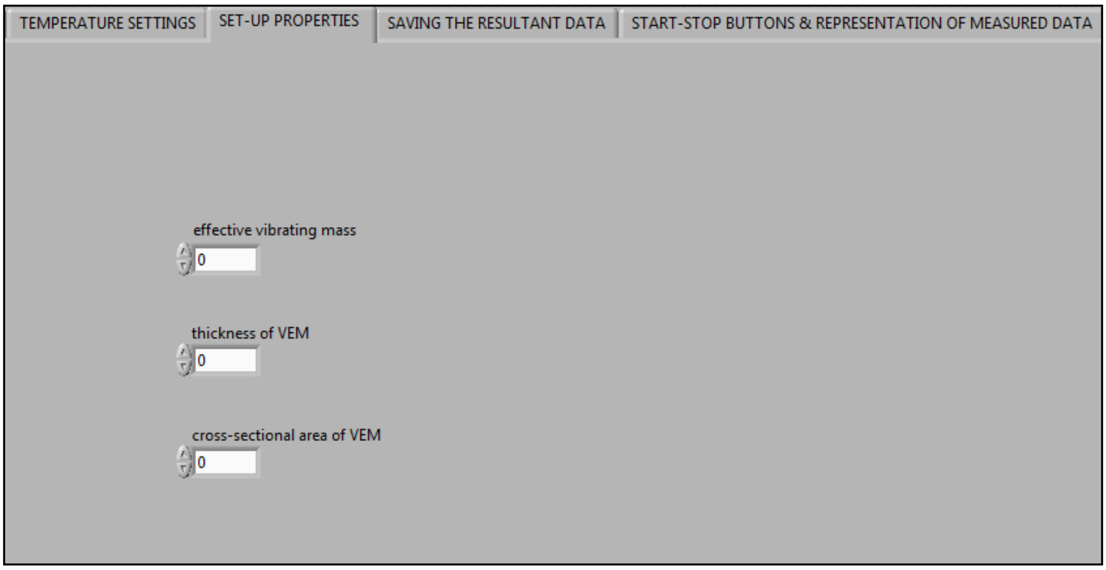

effective vibrating mass 0

thickness of VEM 0

cross-sectional area of VEM 0

Figure 100. The tab of the user interface for shear specimen testing where the test set-up properties are specified

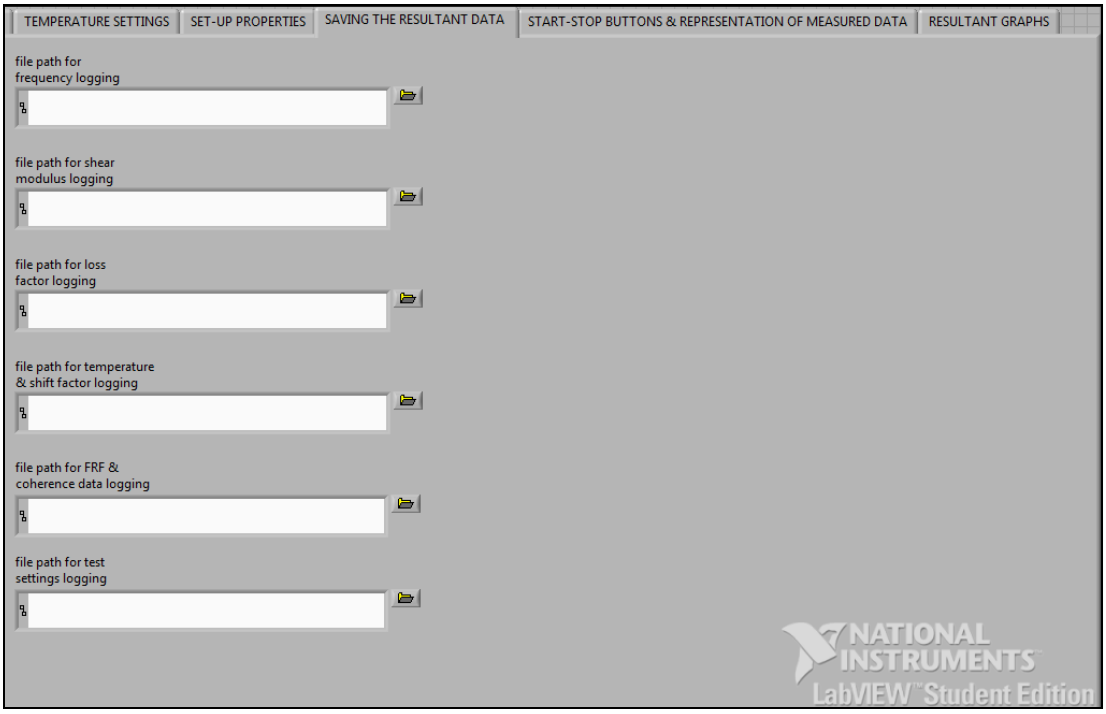

file path for frequency logging

file path for shear modulus logging

file path for loss factor logging

file path for temperature & shift factor logging

file path for FRF & coherence data logging

file path for test settings logging

Figure 101. The tab of the user interface for shear specimen testing where the file locations to save the resultant data are specified

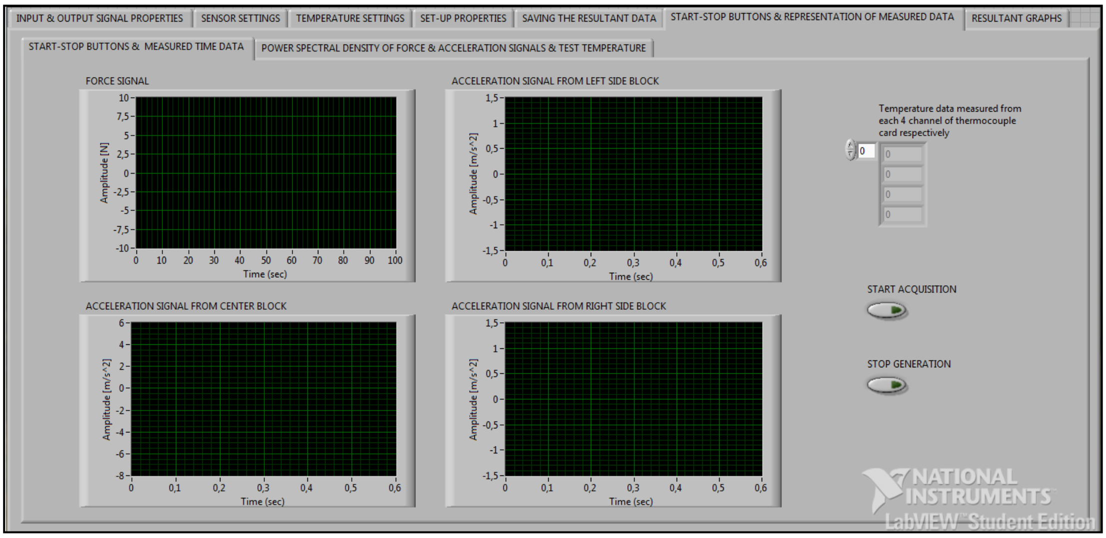

Temperature data measured from each 4 channel of thermocouple card respectively

0
0
0
0
0

Figure 102. The sub-tab of the user interface for shear specimen testing where the start/stop buttons are located and the sets of measured data are displayed for each record

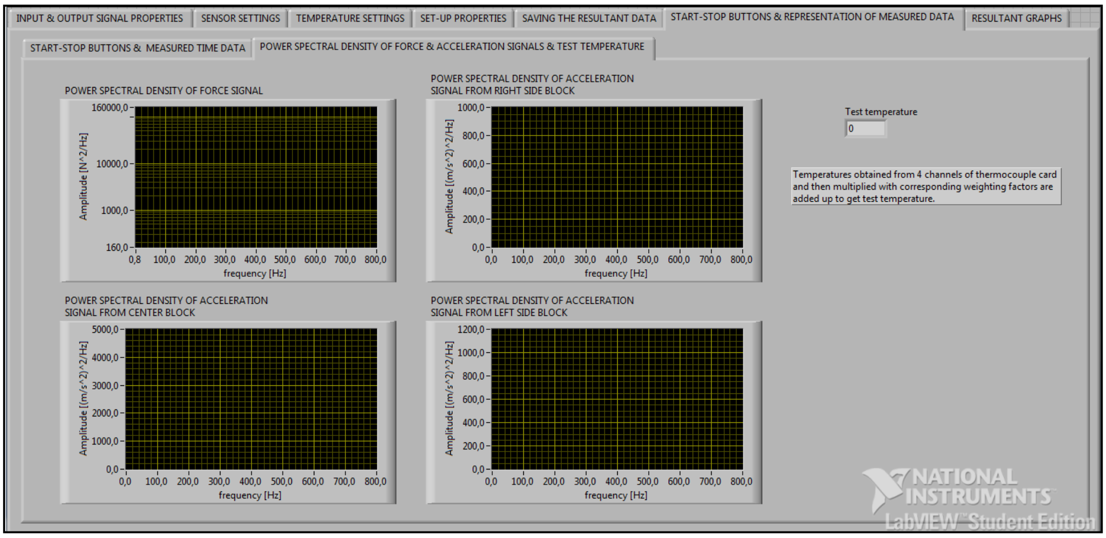

Test temperature: 0

Temperatures obtained from 4 channels of thermocouple card and then multiplied with corresponding weighting factors are added up to get test temperature.

Figure 103. The sub-tab of the user interface for shear specimen testing where the power spectral densities of the measured vibration transducer signals and the test temperature are displayed

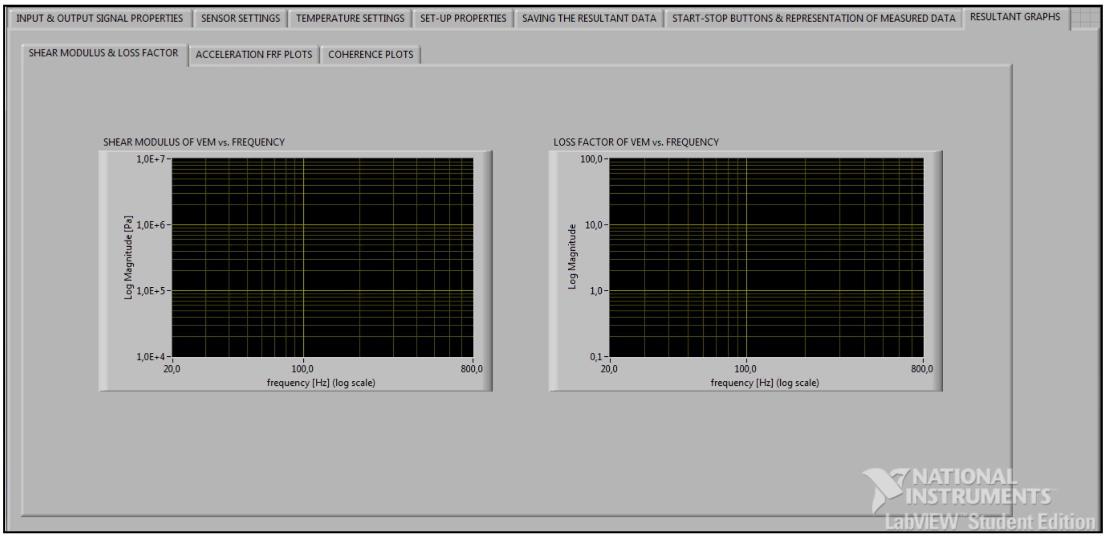

Figure 104. The sub-tab of the user interface for shear specimen testing where the resultant frequency dependent storage modulus and loss factor data are displayed

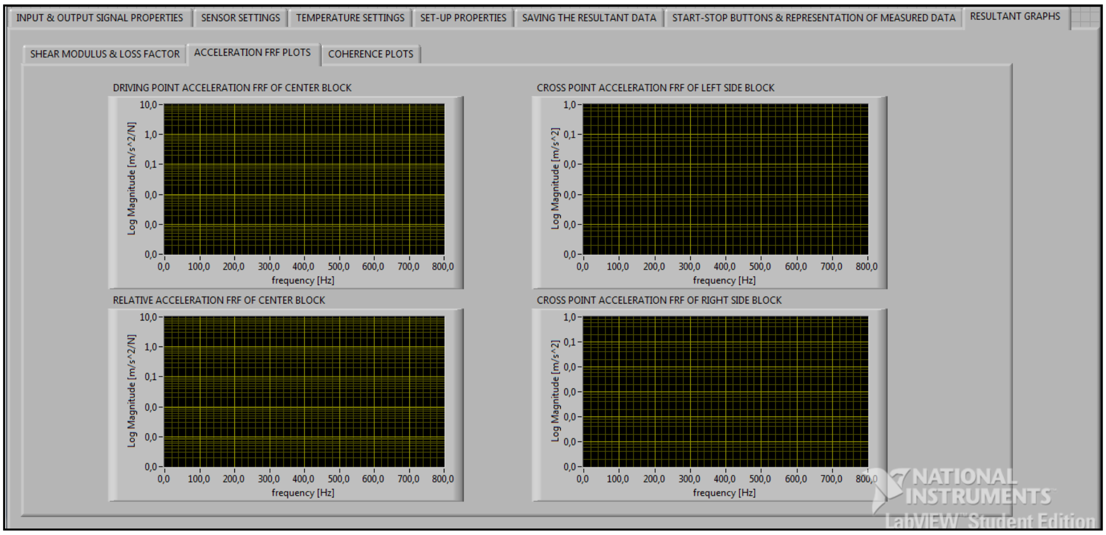

Figure 105. The sub-tab of the user interface for shear specimen testing where the sets of resultant acceleration FRF data are displayed

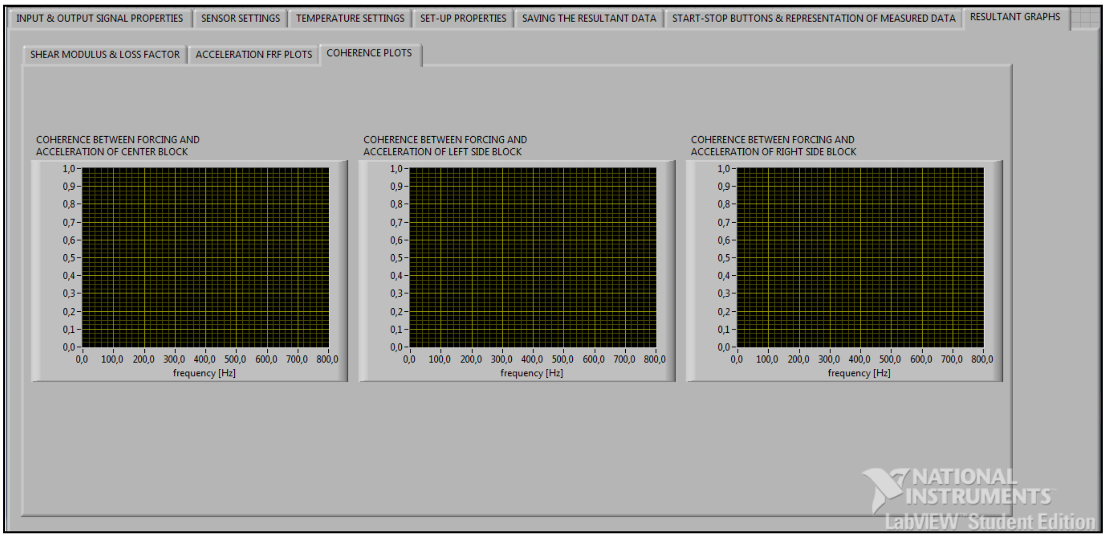

Figure 106. The sub-tab of the user interface for shear specimen testing where the sets of resultant coherence data are displayed